ABSTRACT

CHARACTERIZING THE CONDENSATION HEAT TRANSFER PERFORMANCE OF UNIFORM AND PATTERNED SILICA NANOSPRING-COATED TUBES

by Nickolas Charles Schmiesing

In this work, the condensation heat transfer performance of silica nanospring-coated horizontal aluminum tubes is assessed. Coated samples with varying nanospring mat thicknesses, dependent on growth time, were evaluated against a baseline aluminum sample. Condensation heat transfer testing with water was performed in an evacuated environmentally controlled chamber at flowrates ranging from 1.5 to 5.5 LPM and subcooling temperatures of 1.5, 5.5, and 9.5°C ($T_{sat} \approx 20$°C). During this testing, the nanospring-coated samples exhibited similar condensation heat transfer coefficients to the baseline sample and the SN15 sample (15-min. growth) increased the heat transferred to the cooling fluid by 60% as compared to the baseline. A patterned sample with alternating hydrophobic and hydrophilic rings was created with 15 minutes of growth, which offered similar heat transfer performance to the SN15 sample. Video analysis determined that the SN15 and SN20 (20-min. growth) experienced an 84% increase in the condensate removal rate over the baseline, while the patterned sample experiences a 96% increase. SEM imaging revealed that the coating withstood the condensation environment. Additional work needs to be performed to further evaluate the coating, but these findings suggest that the coating may be capable of improving condensation heat transfer performance.

CHARACTERIZING THE CONDENSATION HEAT TRANSFER PERFORMANCE OF UNIFORM AND PATTERNED SILICA NANOSPRING-COATED TUBES

Thesis

Submitted to the

Faculty of Miami University

in partial fulfillment of

the requirements for the degree of

Master of Science in Mechanical Engineering

by

Nickolas Charles Schmiesing

Miami University

Oxford, Ohio

2019

Adviser: Dr. Andrew Sommers

Adviser: Dr. Giancarlo Corti

Reader: Dr. Edgar Caraballo

Reader: Dr. Carter Hamilton

This thesis titled

CHARACTERIZING THE CONDENSATION HEAT TRANSFER PERFORMANCE OF UNIFORM AND PATTERNED SILICA NANOSPRING-COATED TUBES

by

Nickolas Charles Schmiesing

has been approved for publication by

College of Engineering and Computing

and

Department of Mechanical and Manufacturing Engineering

_____

Dr. Andrew Sommers

_____

Dr. Giancarlo Corti

_____

Dr. Edgar Caraballo

_____

Dr. Carter Hamilton

Table of Contents

List of Tables

List of Figures

Nomenclature

Abbreviations:

θ_{adv}	Advancing contact angle measurement (°)
θ_{rec}	Receding contact angle measurement (°)
θ_{static}	Static contact angle measurement (°)
A_i	Interior surface area (m^2)
A_o	Exterior surface area (m^2)
A_s	Surface area (m^2)
$APCVD$	Atmospheric pressure chemical vapor deposition
BET	Brunauer-Emmett-Teller
c_p	Specific heat $(J\ K^{-1}\ kg^{-1})$
CAH	Contact angle hysteresis (°)
CVD	Chemical vapor deposition
D_i	Inner diameter (m)
D_{max}	Maximum diameter (m)
D_o	Outer diameter (m)
DAQ	Data acquisition unit
DC	Direct current
DWC	Dropwise condensation
EES	Engineering Equation Solver
$Eq.$	Equation
f	Darcy friction factor
$Fig.$	Figure
FWC	Filmwise condensation
$\bar{h}$	Average convective heat transfer coefficient $(W\ m^{-2}\ K^{-1})$
h_i	Interior heat transfer coefficient $(W\ m^{-2}\ K^{-1})$
h_o	Exterior heat transfer coefficient/condensation heat transfer coefficient $(W\ m^{-2}\ K^{-1})$
$HVAC\&R$	Heating, ventilation, air conditioning, and refrigeration
ID	Identification
k	Thermal conductivity $(W\ m^{-1}\ K^{-1})$
L	Length (m)
LED	Light emitting diode
$LPCVD$	Low-pressure chemical vapor deposition
$\dot{m}$	Mass flowrate $(kg\ s^{-1})$

Nu_D	Nusselt number
Pr	Prandtl number
P_{sat}	Saturation pressure (Pa)
q	Heat transferred to the cooling fluid (W)
R	Thermal resistance $(K\ W^{-1})$
R_i	Interior thermal resistance $(K\ W^{-1})$
R_o	Exterior thermal resistance $(K\ W^{-1})$
R_{SN}	Thermal resistance of the silica nanospring mat $(K\ W^{-1})$
R_{tot}	Total thermal resistance $(K\ W^{-1})$
R_{wall}	Thermal resistance of the tube wall $(K\ W^{-1})$
Re_D	Reynolds number
RIE	Reactive ion etching
RTD	Resistance temperature detector
SAM	Self-assembled monolayer
SEM	Scanning electron microscope/microscopy
SN	Silica nanosprings
TEM	Transmission electron microscope/microscopy
$T_{m,in}$	Mean cooling fluid temperature at the tube inlet $(°C)$
$T_{m,out}$	Mean cooling fluid temperature at the tube outlet $(°C)$
$T_{s,in}$	Tube surface temperature at the tube inlet $(°C)$
$T_{s,out}$	Tube surface temperature at the tube outlet $(°C)$
$T_{s,avg}$	Average tube surface temperature $(°C)$
T_∞	Temperature of the tube surroundings $(°C)$
$\overline{U}$	Overall heat transfer coefficient $(W\ m^{-2}\ K^{-1})$
$\Delta T_{subcooling}$	Subcooling temperature $(°C)$
V	Volume (mL)
VLS	Vapor-liquid-solid
$XEDS$	X-ray energy dispersive spectroscopy

Subscripts:

avg	Average
i	Interior
in	Inlet
m	Mean of the cooling fluid
o	Exterior
out	Outlet
s	Surface
tot	Total
$wall$	Tube wall
∞	Surroundings

Units:

cm	Centimeter
g	Gram
Hz	Hertz
$in.$	Inch
K	Kelvin
keV	Kiloelectron volt
kPa	Kilopascal
LPM	Liter per minute
m	Meter
min	Minute
mm	Millimeter
nm	Nanometer
Pa	Pascal
rpm	Revolutions per minute
s	Second
$torr$	Torr
W	Watt
μm	Micrometer
$^\circ$	Degree
$^\circ C$	Degree Celsius
$\%$	Percent

Dedication

To my family, friends, and mentors that have assisted me through times of hardship and celebrated with me in times of joy. Sincerely, thank you for helping me on this journey.

Acknowledgements

I would like to thank Dr. Andrew Sommers and Dr. Giancarlo Corti for presenting me this opportunity to conduct research alongside them and for providing guidance throughout this project. Additionally, I would like to thank Dr. Edgar Caraballo and Dr. Carter Hamilton for serving on my thesis committee and providing feedback on this project. I would also like to thank the senior design team of Anna Davis, Jahnathan Kidd, and Joseph Engelhardt for developing the vacuum chamber used within the experimental setup, and Kyle Swann for his work in the preliminary testing of samples within the chamber. I would like to thank Matt Duley, Dr. Richard Edelmann, and the other members of the Center for Advanced Microscopy and Imaging (CAMI) for providing instruction on the operation of the microscopes used throughout this project. Finally, I would like to thank my friends and family for their continuous support throughout this experience.

CHARACTERIZING THE CONDENSATION HEAT TRANSFER PERFORMANCE OF UNIFORM AND PATTERNED SILICA NANOSPRING-COATED TUBES

1.0 INTRODUCTION

With applications ranging from automobiles to heating, ventilation, air conditioning, and refrigeration (HVAC&R), to steam condensation in power generation, heat exchangers have a significant impact on many industries in the world today. As a result, these heat exchangers also represent a significant portion of the cost associated with the development, production, and operation of these applications. In order to reduce these costs, it is desirable to improve the efficiency of these heat exchangers [1,2]. Other benefits of improving the performance capabilities of heat exchangers include a reduction in the amount of pollution and a decreased risk of airborne pathogens (such as Legionella bacteria) which can originate in air-cooling applications with condensation and cause Legionnaire's disease or other respiratory infections [3,4]. In this study, a novel method for improving condensation heat transfer performance is discussed, which has the potential to improve heat exchanger efficiency.

The basic purpose of using a heat exchanger is to transfer energy from one medium to another. This commonly occurs between two fluids, where a cooling fluid (such as water) flows through a series of tubes while a warmer fluid (such as moist air) passes over them. Throughout this interaction, heat is transferred from the warmer fluid to the cooler one. Because of this, metals with high thermal conductivity, such as copper and aluminum, are frequently used in the production of the heat exchangers. However, copper and aluminum are both naturally hydrophilic. In some heat transfer applications, water will condense on to the heat exchanger surface, which can lead to inefficiencies in the system. This condensation can block airflow and can also pose a significant resistance to heat transfer through the tube and/or fin. Naturally hydrophilic materials are also not capable of shedding this condensate very well, resulting in compounding inefficiencies. This research is thus aimed at developing a solution that can mitigate these effects.

One possible strategy is to alter the surface wettability (i.e. the degree of hydrophobicity or hydrophilicity that a surface exhibits). Several methods can be applied to alter the surface wettability, including modifying the surface chemistry or adjusting the surface roughness [5–8]. These changes can bring a number of benefits. For example, the altered surface may better shed condensated water from the surface, thereby reducing the amount of thermal resistance posed by

the condensate. This study will characterize amorphous silica nanosprings, a recently discovered surface coating, which have the potential to significantly improve heat transfer performance while also having advantages over other current alternatives. These include the surface being grown under relatively mild growth conditions [9], being able to conformally coat both two- and three-dimensional substrates [10,11], and being photolithography compatible for controlling regions where the nanosprings are allowed to grow [12–14].

2.0 LITERATURE REVIEW

2.1 Uniform Surface Enhancements for Improving Condensation Heat Transfer

One method for improving the condensation heat transfer efficiency is to alter the surface wettability to make it either more hydrophobic or hydrophilic with the intention of promoting either dropwise condensation or filmwise condensation, respectively [15,16]. A number of studies have shown that the formation of dropwise condensation is more beneficial to improving condensation heat transfer than filmwise condensation. With filmwise condensation, a thin layer of water forms over the surface acting as additional resistance to heat transfer. In contrast, dropwise condensation is characterized by individual water droplets nucleating on the surface. This, in turn, offers less resistance to heat transfer due to regions of the underlying surface remaining exposed to the surrounding air. The surface is also more likely to shed the condensed liquid at a higher rate than filmwise condensation due to the hydrophobic nature of the surfaces. A side-by-side comparison of filmwise and dropwise condensation is presented in Fig. 1, which is taken from Preston et al. [17], which will be discussed later in this document.

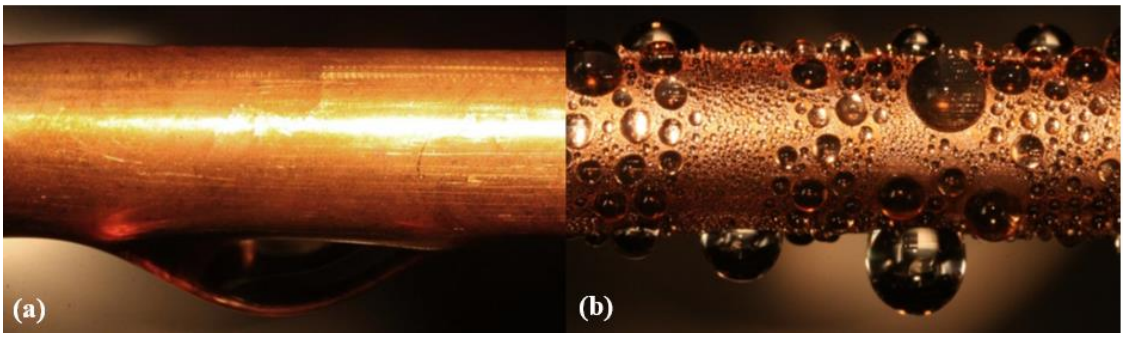

Figure 1. *Comparison of (a) filmwise condensation and (b) dropwise condensation. Taken from [17].*

In a study by Das et al., organic self-assembled monolayer (SAM) coatings were applied to a copper tube, a copper-nickel alloy tube, and gold-coated-aluminum tube in the hopes of promoting dropwise condensation to improve the condensation heat transfer coefficient [18]. The monolayer hexadecylthiol, $HS(CH_2)_{15}CH_3$, had a thickness of 10 to 15 Å which resulted in a negligible resistance to heat transfer. The wettability of these SAM coatings was characterized by the use of static contact angle measurements. With static contact angles ranging from 110º to 112º, these surfaces were shown to be hydrophobic. Steam condensation tests were conducted in a boiler

capable of holding a vacuum to determine the condensation heat transfer coefficient of each tube. The purpose of the vacuum was to remove all the non-condensable gases. This methodology is common practice in condensation heat transfer experiments to improve the accuracy of the experimental results and allow for comparisons between differing experiments. A study by Tanner et al. showed that the presence of non-condensable gases resulted in decreased condensation heat transfer performance over a case without non-condensable gases [19]. A diagram of the Das group's experimental setup and test section from [18] is shown in Fig. 2. With the use of the hexadecylthiol SAM coatings on the copper and copper-nickel tubes, the group was capable of obtaining condensation heat transfer improvements of up to 5 times higher than the baseline aluminum tubes under vacuum conditions. However, the study did not include an evaluation of the durability of the SAM coating during prolonged exposure to operating conditions.

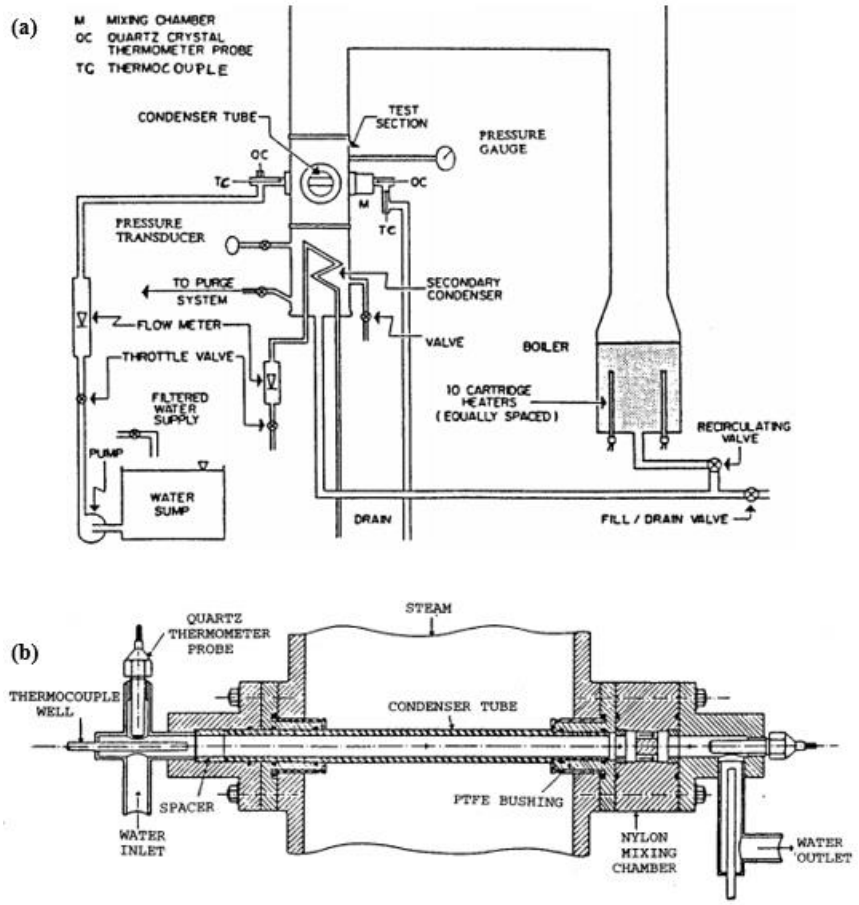

Figure 2. *The (a) experimental setup and (b) test section used by Das et al. to conduct condensation heat transfer experimentation. Taken from [18].*

Another method of promoting dropwise condensation was investigated by Preston et al., in which a chemical vapor deposited (CVD) graphene coating was applied to copper tubes [17]. A furnace at 1000°C was used in order to apply the coating, which limits the materials that are capable of being coated in graphene. Two different approaches were used to apply the graphene coating: atmospheric pressure chemical vapor deposition (APCVD) and low-pressure chemical vapor deposition (LPCVD). The LPCVD process was applied at a pressure of approximately 250 Pa (1.9 torr). The surface wettability after applying the coating was characterized with average advancing/receding contact angle measurements of 87º/64º for the LPCVD and 93º/56º for the APCVD. Tests were also conducted within a vacuum chamber with water as the condensing fluid. These condensation tests determined that the graphene coating could increase the condensation heat transfer coefficient by 400% over a bare copper tube. Durability testing also revealed that the graphene-coated tubes were capable of maintaining dropwise condensation production throughout the duration of a two-week test with no major signs of degradation.

A method for developing superhydrophobic surfaces where copper tubes were infused with silicone oil for the improvement of heat transfer performance was investigated by Tsuchiya et al. [20]. The fabrication of these surface was completed by a sol-gel reaction, detailed by Tenjimbayashi et al., where the surface is exposed to a precursor that is tethered to the surface in order to modify surface wettability [21]. The liquid infused surfaces had static contact angle measurements as high as 154º, which means they can be characterized as superhydrophobic. Using these liquid-infused surfaces, heat transfer coefficients that were 175% higher than the heat transfer coefficients of the uncoated surface were reported. Durability concerns, however, were the main drawback of these oil-infused tubes. Throughout testing, it was shown that the infused oil was depleted by the condensation over time resulting in decreased performance over prolonged testing conditions.

Aside from chemical coatings, topographical modifications to surfaces can also be used to alter the surface wettability. In a work by Wen et al., copper nanowires with diameters ranging from 200-240 nm were deposited on flat copper plates [22]. The group used the nanowires to create nano-roughness on the surface, altering the surface wettability to make it more hydrophobic. This allowed for the promotion of dropwise condensation to improve the heat transfer performance. The copper nanowires were placed using a two-stage electro-deposition process, where the length of the nanowires varied with the duration of the deposition process. Afterwards, the surface was

immersed in a 70℃ ethanol solution of 2.5 mM *n*-octadecanethiol for hydrophobic functionalization. This process was first demonstrated by Porter et al. [23]. A functionalized hydrophobic copper surface without nanowires was also prepared using this method. The average static contact angle measurement after applying the nanowires was 139.2º, which was higher than the reported value of 114.6º for the hydrophobic surface without nanowires. The Wen group showed that the heat transfer coefficient is highly sensitive to the amount of subcooling experienced between the cooling fluid and the condensing fluid. By depositing the copper nanowires, heat fluxes 100% higher than the baseline hydrophobic surface were obtained.

Zhao et al. investigated structured tubes for their ability to improve condensation heat transfer with R134a and R404A as condensing fluids [24]. Two- and three- dimensional fins structures were created on iron-cupronickel and aluminum-brass tubes. Similar to other works, testing was conducted within an evacuated chamber to remove non-condensable gases. Within this study, the goal was to identify the effect of varying the thermal conductivity and condensing fluid on heat transfer performance. The Gnielinski relation was used to reduce the data gathered throughout testing [25]. It was shown that the higher thermal conductivity fluid resulted in a higher heat transfer coefficient, and the three-dimensional finned surface increased the heat transfer performance more than the two-dimensional structure. However, no testing was conducted on baseline unstructured tubes. Thus, no comparisons could be made between these structures and a baseline case.

A superhydrophobic silicon nanopillar surface enhancement was evaluated as an option for improving heat transfer performance by Miljkovic et al. [26]. To fabricate the pillars on the flat surface, both e-beam lithography and deep reactive ion etching (RIE) processes were used. The silicon nanopillars had diameters, heights, and center-to-center spacings of 300 nm, 6.1 μm, and 2 μm respectively. The goal of this study was to determine how the heat transfer performance varied under two different wetting conditions: partially wetting droplets and suspended droplets. For the partially wetting droplets, liquid can be found between the pillars, while suspended droplets rest fully on top of the structures. Through testing, the group found that when the condensation was dominated by partially wetting droplets, the heat flux improved by 71% over an unstructured hydrophobic surface. For the suspended case, the heat flux improvement was only 56% over the hydrophobic surface. Based on a thermal resistance model, the group identified that the difference was caused by the presence of an insulating air layer that provides additional thermal resistance in

the suspended droplet scenario, revealing the importance of identifying and characterizing the air layer when modeling heat transfer.

A study by Rajkumar et al. combined the effects of a chemical coating and surface topography alterations to improve the condensation heat transfer capabilities of vertical copper tubes [27]. In order to make the tubes hydrophobic, a 10 μm lead coating was electrodeposited onto the surface of the tube. Each tube also had four grooves milled into the surface with a 90º spacing about the tube axis and running parallel to the axis of the tube. These grooves were intended to reduce surface contact, allowing for accelerated droplet removal. Within this experiment, the impacts of applying the lead coating and varying the groove depth on condensation heat transfer were investigated. Similar to the results found in Wen et al. [22], the group found that the condensation heat transfer coefficient was highly sensitive to the degree of subcooling as shown in Fig. 3. The presence of the lead on the copper tube also increased the heat transfer coefficient over the uncoated tube. Similarly, the presence of the grooves also improved the performance. To determine the effects of combining the lead coating and the groove depths, comparisons were made to the lead-coated-copper tube without grooves. These comparisons revealed that the combination was only beneficial at lower degrees of subcooling less than 2°C, while the lead-coated tube without grooves was superior at higher degrees of subcooling.

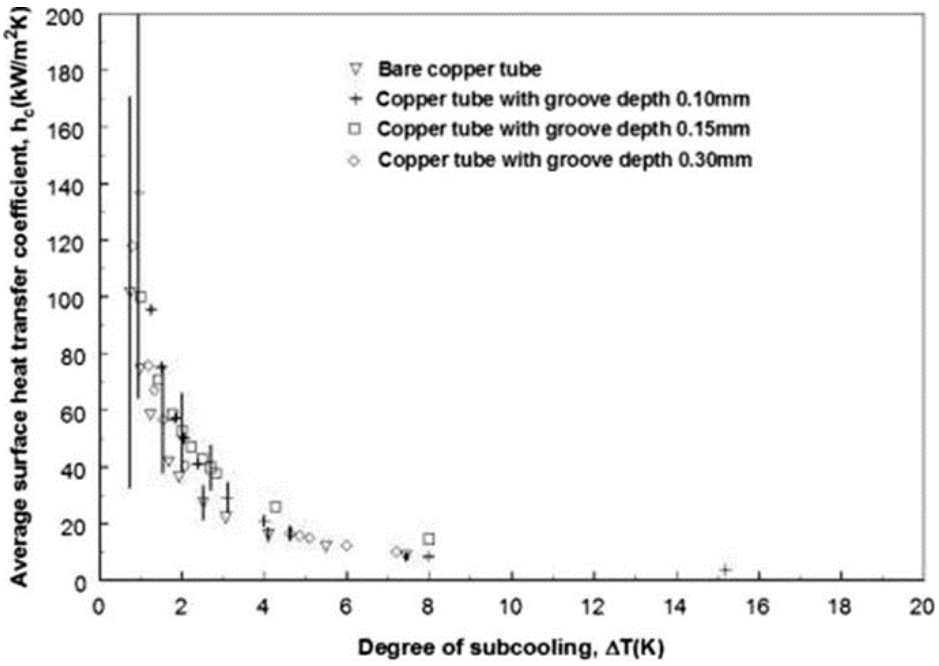

Figure 3. *Plot showing the strong relation between the condensation heat transfer coefficient with respect to the degree of subcooling. Taken from [27].*

2.2 Hybrid Wettability Patterning for Improving Condensation Heat Transfer

A number of studies have also been conducted in which the authors have manipulated the surface wettability to have localized regions of hydrophobicity and hydrophilicity. By doing so, the researchers hoped to gain the benefits that each type of surface wettability has to offer, as well as promote different forms of condensation behavior that cannot be created by a uniform wettability. This can include promoting easier and more frequent droplet removal from the surface in order to increase the heat transfer capabilities.

In experiments by Yang et al., hybrid wettability surfaces were created and compared to uniformly hydrophilic, hydrophobic, and superhydrophobic surfaces [28]. A flat surface was manufactured with alternating hydrophobic and hydrophilic regions oriented in a V-shape pattern. To create this pattern, a screen-printing process was used to create a mask to cover the regions of the copper surface that would remain naturally hydrophilic. Then, the masked surface was sprayed with ethyl nonafluorobutyl ether to create the hydrophobic regions, after which the mask was removed. A range of surrounding airflow velocities were used in this experiment. From the testing, the group discovered that the hybrid patterned surface performed better than the other tested surfaces independent of the velocity. Heat transfer coefficients ranging from 3% to 9% higher than the hydrophobic surfaces were observed while 6% to 16% increases over the hydrophilic surface were observed.

Nature inspired some of the earliest works with patterned surfaces and continues to inspire new patterns to this day. Ghosh et al. created a hydrophilic-superhydrophilic patterned surface that was intended to mimic the behavior of banana leaves [29]. Similar to the fabrication process implemented by Yang et al. in [28], Ghosh et al. created the surface using a masking process. In this work, a protective polymer sheet was placed on an aluminum surface, and then the desired pattern was cut into the polymer sheet using a carbon dioxide (CO_2) laser. The wettability of the unmasked region was altered by immersing the surface in a hydrochloric acid solution, resulting in localized superhydrophilic regions. As before, the underlying aluminum substrate was considered to be naturally hydrophilic. With the use of the patterned surface, the condensation heat transfer testing revealed that improvements of up to 20% higher than the baseline aluminum surface could be achieved.

In a two-part study by Alwazzan et al., the optimization of an alternating hydrophobic-hydrophilic pattern on horizontal copper tubes was investigated for improving heat transfer

performance [30,31]. A photo-resist sheet was patterned using a printed transparency as a photolithographic mask. Exposure to an ultraviolet light source caused the areas not blocked by the ink on the photoresist sheet to become brittle, while the regions blocked by the ink on the transparent sheet remained unchanged. The photoresist sheet was then wrapped around the copper tubes. Sandblasting was used to disintegrate the brittle portions of the photoresist sheet and create surface roughness on the underlying portions of the tube. After removing the remaining photoresist mask, the surface was immersed in a solution of *n*-octadecyl mercaptan and ethanol for additional hydrophobicity. This process resulted in alternating surface wettability rings along the tube. Varying ratios of hydrophobic ring width to hydrophilic ring width were tested to optimize the surface pattern. These tests suggested that the optimum ratio was a hydrophobic region two times wider than the hydrophilic region. The optimized hybrid surface was capable of achieving a heat transfer coefficient 480% higher than a filmwise condensation (hydrophilic) tube and 180% higher than a dropwise condensation (hydrophobic) tube. Alwazzan et al. also hypothesized that using different wettabilities may result in different optimal ring width configurations.

2.3 Growth and Characterization of Silica Nanosprings

Silica nanosprings (SN) are a surface coating that has characteristics that may be conducive to improving condensation heat transfer. The SN were discovered in the lab of Dr. David McIlroy as documented by Wang et al. [32]. SN are made of amorphous silica that is grown into a high-surface area, one-dimensional nanomaterial surface coating. Mild growth conditions (relative to other surface coatings and other one-dimensional nanostructures) are used to produce the SN [9]. The growth process takes place at atmospheric pressure and temperatures around 350°C. SN grow via a vapor-liquid-solid (VLS) mechanism that is discussed in depth in [9]. To briefly describe the growth procedure, first the surface is sputtered with a layer of gold catalyst. The gold-coated surface is placed in a programmable chemical vapor deposition (CVD) reactor and exposed to a silane precursor for a prescribed period of time. The greater the duration of precursor exposure, the longer the nanosprings can grow resulting in a thicker SN mat over the surface.

Multiple studies have been conducted to determine how the helical structure of the silica nanosprings form. McIlroy et al. stated that nanosprings could only form from amorphous nanowires [9]. The early stages of SN growth are documented using electron microscopy in Wojcik et al. [33]. High resolution transmission electron microscope (TEM) images show the gold catalyst

particle at the tip of the nanosprings, each of which is composed of multiple nanowires. These TEM images can be found in Fig. 4. Scanning electron microscope (SEM) images were also collected from samples early in the growth procedure, which are presented in Fig. 5. These images show that each nanospring is composed of multiple structures that begin as individual nanowires. These nanowires eventually come together and group at their Au-Si catalyst tips. This connection point causes the nanowires to interact and intertwine with one another, producing the helical structure of the SN as the nanowires continue to grow. To represent this growth process, a 3D model rendering of an individual nanospring has been provided in Fig. 6. In [32], it was shown that each nanospring is made up of five to eight nanowires.

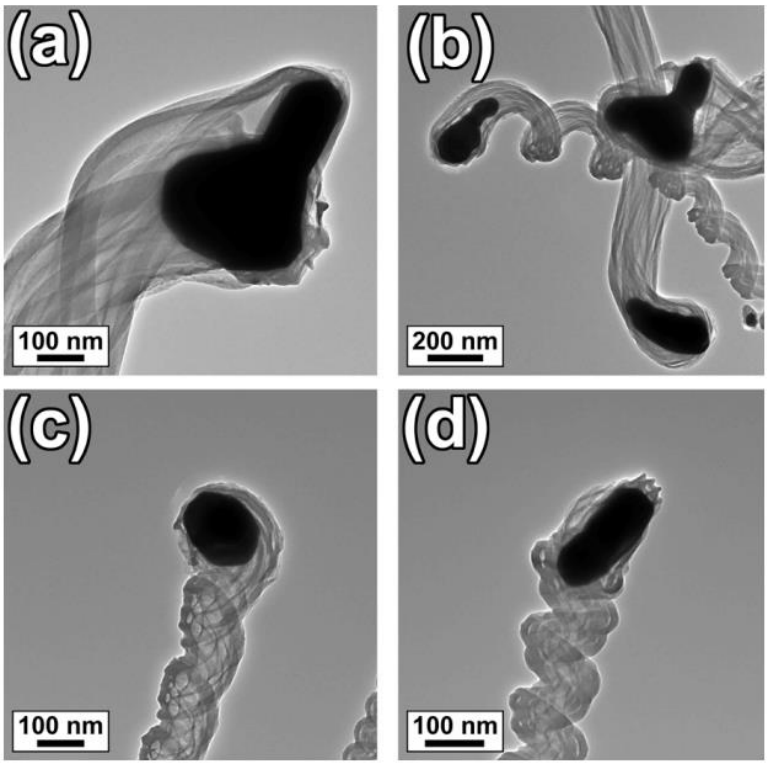

Figure 4. *Brightfield TEM images of silica nanosprings showing that each spring is composed of multiple silica nanowires with a gold particle at the tip. Taken from [33].*

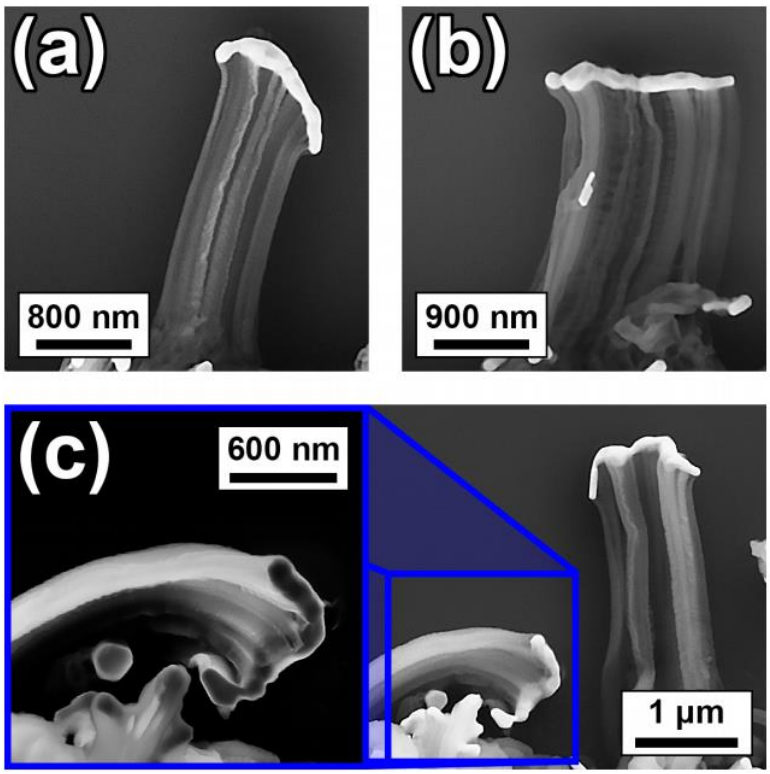

Figure 5. *Secondary electron SEM images showing the early stages of silica nanospring growth. These images show the individual silica nanowires coming together and meeting at the Au-Si tips, shown in white. These tips pinch together, causing the helical structure to begin as shown in (c). Taken from [33].*

Figure 6. *Rendering of a single nanowire structure showing multiple nanowires coming together and intertwining to form the nanospring.*

The SN coating has not yet been investigated for its ability to improve condensation heat transfer. However, a number of works have been performed that have partially characterized the coating which suggest the coating should perform well in a condensation heat transfer environment. For example, work by Schilke et al. has shown that the SN coating is thermally stable at temperatures below 1000°C and are capable of being functionalized [34]. SN are made of silica, thus their surface is terminated with free hydroxyl groups allowing the springs to chemically bond with both organic and inorganic materials [34–36]. This bonding can be performed using a variety of common surface techniques such as vapor and liquid deposition [10,34]. Due to the porosity of the SN mat, it may be desirable to transport water from the underlying surface to the top of the coating. In a study by Hass et al. it was shown that applying proper functionalization can allow for moisture wicking through the SN mats [35].

Furthermore, the growth rates of the silica nanosprings in these studies were approximately 2.5 μm per minute, which was shown to be about 40 mg per hour of growth for a 24 cm^2 sample [37]. Brunauer–Emmett–Teller (BET) measurements showed that SN have ~350 m^2g^{-1} of accessible surface area [38]. A significant benefit of the SN coatings is the conformability to coat a wide variety of two-dimensional and three-dimensional surfaces, including complex geometries, given that the surfaces can withstand the growth conditions [10,11,39,40]. Finally, photolithography has been used previously to pattern where nanosprings grow on a surface, showing that patterned surfaces can be generated using the silica nanospring coating [12–14].

3.0 PROJECT DEFINITION

The intent of this project is to study and characterize a silica nanospring coating as a means to enhance condensation heat transfer performance on horizontal aluminum tubes, while also systematically studying the parameters that influence the heat transfer performance. Simultaneously, further characterization of the growth and physical structure of the nanosprings will also be conducted. The coating will be characterized in terms of surface wettability, mat thickness, condensate drainage rate, and the robustness of the coating.

The effect of applying the silica nanospring coating to metallic substrates has not yet been studied from a heat transfer perspective. While surface modifications for developing hydrophobic tendencies on substances such as silicon and glass have been extensively investigated in recent years, similar works using metallic substrates remain relatively unstudied. Similarly, studies involving hybrid patterned surfaces for improving heat transfer performance have also been sparsely conducted. As a result, this study aims to further characterize silica nanospring coatings in order to develop strategies for implementation in real-life systems and applications.

4.0 METHODOLOGY

4.1 Experimental Test Setup

In order to assess the heat transfer performance of each test sample, condensation heat transfer experimentations were carried out within a controlled environment chamber. The controlled environmental chamber consisted of a well-insulated vacuum chamber containing water as the condensing fluid. As previously mentioned, the purpose of performing tests within an evacuated chamber was to remove any non-condensable gases, which can have a significant impact on the condensation heat transfer performance of each sample [19]. Thus, testing within a vacuum chamber allowed for direct comparison of the performance for each sample. Through this experimentation, testing parameters were set and recorded for use in calculating different metrics of comparison. The parameters being monitored included the cooling fluid flowrate, the degree of subcooling between the chamber environment and the cooling fluid at the inlet of the tube ($\Delta T_{subcooling}$), the cooling fluid temperature at the inlet and the outlet of the tube ($T_{m,in}$ and $T_{m,out}$), the tube surface temperatures at the inlet and the outlet ($T_{s,in}$ and $T_{s,out}$), and the interior pressure of the test chamber (P_{sat}). A schematic of the test setup is presented in Fig. 7.

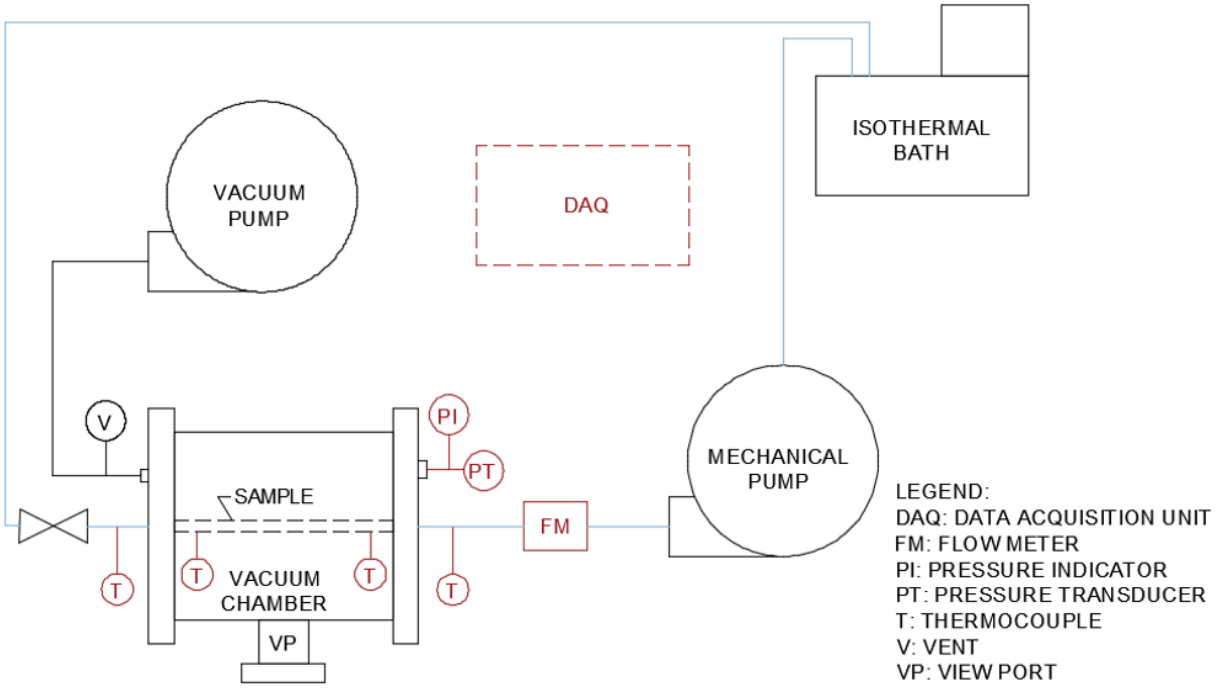

Figure 7. *Schematic of the test setup used for conducting condensation heat transfer testing.*

The test setup exterior, shown in Fig. 8a, is composed of a Neslab RTE-10 isothermal bath (1) intended to control and maintain the cooling fluid inlet temperature. The cooling fluid flows through the test sample by means of a Leeson motor driven pump (2), while the flowrate is monitored by a McMillan Co. 112 Flo-Meter (3). After the flow meter, the cooling fluid then flows through the test sample, which is housed within an ISO-200 controlled environment vacuum chamber (4). This chamber is well-insulated in order to ensure that any heat transfer that may occur between the interior and the exterior of the chamber is negligible. An Adixen mechanical vacuum pump (5) is used to evacuate the chamber, removing any non-condensable gases. An Agilent 34972A data acquisition unit (DAQ) (6) is used to record the temperature, pressure, and flowrate data that is measured throughout testing. For this experimentation, it was important that the condensation formation of water only takes place on the test sample, not the walls of the surrounding chamber. Because of this, a heating pad was wrapped around the outside of the environmental chamber to keep the chamber wall temperature sufficiently high enough to prevent condensation formation on these surfaces. The temperature of this heat wrap was controlled with the use of a SOLO 4848 PID controller (7).

All temperature measurements recorded during testing were measured using Omega T-type thermocouples that were previously calibrated using an Isotech F200 high precision resistance temperature detector (RTD) (see Section 10.1 of the Appendix). The calibrated precision of the thermocouples and the accuracy of the other measurement devices in the test setup can be found in Table 1. Within the evacuated chamber, shown in Fig. 8b, two thermocouples were used to monitor the sample (8) surface temperature. These thermocouples (9) are held firmly to the sample surface by wrapping Teflon tape around the thermocouple in contact with the tube sample and then tightening a plastic hose clamp around the connection to ensure the thermocouple remains in contact with the surface. The Teflon tape also helps prevent condensation from coming into contact with the thermocouples. An additional thermocouple (10) is used to record the temperature of the moist air surrounding the test sample. The test sample and all wiring (thermocouples, lighting, etc.) on the interior of the test chamber have been delivered using vacuum suitable Swagelok fittings or high vacuum rated Omega fittings. An Omega PX309 digital pressure transducer is used to monitor the pressure within the chamber, and a viewport in the chamber wall allows for the collection of still images and video during testing. The condensing fluid used during testing was water, so prior to pulling a vacuum, 2 liters of deionized water (11) were supplied to the chamber.

Thus, after pulling a vacuum the surrounding environment consisted of saturated water vapor. Additional images of the test chamber and test setup components can be found in the Section 10.2 of the Appendix.

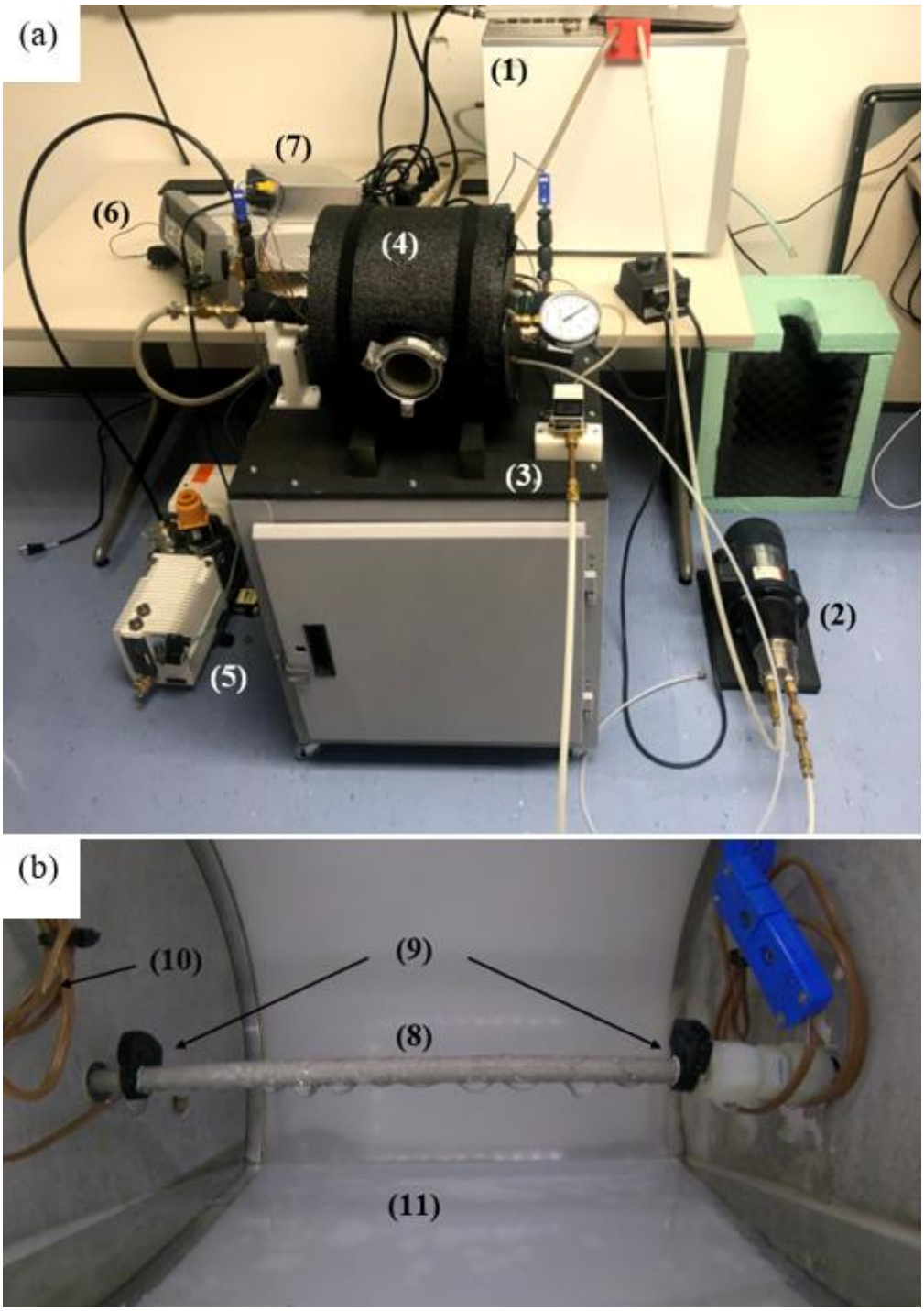

Figure 8. *Images of the (a) exterior and (b) interior of the evacuated controlled environment chamber used to conduct condensation heat transfer experimentation.*

Table 1. *Accuracy of devices used for data collection within the test setup.*

Device	Range of Use	Accuracy
Flow meter	0 to 10 LPM	±3%
Pressure transducer	0 to 350 kPa	±1%
Cooling Fluid Inlet Thermocouple	-270 to 370°C	±0.035°C*
Cooling Fluid Outlet Thermocouple	-270 to 370°C	±0.027°C*
Surface Inlet Thermocouple	-270 to 370°C	±0.025°C*
Surface Outlet Thermocouple	-270 to 370°C	±0.044°C*

** Thermocouple accuracies have been calibrated using an RTD over a range of temperatures expected to be experienced during testing.*

4.2 Testing Procedure

In order to conduct a condensation heat transfer experiment, first the prescribed cooling fluid flowrate and the degree of subcooling between the surrounding environment and the cooling fluid at the sample inlet are set using the pump and the isothermal bath respectively. After setting these parameters, a sufficient period of time is allotted in order to allow the system to reach thermodynamic equilibrium. During this time, slight adjustments to the flowrate and cooling fluid temperature may be made in order to maintain the desired testing parameters. A representative plot of the system reaching equilibrium can be seen in Fig. 9. Once thermodynamic equilibrium has been reached, a data collection period of 120 seconds commences in which the previously described test data is recorded with a frequency of 1 Hz. After this data collection period, the flowrate of the cooling fluid is altered, and the system is again allowed time to reach thermodynamic equilibrium. This process repeats until all the necessary data has been collected. In this study, each sample has been tested at 1.5, 3.3, and 9.5°C of subcooling and flowrates ranging from 1.5 to 5.5 LPM in 0.5 LPM increments.

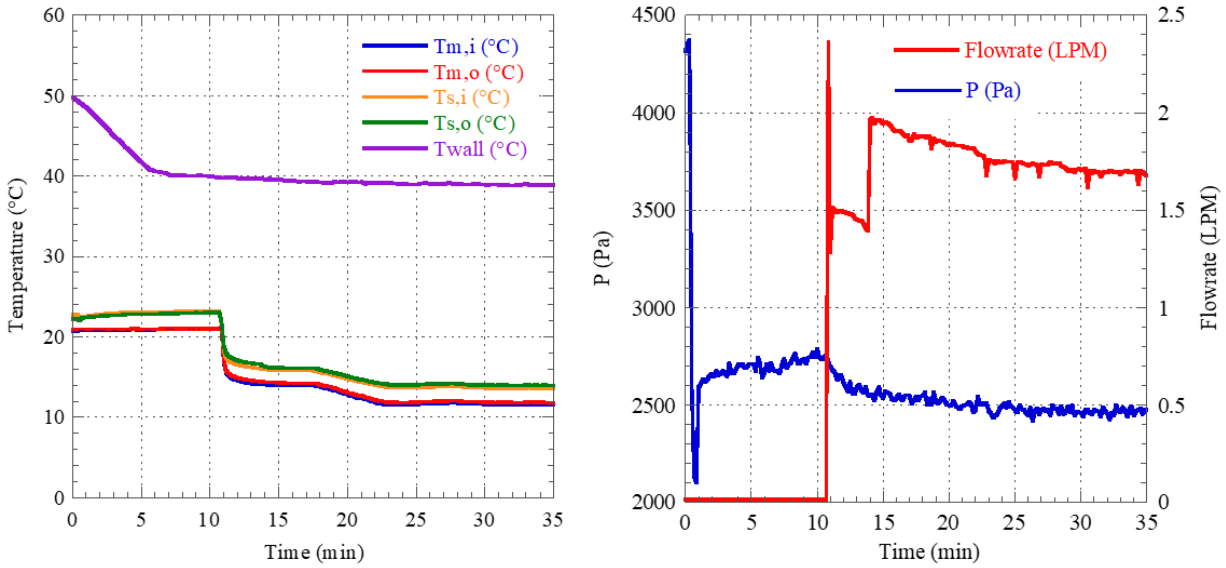

Figure 9. *Plots showing the test setup reaching an equilibrium point after approximately 30 minutes.*

4.3 Calculation of Heat Transfer Coefficient (Method 1: Constant Tube Surface Temperature)

Using the data collected during testing, the condensation heat transfer coefficient is calculated in order to make comparisons between samples. There are a number of different methods that can be used to calculate this metric depending on the testing scenario and flow characteristics. For this study, multiple correlations are used for data reduction, and the most appropriate method will be used for presenting the findings. The first method that is considered is the constant tube surface temperature method. In order for this method to be valid, the surface temperature along the length of the tube must be approximately uniform. Because of this, the thermocouple measurements taken at the inlet and the outlet of the tube will be used to access the validity of this method (i.e. Method 1). Equation (1) represents the balance of the heat transferred from the cooling fluid with respect of the heat transferred from the tube surface to the surrounding environment

$$\dot{m}c_p\left(T_{m,out} - T_{m,in}\right) = \bar{h}A_s\left(T_\infty - T_{s,avg}\right), \tag{1}$$

where $\dot{m}$ is the water coolant flow rate, c_p is the water heat capacity, $T_{m,out}$ and $T_{m,in}$ are the water coolant inlet and outlet temperatures, $\bar{h}$ is the convective heat transfer coefficient, A_s is the tube surface area exposed to the surrounding environment, T_∞ is the chamber internal temperature and

$T_{s,avg}$ is the average surface temperature of the tube. Eq. (1) can then be rearranged to solve for the condensation heat transfer coefficient

$$\bar{h} = \frac{\dot{m}c_p\left(T_{m,out} - T_{m,in}\right)}{A_s(T_\infty - T_{s,avg})}. \tag{2}$$

4.4 Calculation of Heat Transfer Coefficient (Method 2: Constant External Fluid Temperature)

If the tube surface temperature is not constant, then a different data reduction methodology is necessary. An alternate method is the thermal resistance model based on a constant external fluid temperature (i.e. Method 2). In this method, the heat transfer coefficient is determined using the total thermal resistance and the individual thermal resistance components. In this case, the total thermal resistance consists of the convective resistance between the inner tube wall and the cooling fluid, the conduction resistance created by the tube wall, and the convective resistance between the outer tube wall and the surrounding vapor. The total thermal resistance is shown in Eq. (3) below:

$$R_{tot} = R_i + R_{wall} + R_o, \tag{3}$$

where, R_{tot} is the total thermal resistance, R_i is the convective resistance on the interior of the tube, R_{wall} is the thermal conduction resistance through the tube wall, and R_o is the convective resistance on the outside of the tube. The total thermal resistance can be calculated using the average overall heat transfer coefficient ($\bar{U}$) as

$$R_{tot} = \frac{1}{\bar{U}A_o}, \tag{4}$$

where the average overall heat transfer coefficient, $\bar{U}$, is:

$$\bar{U} = \left(\frac{-\dot{m}c_p}{A_o}\right) * \ln\left(\frac{T_\infty - T_{m,out}}{T_\infty - T_{m,in}}\right). \tag{5}$$

The thermal resistance R_i between the interior wall and the cooling fluid can be calculated using Eq. (6):

$$R_i = \frac{1}{h_i A_i}, \tag{6}$$

where h_i is the interior heat transfer coefficient and A_i is the interior surface area of the tube. Since Eq. (6) is dependent on the interior heat transfer coefficient h_i, a relationship is required to determine this quantity. There are a number of correlations that have been proposed in the literature depending on the heat transfer scenario and the flow conditions. In this study, the tested flow rates fall within the turbulent flow regime with the Reynolds numbers (Re) significantly higher than 2300. An equation was proposed by Gnielinski for calculating the heat transfer coefficient for turbulent flows within smooth tubes such that [25]:

$$Nu_D = \frac{(f/8)(Re_D - 1000)Pr}{1 + 12.7(f/8)^{\frac{1}{2}}\left(Pr^{\frac{2}{3}} - 1\right)}, \tag{7}$$

where

$$h_i = Nu_D * \frac{k}{D_i}. \tag{8}$$

In Eq. (7), the Nusselt Number, Nu_D, is dependent upon the Reynolds and Prandtl numbers, Re_D and Pr respectively. The Darcy friction factor, f, appears in this equation. The Gnielinski relation is valid for flows where $3000 < Re_D < 5 \times 10^6$ and $0.5 < Pr < 2000$.

Multiple recommendations have also been made for calculating this friction factor, which is dependent on the flow characteristics. Three of these recommendations include the Colebrook correlation [41], Petukhov correlation [42], and Blasius correlation [43]. The Colebrook correlation, shown in Eq. (9), is intended to be used for flows where $Re > 4000$:

$$f = \frac{4}{(1.5635 * \ln(Re_D/7))^2}. \tag{9}$$

The Petukhov correlation, shown in Eq. (10), is intended to be used for flows where $3000 < Re < 5 \times 10^6$:

$$f = (0.790 * \ln(Re_D) - 1.64)^{-2}. \tag{10}$$

Finally, the Blasius correlation, shown in Eq. (11), was developed for fully developed, turbulent flow in hydraulically smooth tubes where $Re < 2 \times 10^4$:

$$f = 0.316 Re_D^{-\frac{1}{4}}. \quad (11)$$

The conductive thermal resistance through the wall is based on the geometry and material properties of the aluminum tube:

$$R_{wall} = \frac{\ln(D_o/D_i)}{2\pi L k}, \quad (12)$$

where D_o and D_i represent the inner and outer diameter respectively, L is the length of the tube, and k is the thermal conductivity of the tube walls.

Finally, the thermal resistance between the outer tube wall and the surrounding environment can be calculated as

$$R_o = \frac{1}{h_o A_o}, \quad (13)$$

where A_o is the exterior surface area of the tube and h_o is the condensation heat transfer coefficient of the tube. Substituting Eq. (13) into Eq. (3), the condensation heat transfer coefficient can be calculated, as shown in Eq. (14).

$$h_o = \frac{1}{A_o(R_{tot} - R_i - R_{wall})}. \quad (14)$$

It is worth noting that other relationships have been proposed for calculating the internal heat transfer coefficient h_i that can be substituted into Method 2 if necessary. This decision will be dependent on which correlation best fits the flow characteristics (e.g., Reynolds and Prandtl numbers) experienced during experimental testing. By using each of the methods discussed above, comparisons can also be made to check the data reduction methodology and perform an initial "self-check" at the beginning of an experiment. From these calculations, comparisons between the condensation heat transfer coefficients of the different samples can then be made to assess their ability to improve heat transfer performance. A program, created within the Engineering Equation Solver (EES) software, has been employed to perform these calculations. A script of this EES program can be found in Section 10.3 of the Appendix.

4.5 Sample Preparation

Tubes coated with silica nanosprings were compared to an uncoated baseline aluminum tube to assess the effectiveness of the SN coating on the heat transfer performance. The baseline sample was exposed to the same preparation and cleaning processes as the coated samples. The condensation heat transfer samples were created using aluminum 6061-T6 tubes with 6.35 mm (0.25 in.) outer diameters and 5.10 mm (0.20 in.) inner diameters purchased from McMaster-Carr. The length of tube evaluated during testing is 152.4 mm (6.0 in.). All samples were first rubbed with an abrasive pad and lightly sanded with a fine grit crocus sheet from Norton Abrasive K624 (grit greater than 500). Each sample was cleaned by rubbing with acetone and then dipping them in a deionized water bath. A similar cleaning was then conducted using ethanol instead of acetone. After cleaning, the silica nanospring samples were coated in the manner described in greater detail in Section 2.3 in the literature review.

Briefly, the growth process for the silica nanospring mat is as follows: first the samples were sputter coated with a layer of gold. The sputter coating duration for each of the samples in this study was 20 seconds. In order to get a uniform coating around the circumference of the tube, the samples were rotated during the sputtering process at a speed of 45 rpm using a battery-powered DC motor as can be seen in Fig. 10a. Plastic sheathes were placed on the ends of each condensation testing sample to set the test section length of 152.4 mm. This also allowed for uncoated regions on the test sample for better contact between the thermocouples and the tube surfaces. Samples to be used for SEM imaging and wettability assessment were also sputtered in the same manner. After sputtering, all three samples were placed in a programmable CVD reactor for identical growth conditions. This reactor was programmed to expose the samples to a silane precursor for a specified amount of time at a specified temperature. To reiterate, the longer a sample is exposed to the precursor, the thicker the nanospring mat becomes. Figs. 10b and 10c shows before and after images of a set of samples for the growth process within the reactor.

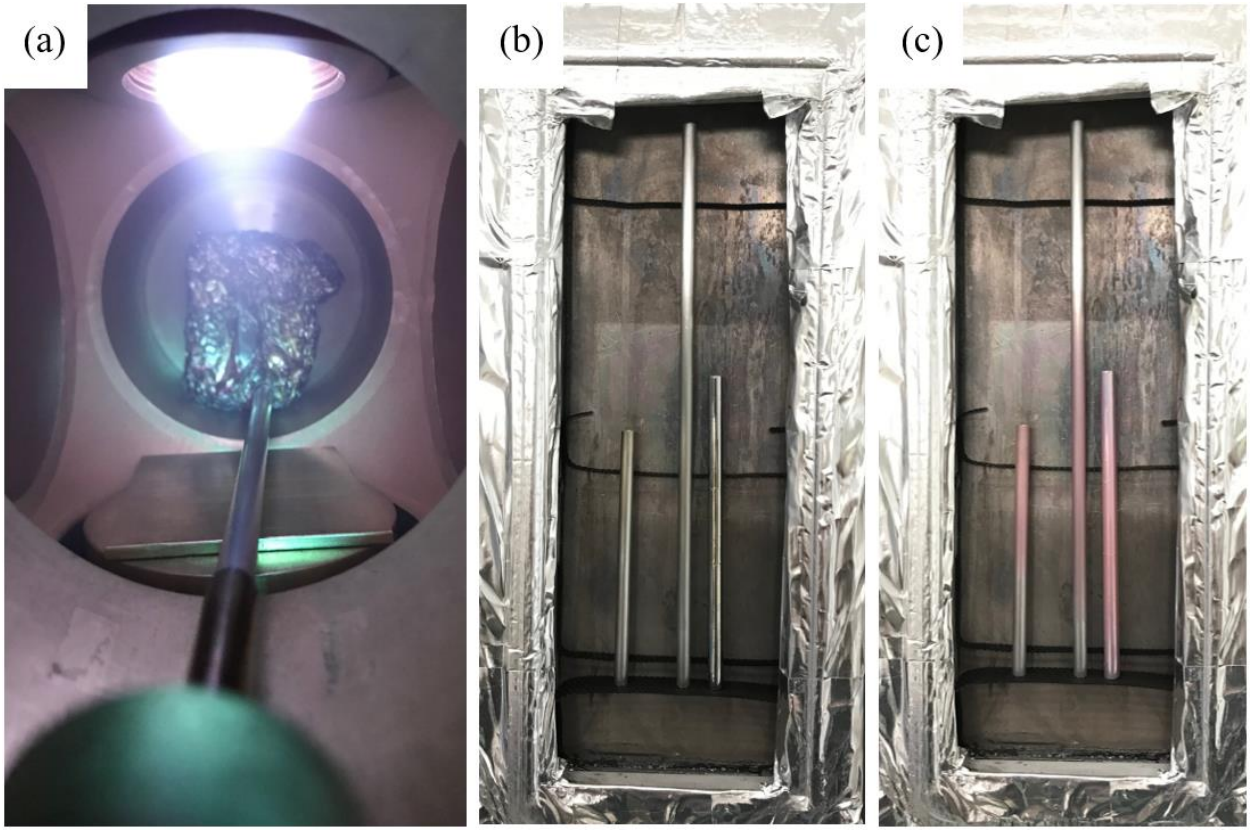

Figure 10. *Images of (a) a condensation test sample being sputter coated in gold while attached to a DC motor, and (b) before and (c) after silica nanospring growth images of samples within the CVD reactor.*

For the first part of this study, the goal was to determine if a uniform silica nanospring coating was capable of improving the condensation heat transfer performance of aluminum tubes, and which coating thickness performed the best. Because of this, multiple uniformly coated samples, each with a different growth duration and mat thickness, were created. Details of the surfaces considered for this study are provided in Table 2 below. Each of the samples uniformly coated in silica nanosprings was assigned a sample identification (ID), which contains the growth duration in minutes. In the remainder of this document, the samples will be referenced using this ID.

Table 2. *Samples being studied in this work.*

No.	Material	Surface Features	Growth Duration	Pattern?	Surface ID
S1	Al	Baseline Surface	--	No	Baseline
S2	Al	Baseline Surface + Uniform SN Coating	5 min	No	SN5
S3	Al	Baseline Surface + Uniform SN Coating	10 min	No	SN10
S4	Al	Baseline Surface + Uniform SN Coating	15 min	No	SN15
S5	Al	Baseline Surface + Uniform SN Coating	20 min	No	SN20
S6	Al	Baseline Surface + Uniform SN Coating	30 min	No	SN30
S7	Al	Baseline Surface + Patterned SN Coating	15 min	Yes	Patterned

4.6 Wettability Assessment

Within this work, characterizing the degree of wettability of each sample is important to assessing how hydrophobic or hydrophilic a surface is. The wettability has an impact on the type of condensation formation on each sample, as well as how easy it is for droplets to move on and shed from the surface. Contact angle measurements were taken for each sample to characterize the surface wettability. There are three types of contact angle measurements: static, advancing, and receding. With static contact angle measurements (θ_{static}), a droplet is placed on the surface and the angle formed between the surface and the droplet is measured. Advancing and receding contact angles are dynamic measurements, which can be measured using the sessile droplet method, demonstrated in Fig. 11. With advancing contact angle measurements (θ_{adv}), a static droplet is first placed on the surface. Then, a syringe is used to inject additional water into the droplet until the droplet begins to move (or advance) along the sample surface. The contact angle that is formed as the droplet first begins to move is the advancing contact angle measurement. Receding contact angle measurements (θ_{rec}) follow a similar process to advancing contact angle measurements; however, in this case, the syringe pulls water from the droplet rather than injecting water into the droplet. The contact angle that is formed just before the droplet first begins to move inward is the receding contact angle measurement. The difference between the advancing and receding contact angle measurements is known as the contact angle hysteresis (CAH), as shown in Eq. (15).

$$CAH = \theta_{adv} - \theta_{rec} \tag{15}$$

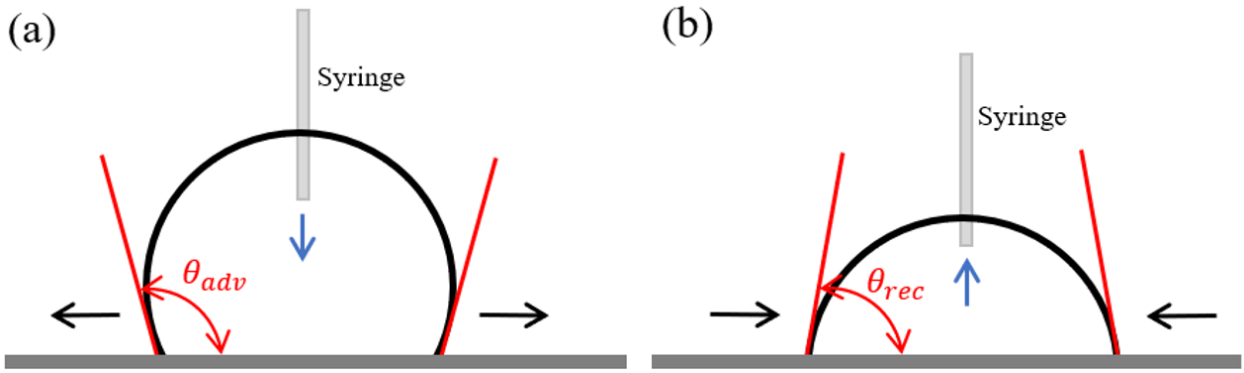

Figure 11. *Schematic of the sessile droplet method to measure (a) advancing and (b) receding contact angles.*

A combination of both the static contact angle measurement and the contact angle hysteresis values are used to characterize the surface wettability. Higher static contact angle measurements typically indicate that a surface is hydrophobic because the water droplet is being repelled away from the surface causing it to form into more of a sphere shape. The more hydrophobic a surface is, the closer the static contact angle measurement is to 180º. Samples with static contact angle measurements larger than 150º are generally considered to be superhydrophobic. With the contact angle hysteresis, the smaller the value is, the more hydrophobic a sample is.

A Ramé-Hart contact angle goniometer, shown in Fig. 12a, and DROPimage software was used to measure the contact angles of the samples in this study. The nominal droplet volume used for these measurements was 20 µL. In order to get an accurate representation of the samples created for this study, contact angle measurement samples were created using aluminum foil. A strip of aluminum foil was formed into a tube shape with a diameter comparable to the condensation samples. These aluminum foil tubes were then coated using the same silica nanospring growth process described above. These samples were placed in the CVD reactor at the same time as the condensation test samples to ensure they were exposed to identical growth conditions. After the growth process, the aluminum foil tubes were carefully unrolled and flattened into a semi-planar surface with care taken not to damage the coated area. After flattening, the sample was adhered to a planar substrate to keep the sample flat, as shown in Fig. 12b. Contact angle measurements were taken at various locations across the area of each sample. It is important to note that in the process of unrolling the aluminum foil samples the geometry of the silica nanospring mat was slightly compressed due to the geometry changes of the underlying substrate. This may impact the contact

angle measurements, but the measurements still allow for relative comparisons between the different samples being investigated.

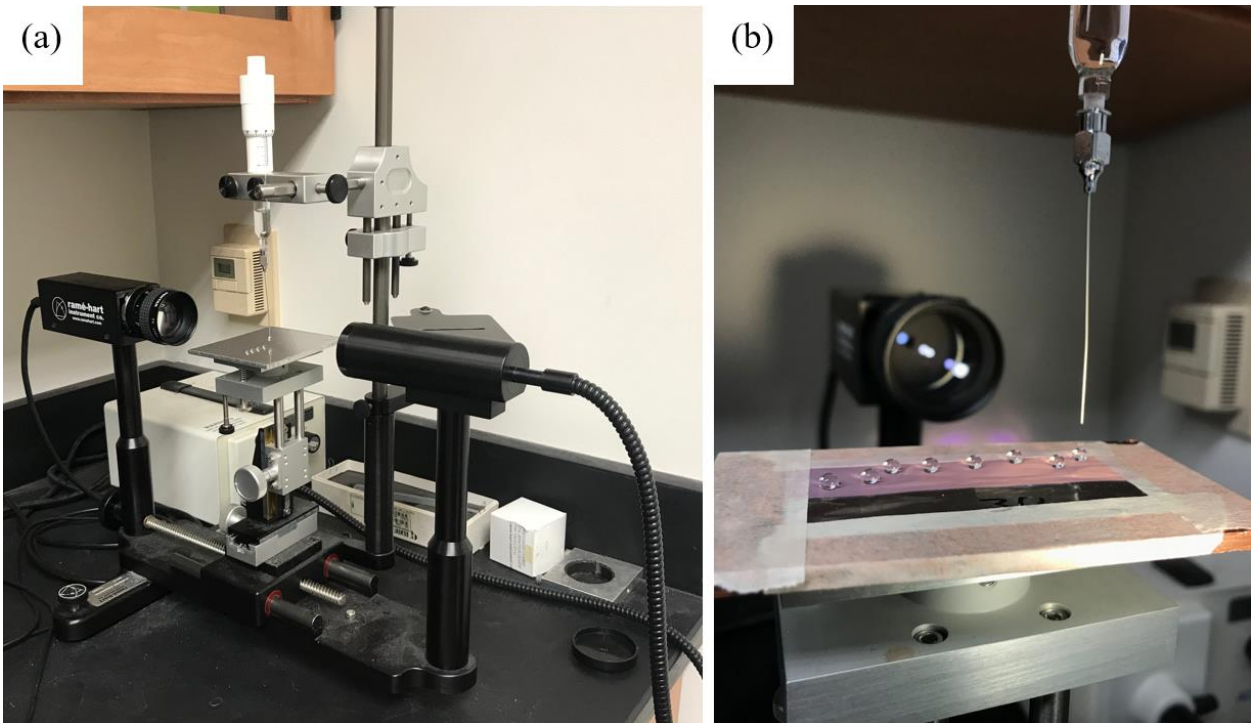

Figure 12. *Images of (a) the Ramé-Hart contact angle goniometer used for characterizing surface wettability, and (b) an unrolled silica nanospring-coated aluminum foil sample with contact angle measurements being taken across the sample area.*

5.0 RESULTS AND DISCUSSION

As a reminder, this project seeks to improve the condensation heat transfer performance of horizontal aluminum tubes through the application of an amorphous silica nanospring coating. Condensation heat transfer is commonly improved through the promotion of dropwise condensation, which is commonly achieved by adjusting surface wettability to a hydrophobic state. Previous studies incorporating the silica nanospring coating have shown the superhydrophobic capabilities of the coating [39,40]. The promotion of dropwise condensation is capable of improving condensation heat transfer performance by exposing regions of the underlying surface to direct contact the surrounding environment and decreasing the amount of thermal resistance posed by the condensate layer. Similarly, the hydrophobic surfaces commonly associated with the promotion of dropwise condensation are also commonly able to better shed water droplets from the surface, meaning less condensate is capable of lingering on the surface.

5.1 Silica Nanospring Mat Characterization

In the first part of the study, the goal was to fabricate and test samples with varying silica nanospring mat thicknesses. The mat thickness is dependent upon the amount of time the sample is exposed to the precursor during the growth process. Because of this, samples with uniform coatings were created by varying the precursor exposure time between 5, 10, 15, 20, and 30 minutes. In order to characterize each of the different samples and ensure that the nanospring mat formed properly, imaging was conducted using a Zeiss Supra 35 scanning electron microscope (SEM). As part of this work, the growth parameters required to produce nanosprings had to be modified in order to successfully produce the mat on the round tube surface. As a result, the parameters were iterated numerous times in order to obtain the best results. The goal was to produce nanosprings on the curved surface with more space between the springs than planar surfaces previously developed in the lab. By increasing this gap size, the underlying aluminum substrate was more exposed to the surrounding environment, meaning that the nanospring mat itself would pose less thermal resistance.

The first growth parameter modified was the amount of gold sputtered onto the surface before growth. The sputtering time was varied from 10 to 60 seconds in 10-second intervals. Through these samples, it was determined that having too much gold on the surface prevented springs from

launching from the surface due to the higher amount of energy required to form gold islands. In contrast, having too little gold resulted in the springs not being able to launch to form the nanospring mat. As a result, it was determined that the optimal sputter time of the samples evaluated was 20 seconds. This amount of gold allowed the springs to successfully launch from the surface while also expanding the gaps between springs over the previously developed planar surfaces. Because of this, the sputtering time for all the nanospring-coated surfaces in this study was established as 20 seconds.

For the growth process, the sample is first sputtered with a gold layer. As the CVD reactor heats up for the growth process, the gold on the surface migrates forming larger gold islands. This is important from a heat transfer perspective because these gold islands indicate the locations on the surface where silica nanosprings will launch. So, identifying the amount of area not occupied by the gold islands also indicates how much of the underlying substrate will be exposed to the surrounding environment. Characterization of the gold islands resulting from 20 seconds of sputtering was performed with a scanning electron microscope (SEM). These SEM images were then compared to images of a tube sample that was sputtered for 20 seconds and then placed in the CVD reactor. This sample was exposed to the growth process to a point just prior to when the precursor was introduced to the reactor. This method allowed the gold to migrate but prevented the springs from launching. Representative SEM images of each of these samples can be found in Fig. 13.

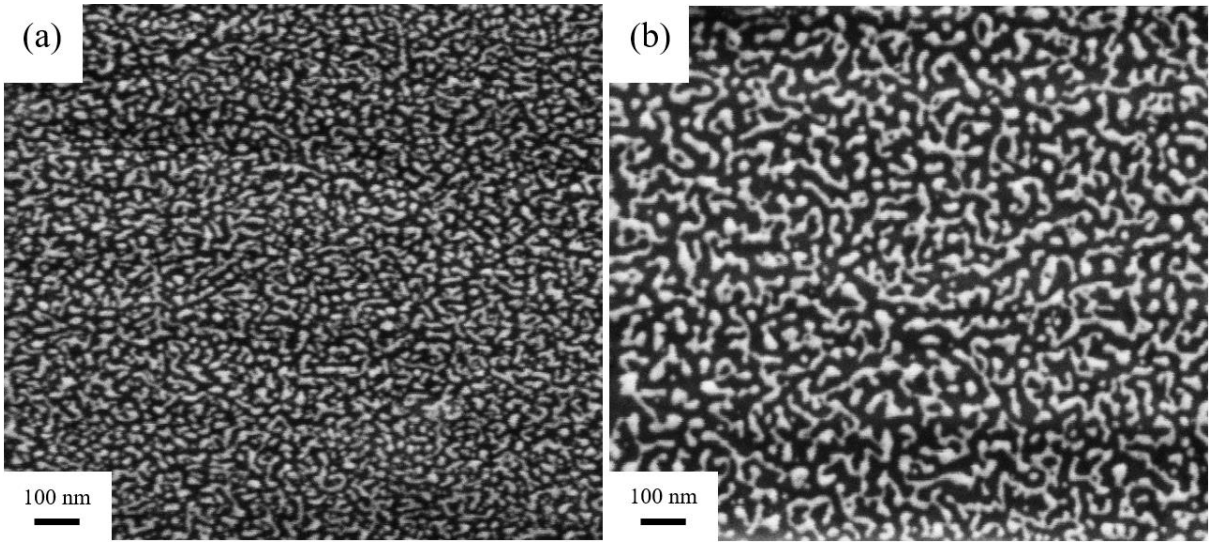

Figure 13. *SEM images of tube samples sputtered for 20 seconds (a) before being placed in the CVD reactor and (b) after migration of the gold particles in the CVD reactor.*

Using ImageJ software, the micrographs in Fig. 13 were converted to binary images composed of only black and white pixels, as seen in Fig. 14. Then, pixel counting was used to determine how much of the surface was occupied by gold islands and how much of the underlying surface was exposed. For the sample that was sputtered but not placed in the reactor, the gold islands occupied 37.6% of the sample, while 62.4% of the underlying surface remained exposed. For the sample that was sputtered and then placed in the reactor, 37.9% of the sample contained islands, while 62.1% of the area was exposed aluminum. Although the gold migrated to form larger islands, the amount of exposed aluminum surface area remained essentially unchanged. So, using a sputtering time of 20 seconds results in a silica nanospring mat that occupies approximately 38% of the surface while 62% of the underlying surface remains capable of interacting with the surrounding environment. This is important because the thermal properties of aluminum are more conducive to heat transfer than the thermal properties of silica. As a result, the benefits of the exposed aluminum areas can remain efficient at promoting heat transfer.

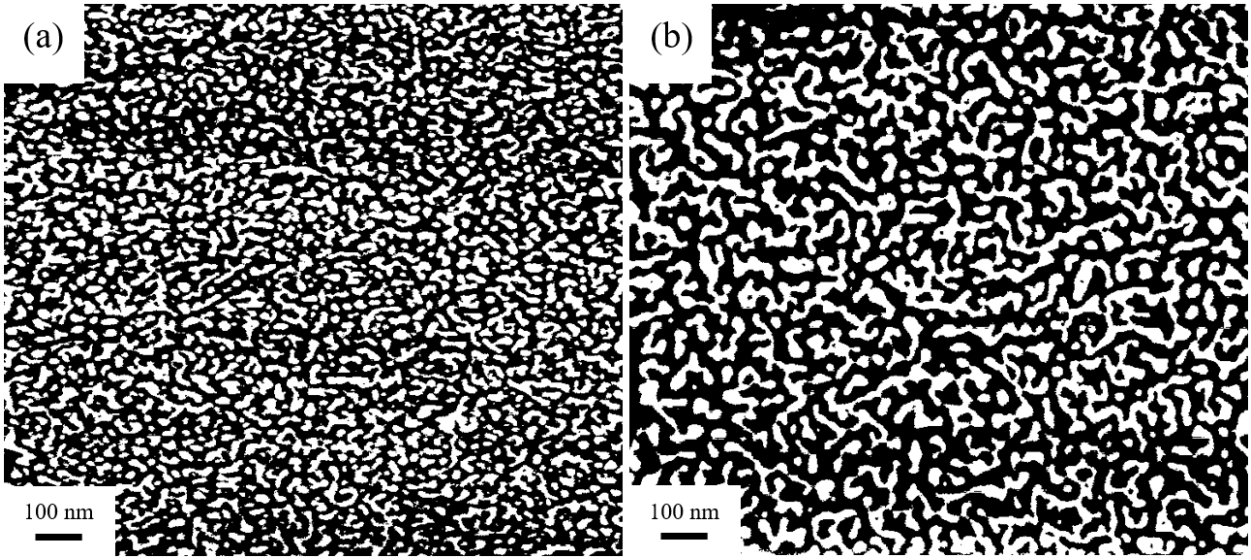

Figure 14. *Binary images showing (a) sputtered gold islands covering 37.6% of the surface with 62.4% of the underlying aluminum exposed and (b) migrated gold islands covering 37.9% of the surface with 62.1% of the underlying aluminum exposed.*

After establishing the sputtering time required for the nanospring growth, the temperature during the growth process was adjusted. Because the springs were being produced on a curved surface, more energy was required to get the springs to launch than on a planar surface. Because of this, the temperature at which the precursor was introduced to the reactor was increased from

310℃ to 325℃. This delayed the spring growth, allowing the gold to overcome the energy barrier and form the larger islands shown above. Because of this, enough gold was present to allow the springs to form. With the adjusted growth parameters, samples containing uniform nanospring mats along the length were created. As previously mentioned, the goal of the first part of this study was to evaluate the condensation heat transfer performance of silica nanospring mats with varying thicknesses and determine which mat thickness exhibited the best performance. Five samples with growth times varying from 5 minutes to 30 minutes were fabricated. Fig. 15 shows an SN5 sample prior to testing and is representative of all of the nanospring-coated condensation test samples prior to testing. It is worth noting that during the gold sputtering process, the distribution that the gold particles followed was conical in shape. As a result, the gold density is highest in the center of the sample and lowest towards the edges of the test section. This results in a slightly thicker nanospring mat in the center of the sample and a thinner nanospring mat towards the edges. SEM imaging, however, confirmed that the nanospring coating was still produced along the entire length of the test section.

Figure 15. *SN5 sample prior to testing.*

In order to ensure that the nanospring mat grew properly, SEM images were collected. Fig. 16 below shows a representative SEM micrograph of the SN5 sample prior to testing. In this figure, silica nanosprings can be seen with gaps between that eventually lead to the exposed underlying surface. The lighter particles in this image are the gold particles at the tips of different nanosprings. A variety of different spring structures are present, but each of the structures is made from multiple nanowires intertwining with one another. This is a representative image of the samples used in this study showing that the nanospring mat was successfully grown. For comparison, Fig. 17 shows a micrograph at the same magnification (75,000x) of a sample that was placed in the reactor for the same growth duration. However, in this sample the conditions had not yet been optimized, so the springs did not launch from the surface.

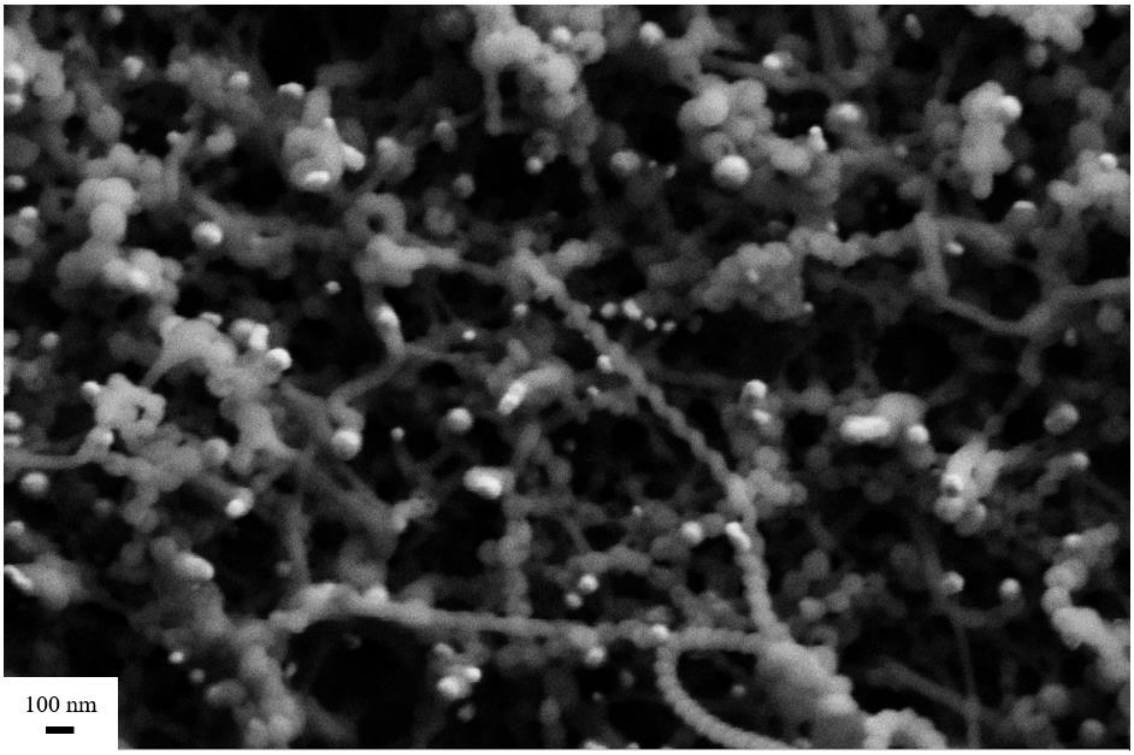

Figure 16. *SEM image of the SN5 sample prior to testing.*

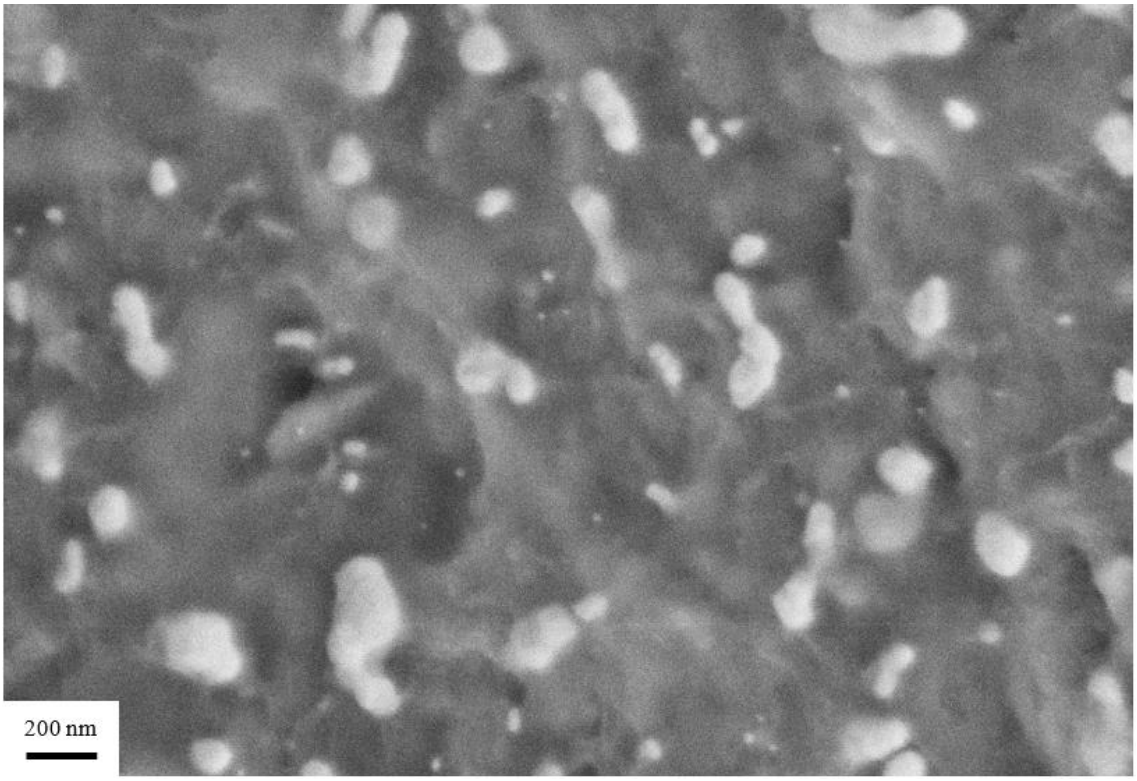

Figure 17. *SEM image of a sample in which the springs did not successfully launch.*

Images of all of the untested samples were collected in the SEM as shown in Figs. 18 and 19 below. SEM images of an uncoated baseline sample are also presented for comparison. From these images, it can be seen that the silica nanospring coating is present across the area of the sample. It can also be seen that as the growth time increases, longer springs have appeared within the mat as expected. Additional SEM images of the samples can be found in Section 10.4 of the Appendix.

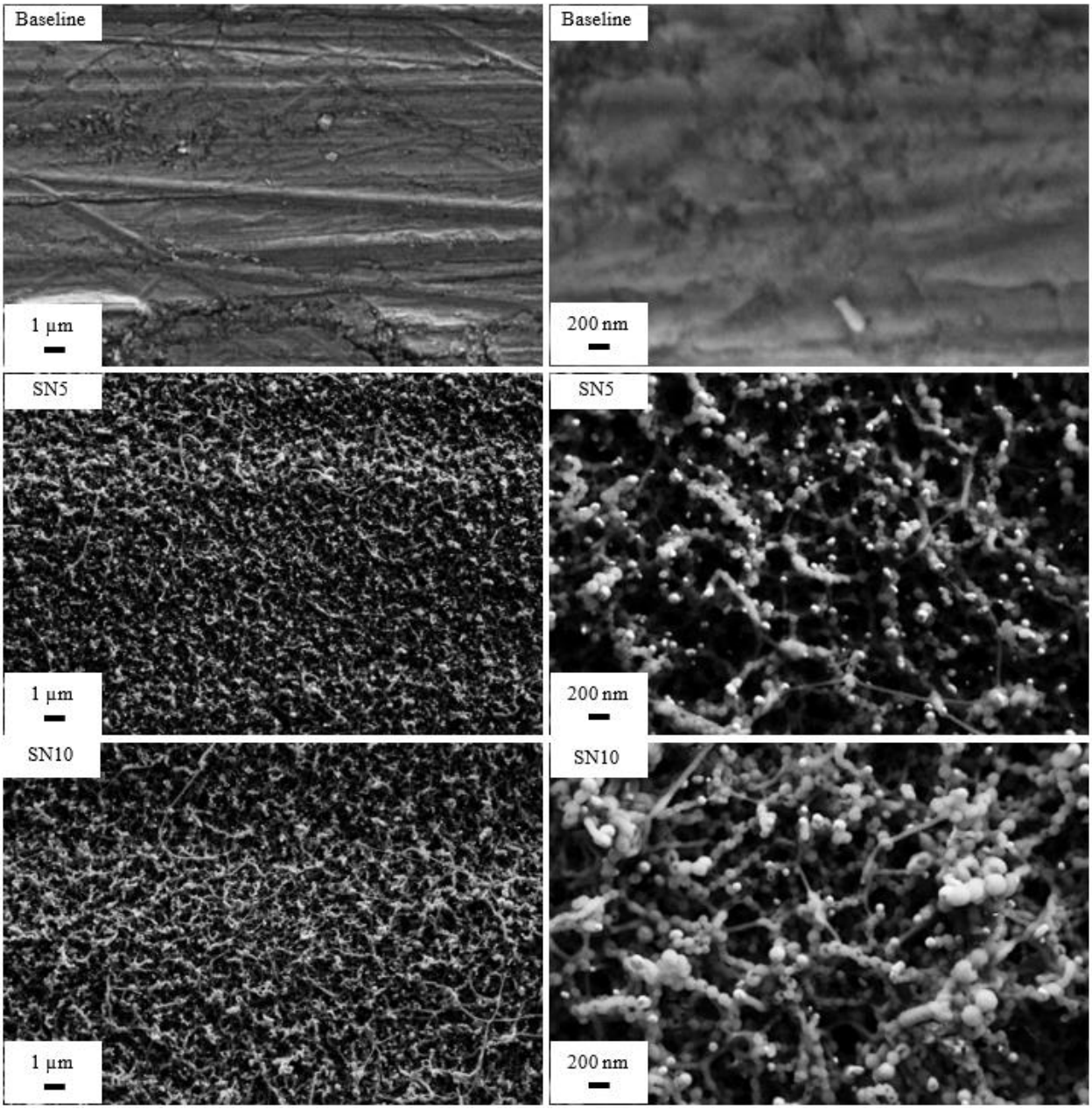

Figure 18. *SEM images of the untested baseline, SN5, and SN10 surfaces at 10,000x and 50,000x.*

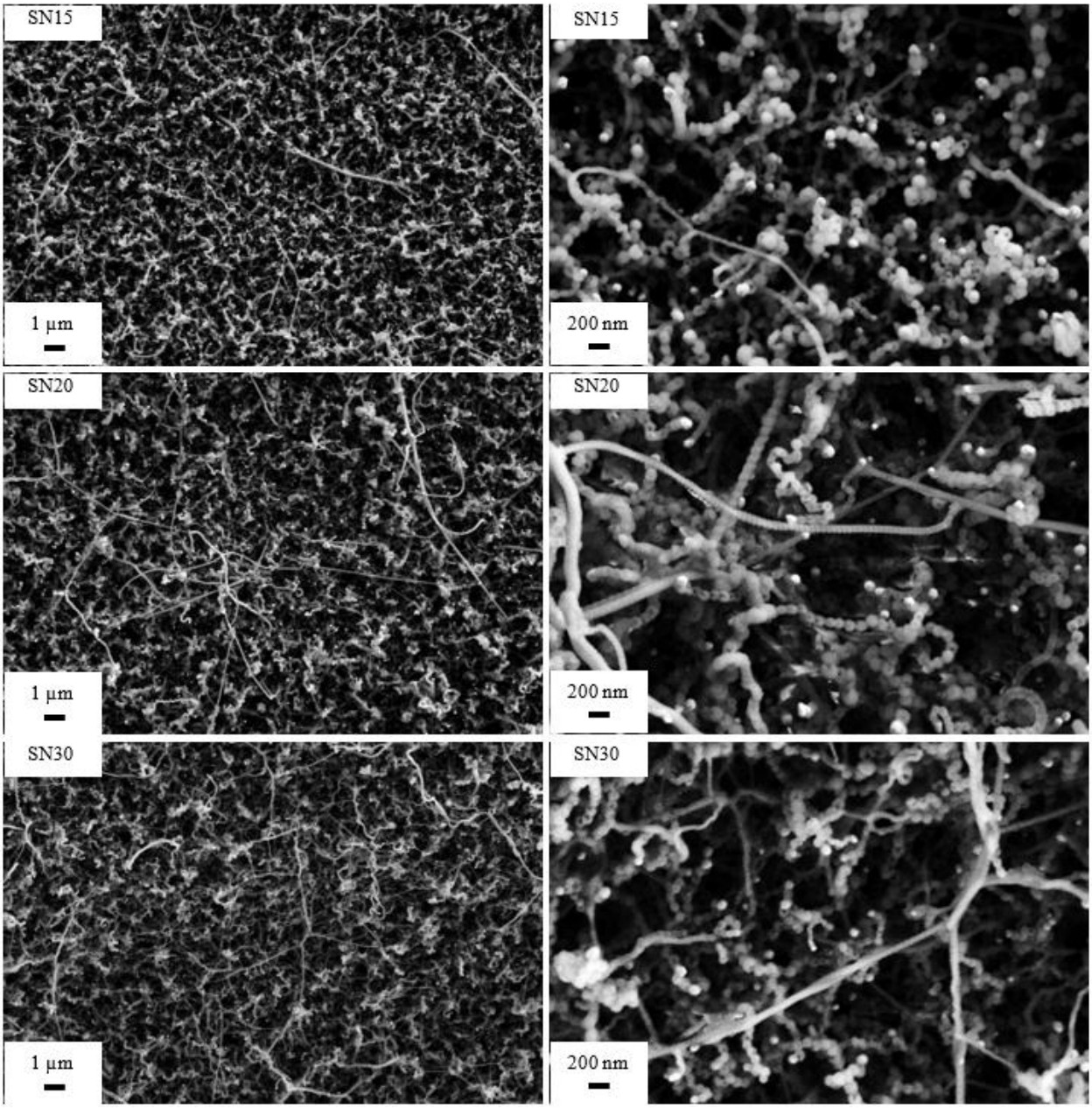

Figure 19. *SEM images of the untested SN15, SN20 and SN30 at 10,000x and 50,000x.*

Further characterization of the silica nanospring samples was completed through the use of X-ray energy dispersive spectroscopy (XEDS) within the Zeiss Supra 35 microscope. XEDS spectra were collected for each of the samples evaluated in this study prior to testing including the baseline sample. Figure 20 shows the spectrum collected for the baseline sample, while Fig. 21 shows the spectrum collected for the SN5 sample, which is representative of the untested spectra for the other nanospring-coated samples as well. These spectra were collected using an

accelerating voltage of 15 keV and were collected over a span of 300 live seconds. From the baseline sample, the most prominent elements were aluminum (Al), magnesium (Mg), and silicon (Si). The base material for each tube was aluminum, while magnesium and silicon were the highest concentration alloying elements within Aluminum 6061. From the SN5 spectra, these three elements were still prominent in the silica nanospring-coated samples, along with the addition of gold (Au) and an increased concentration of oxygen (O). The gold was present as a result of the sputtering process required for nanospring growth, while the concentration of the silica and oxygen increased. This is due to the formation of the silica (SiO_2) nanosprings. This again points to the fact that the silica nanosprings were successfully grown on the aluminum tube surfaces, but the aluminum substrate was still dominant in the material make-up of each sample.

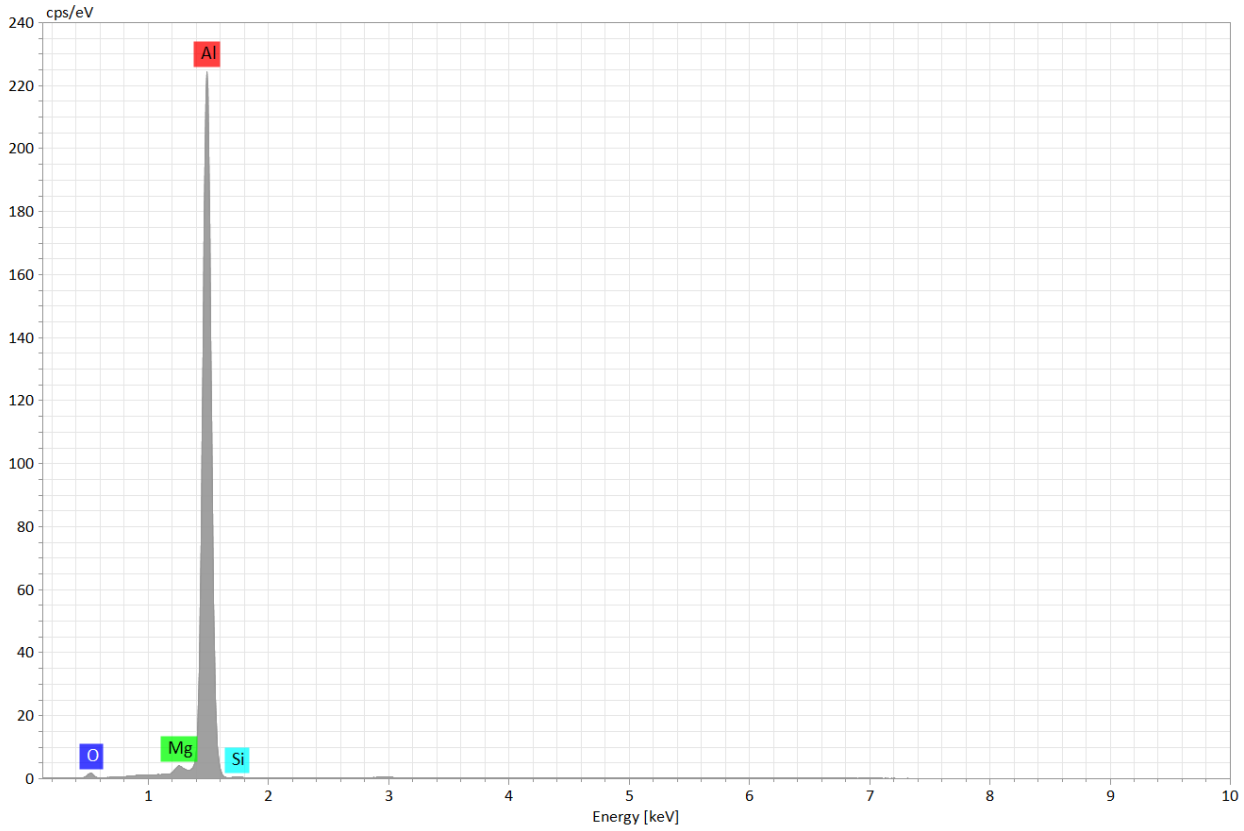

Figure 20. *XEDS spectrum collected from the untested baseline aluminum 6061 sample.*

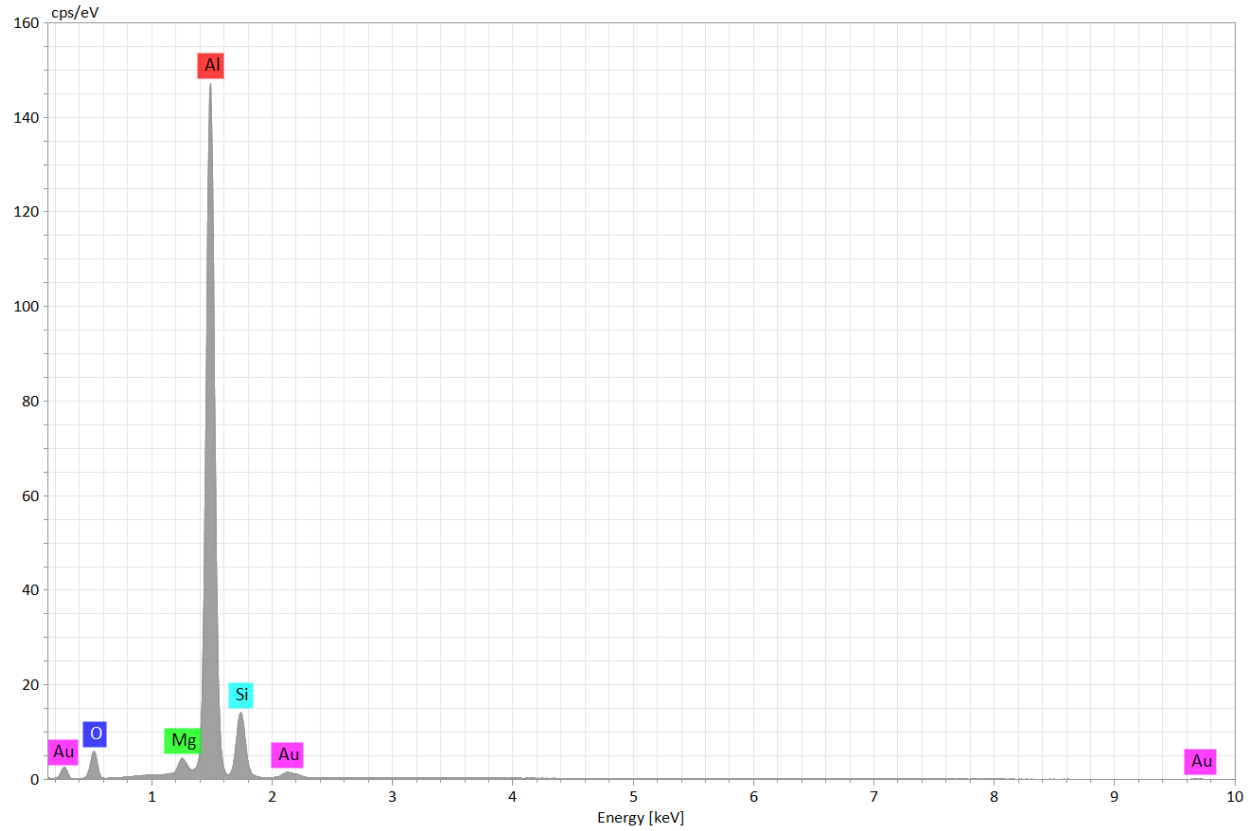

Figure 21. *XEDS spectrum collected from the untested SN5 sample, representative of the untested spectra from all of the silica nanospring-coated samples.*

In order to assess the additional thermal resistance of the presence of the silica nanospring mat, the mat thickness was measured using the SEM. Portions of the aluminum foil samples fabricated for contact angle measurements were used for these images. Regions where a side view of the mat thickness were captured, and the thickness was measured using the annotation features within Smart SEM interface as shown in Fig. 22. As a reminder, an increase in the exposure time to the precursor resulted in an increased mat thickness. The average mat thickness measurements for each of the samples can be found in Table 3. Silica is commonly thought of as a thermal insulator. Because of this, it is important to determine how much thermal resistance is posed by the addition of the silica nanospring coating. Thickness measurements were conducted to assess the additional thermal resistance that may be posed from the presence of the nanosprings. If the nanospring mat is assumed to be a uniform coating of silica across the sample surface, then Eq. (16) can be used to calculate the additional thermal resistance:

$$R_{SN} = \frac{\ln(D_o/D_i)}{2\pi Lk}, \tag{16}$$

where D_o and D_i are the outer and inner layer diameters respectively, L is the length of the coated region, and k is the thermal conductivity of amorphous silica, 1.8 $Wm^{-1}K^{-1}$ [44]. This approach over-approximates the thermal resistance of the mat due to the gaps between the nanosprings being ignored in these calculations. However, these gaps are important in the heat transfer process because they allow the underlying aluminum substrate, with better thermal properties, to directly interact with the surroundings. The calculated thermal resistance can also be found in Table 3. These values can be compared to the thermal resistance posed by the tube wall, which was found to be 1.19E-03 KW^{-1} using Eq. (12). Based on these results, it can be seen that the thermal resistance due to the mat is much lower than the aluminum tube walls, however as the mat becomes thicker this resistance increases. It is also important to remember that this method assumes that a silica mat covers the entire surface, over-approximating the true thermal resistance and that the conduction thermal resistance associated with the aluminum tube wall is, itself, often small when compared to the convective resistance terms.

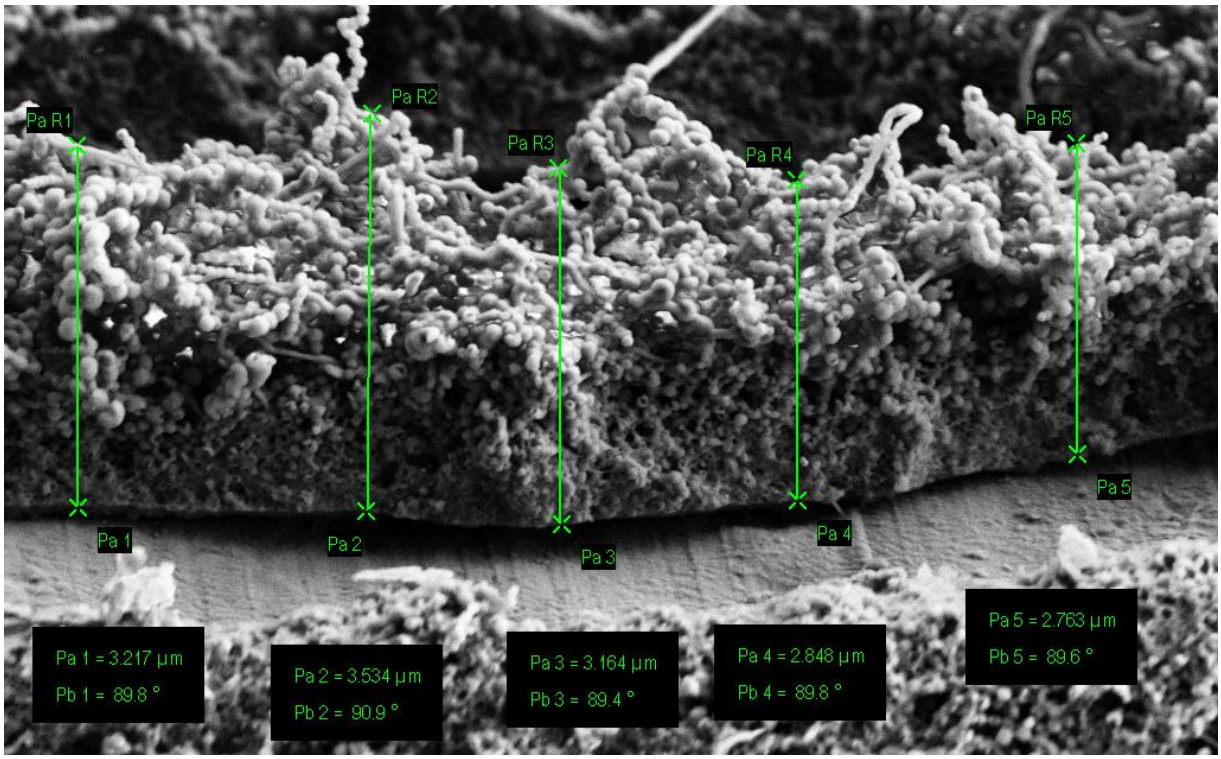

Figure 22. *An annotated SEM micrograph of the SN30 sample used to measure the thickness of the nanospring mat.*

Table 3. *Silica nanospring mat thicknesses and the associated overapproximated thermal resistance.*

Surface ID	Mat Thickness (nm)	Thermal Resistance (KW^{-1})	Percent of Wall Thermal Resistance	Nanospring Mass ($g\ cm^{-2}$)
SN5	784.2 ± 137.4	7.09E-05	6.0%	3.32E-02
SN10	948.8 ± 209.2	8.57E-05	7.2%	8.72E-02
SN15	1081 ± 335.6	9.77E-05	8.2%	9.24E-02
SN20	1825 ± 354.6	1.65E-04	13.9%	1.15E-01
SN30	2902 ± 538.2	2.62E-04	22.1%	1.54E-01

Much consideration and iteration had to be taken into account in order to adjust the growth parameters in order to achieve silica nanospring growth on the curved aluminum tube surface. These adjustments were made in order to overcome the energy barrier associated with curved surfaces, as well as to increase the space between nanosprings and allowing more access to the underlying aluminum surface. The sputtering time was set to 20 seconds on the rotating tube samples. The reactor chamber temperature was increased, and the precursor exposure time was delayed in order to increase the energy available to produce the coating. SEM imaging and other techniques were used to prove the nanospring mat was fabricated as expected and to better characterize the coating in general. Thickness measurements were collected and averaged to show that an increase in the precursor exposure time also increased the mat thickness. The thermal resistance of each coating was calculated with an over-approximation, which showed that the thermal resistance due to the tube wall is significantly higher than the resistance posed by the coating.

5.2 Wettability Assessment

Contact angle measurements were collected using a Ramé-Hart contact angle goniometer in order to assess the wettability of each surface. These measurements provide insight into the surface energy of each sample, where surfaces with higher surface energy are hydrophilic, and surfaces with low surface energy are hydrophobic. Static (θ_{static}), advancing (θ_{adv}), and receding (θ_{rec}) contact angle measurements were collected using the sessile droplet method. As a reminder, a high static contact angle measurement and a low contact angle hysteresis (see Eq. (15)) value are indicative of a higher degree of hydrophobicity. For each sample, 20 static contact angle measurements were recorded, while 10 advancing and 10 receding contact angle measurements

were recorded. A summary of these measurements and their associated uncertainties can be found in Table 4. From these measurements, it is clear that the static contact angles were significantly higher for the nanospring-coated samples when compared to the baseline aluminum sample, indicating that the nanosprings have attained the desired hydrophobic affect. The SN5 sample had the lowest average static contact angle measurement at 133.0º, however, this was still nearly 50º higher than the baseline sample with a static contact angle measurement of 83.7º. This result is further represented by the images of static droplets for each of the samples, shown in Fig. 23. With the presence of the nanospring coating, the droplets are more repelled from the surface causing the droplets to form into more of a sphere shape, as opposed to the nearly hemispherical droplet present on the baseline surface. The hysteresis calculations also support the hydrophobicity of the silica nanospring coating with every nanospring sample other than SN10 having a lower hysteresis value than the baseline sample.

When evaluating just the silica nanospring samples, a trend can be seen between the mat thickness and the contact angle measurements. As the mat thickness increases, the static contact angle measurement also increases to a certain point and then plateaus (see Fig. 24). A similar trend was present with the contact angle hysteresis where the hysteresis values decreased as the growth time increased beyond 10 minutes. However, only a marginal improvement was recorded between the SN20 and SN30 sample. This suggests that after a certain thickness the droplet is only interacting with a portion of the mat and only minimal or no gains can be achieved by increasing the mat thickness. For this application, this may suggest that an optimal mat thickness may exist that balances the benefits of increased hydrophobicity and the drawbacks of increased thermal resistance posed by thicker nanospring mats.

Table 4. *Contact angle measurements for each test sample.*

Surface ID	$\boldsymbol{\theta_{static}}$	$\boldsymbol{\theta_{adv}}$	$\boldsymbol{\theta_{rec}}$	$\boldsymbol{CAH}$
Baseline	83.7º ± 8.2º	98.3º ± 5.4º	58.3º ± 10.3º	40.0º
SN5	133.0º ± 7.9º	140.0º ± 6.1º	117.2º ± 7.8º	22.8º
SN10	148.4º ± 7.4º	166.7º ± 7.1º	123.5º ± 4.9º	43.2º
SN15	151.1º ± 8.6º	160.8º ± 4.5º	131.7º ± 4.8º	29.1º
SN20	152.3º ± 8.2º	160.4º ± 6.0º	141.0º ± 5.6º	19.4º
SN30	155.3º ± 8.1º	160.6º ± 5.7º	144.4º ± 3.8º	16.2º

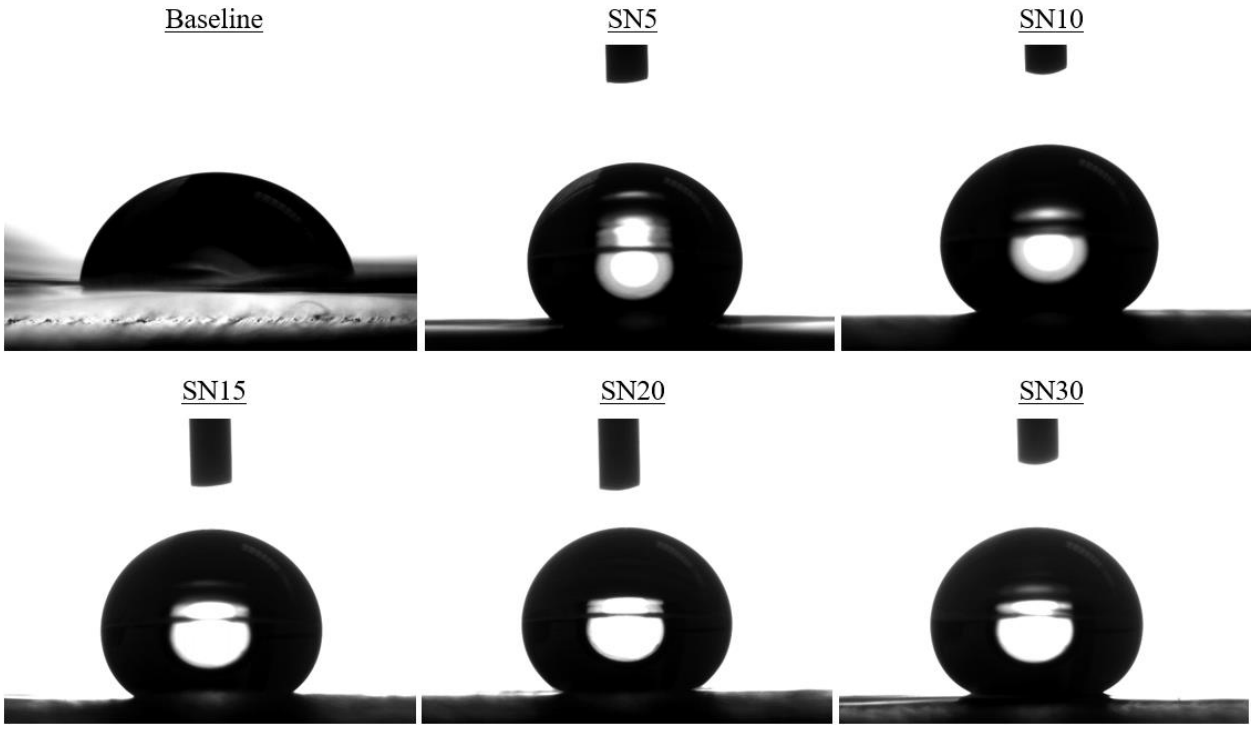

Figure 23. *Static droplet images for the baseline and nanospring-coated samples.*

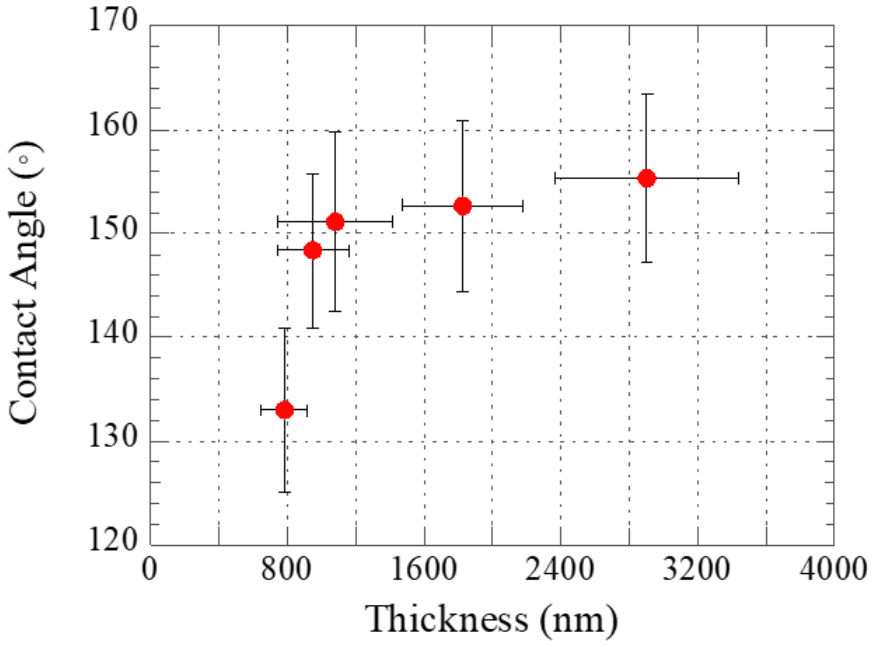

Figure 24. *Relation between static contact angle measurement and silica nanospring mat thickness.*

5.3 Baseline Condensation Testing

Condensation heat transfer testing was conducted on an uncoated aluminum 6061-T6 tube as a baseline for comparison throughout this study. The baseline tube was prepared in the same way as the nanospring-coated samples prior to the gold sputtering process. Tests were conducted at flowrates ranging from 1.5 to 5.5 LPM in 0.5 LPM increments and nominal subcooling temperatures of 1.5℃, 5.5℃ and 9.5℃. Throughout this condensation testing, the baseline surface promoted filmwise condensation, as seen in Fig. 25. This was expected given the hydrophilic nature of aluminum as well as the hydrophilic classification shown with the contact angle measurements.

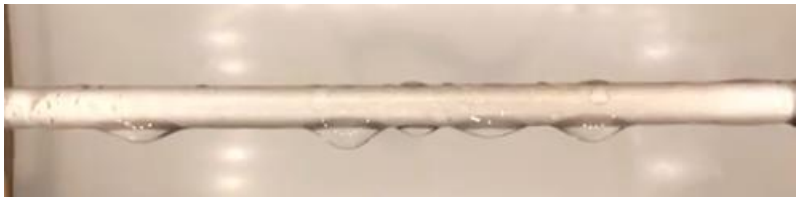

Figure 25. *Condensation on the baseline aluminum sample behaving in a filmwise manner.*

In this study, the condensation heat transfer coefficient was calculated for the experimental data using the constant surface temperature approach (Method 1). Within the set of baseline tests, the maximum difference in the surface temperature between the inlet and outlet of the sample was less than 1℃, so this method was applicable. A plot of the condensation heat transfer coefficient with respect to the degree of subcooling between the tube surroundings and the temperature of the cooling fluid at the sample inlet can be found in Fig. 26. In this plot, the dependence of the condensation heat transfer coefficient on the degree of subcooling, similar to the plots shown in Fig. 3 from [27]. A large degree of uncertainty is present at the lowest degree of subcooling due to a combination of a small measured temperature change within the cooling fluid and the accuracy limitations of the thermocouples. The cooling fluid temperature change throughout this data set ranged from 0.09℃ to 0.34℃. As a result, a high uncertainty was present in the lower degree of subcooling calculations.

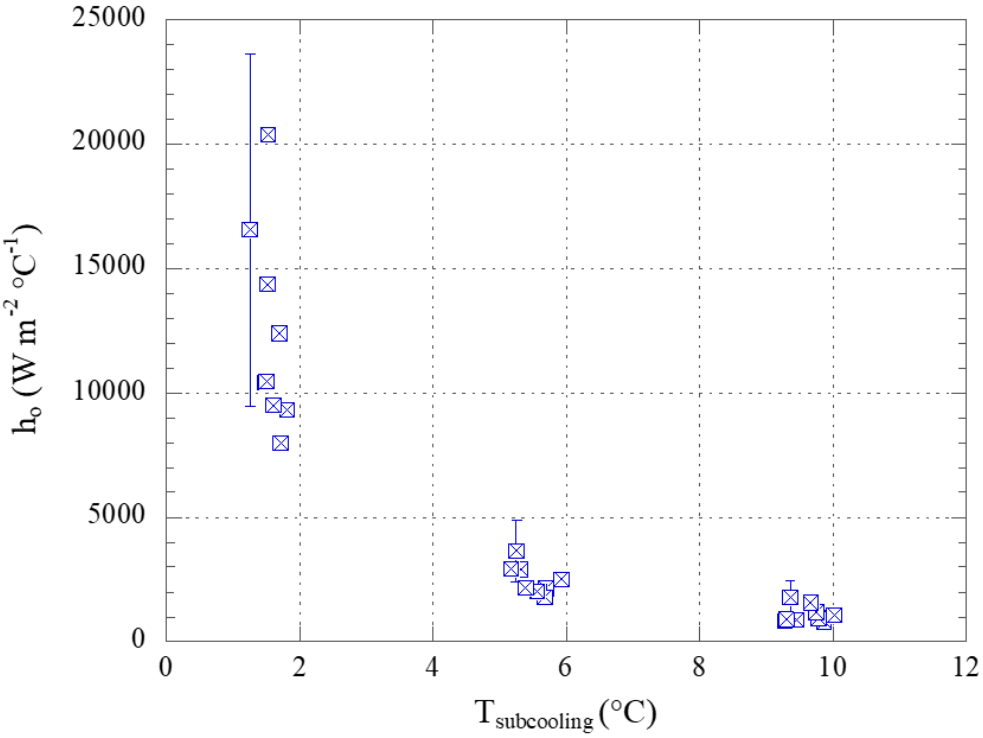

Figure 26. *A plot of the baseline aluminum condensation heat transfer coefficient with respect to subcooling, calculated using the constant surface temperature approach.*

After conducting the condensation heat transfer testing, it was realized that the temperature differences within the test setup were on the order of less than 1°C. This resulted in large uncertainties and limited the ability to differentiate the heat transfer performance of each of the samples. As a result, additional methods for making comparisons were identified. In order to further assess the heat transfer capabilities of each sample, the amount of heat transferred to the cooling fluid (q) was calculated for each test using:

$$q = \dot{m} c_p \left(T_{m,out} - T_{m,in}\right), \tag{17}$$

where $\dot{m}$ is the mass flowrate of the cooling fluid, c_p is the specific heat of the cooling fluid (in this case water), and $T_{m,out}$ and $T_{m,in}$ and the temperature of the cooling fluid at the outlet and inlet of the sample respectively. The plots in Fig. 27 present the cooling fluid heat transfer rate for the baseline tube at each of the nominal degrees of subcooling tested. From these plots, it is clear that the amount of heat transferred increases as the Reynolds number increases. These plots, as

well as the plot of the condensation heat transfer coefficient, Fig. 26, will serve as a point of comparison with the silica nanospring-coated samples.

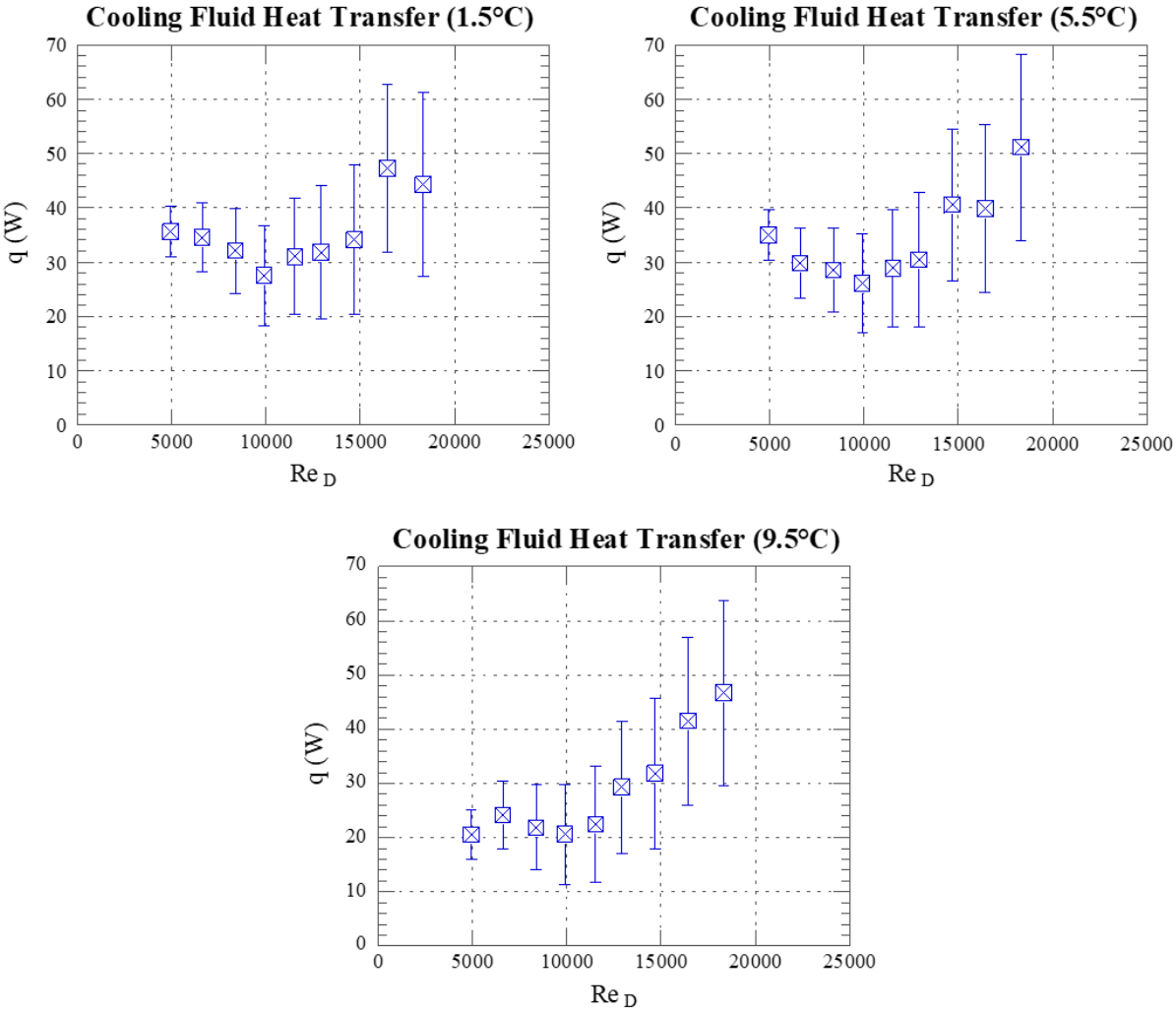

Figure 27. *Quantification of heat transferred to the cooling fluid during the baseline condensation heat transfer experimentation as a function of degrees of subcooling.*

5.4 Uniformly Coated Condensation Heat Transfer Testing Results

After conducting the baseline testing, the samples uniformly coated in nanosprings were evaluated. With this testing, the goal was to identify first, whether the nanospring coating promoted dropwise condensation and, second, if it improved the heat transfer performance over the baseline sample. Images of the condensation formation on each of the samples can be found in Fig. 28. From this image, it is clear that the water condensation behavior on the silica nanospring samples

is significantly different than on the baseline sample. The nanospring samples promoted dropwise condensation (DWC) formation, and the droplets were also smaller in size on average than on the baseline surface. As a result, more of the underlying surface was exposed to the surroundings in between the droplets and the droplet departure frequency increased.

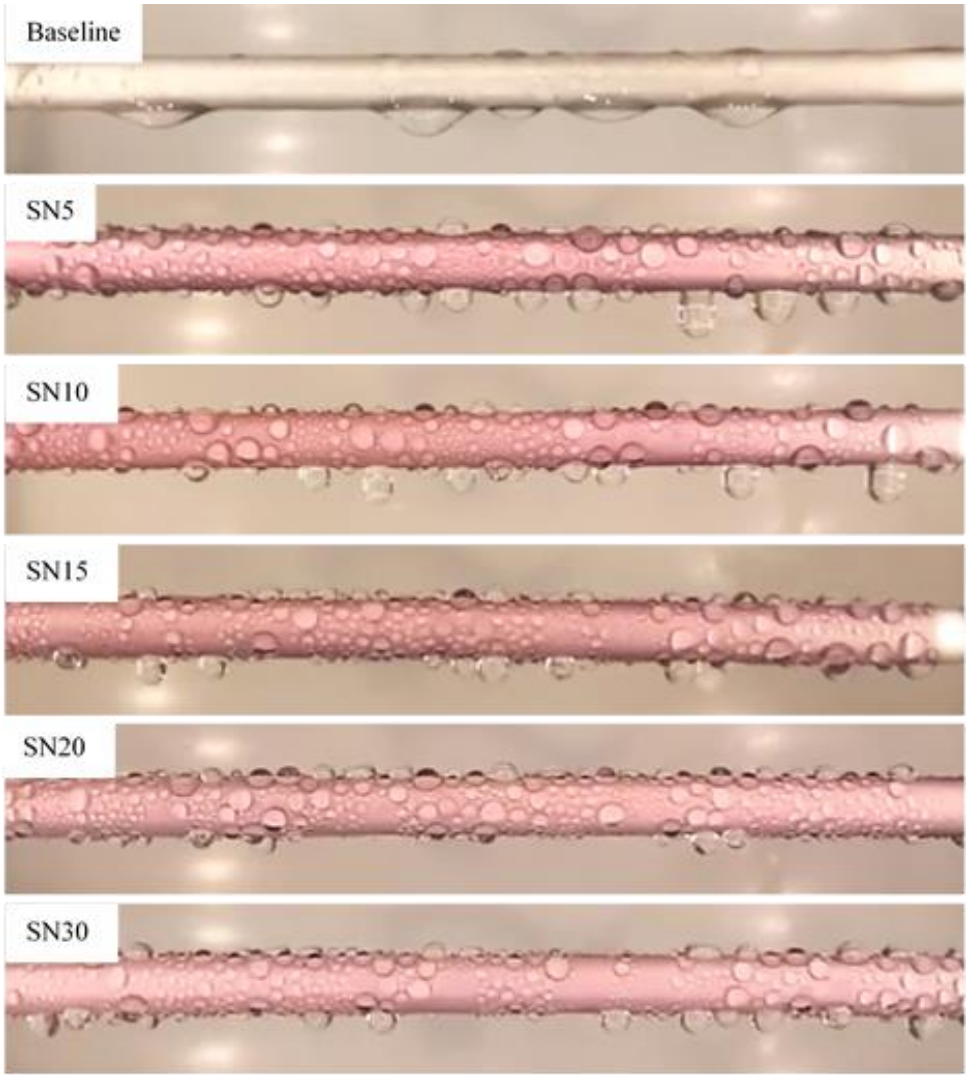

Figure 28. *Images of the condensation formation of the various samples taken during condensation heat transfer testing.*

As with the baseline sample, the condensation heat transfer coefficient was calculated for each of the nanospring-coated samples using the constant surface temperature methodology (Method 1). A comparison plot of the calculated heat transfer coefficients can be found in Fig. 29. This plot was generated by averaging the various condensation heat transfer coefficient values for

each sample at each of the nominal subcooling temperatures. The error bars represent a 95% confidence interval based on twice the standard deviation. As previously mentioned, the small temperature difference experienced within the test setup resulted in a relatively large amount of uncertainty. Because of this, none of the average heat transfer coefficients are significantly different; however, some trends can still be noted. Within this plot, the heat transfer coefficients of the SN15 and SN20 samples are comparable to the baseline heat transfer coefficient at each of the tested degrees of subcooling. It can also be noticed (especially at the 1.5°C of subcooling) that the condensation heat transfer coefficient increases as the mat thickness increases from SN5 up to SN20, but then drops with the SN30 sample. It is hypothesized that this is indicative of the additional thermal resistance of the thicker coating outweighing the benefits of increased hydrophobicity. This explanation is supported based on the SN30 sample having a similar wettability to the SN15 and SN20 samples while having a mat that is nearly twice as thick as the SN20 sample. As a result, the SN30 had poor heat transfer performance. The SN5 sample also had poor heat transfer performance, which may be explained by the higher degree of wettability (i.e. more hydrophilic) as compared to the thicker nanospring coatings.

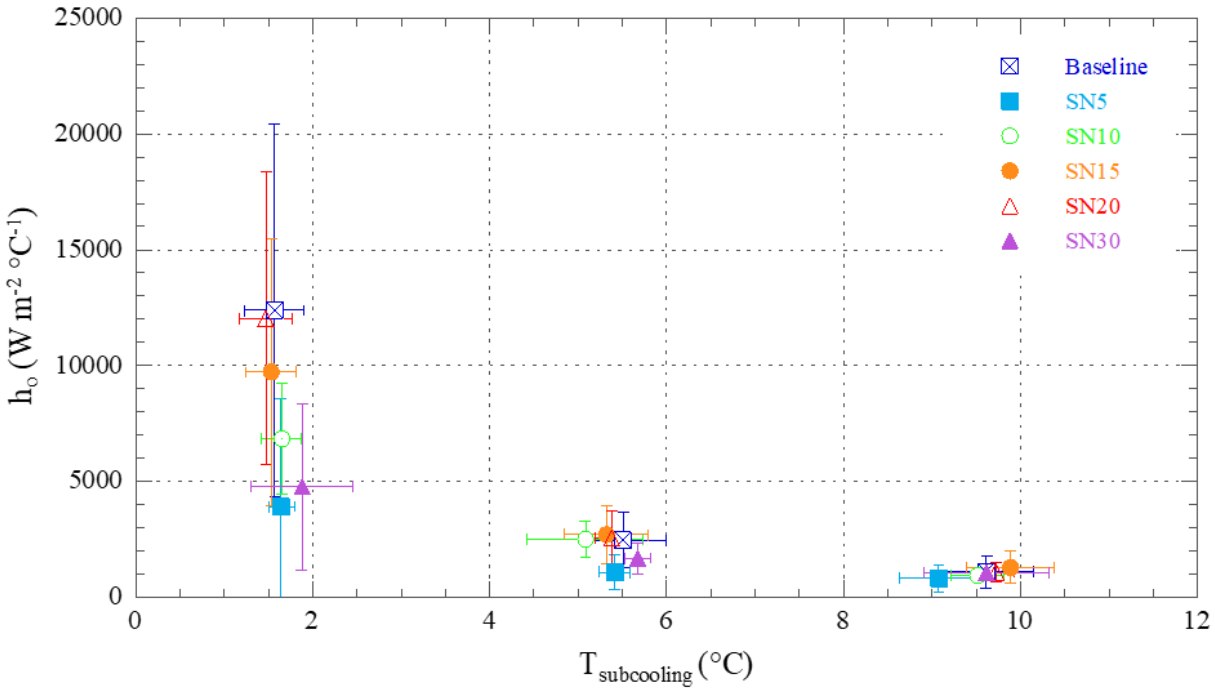

Figure 29. *Comparison plot of the condensation heat transfer coefficient for the uniformly coated silica nanospring samples.*

Because no statistically significant differences could be shown through the condensation heat transfer coefficients, the heat transfer rate experienced by the cooling fluid was calculated for each of the condensation tests. Comparison plots with the baseline calculations can be found in Figs. 30, 31, and 32 for 1.5℃, 5.5℃, and 9.5℃ degrees of subcooling, respectively. Representative error bars are presented on a set number of data points within each plot. For completeness, plots containing error bars at each of the data points are provided in Section 10.5 of the Appendix. Similar to the heat transfer coefficient calculations, the SN15 and SN20 samples have comparable performance to the baseline sample and even outperform it in some instances. For example, in the low Reynolds number region of the plot for 9.5℃ of subcooling (i.e. Fig. 32), the baseline sample is one of the worst performers, while the SN15 data point is significantly higher than the baseline data point. The SN15 sample had a heat transfer value approximately 60% higher than the baseline value at the lowest Reynolds number ($Re \approx 5000$) and 9.5℃ of subcooling. Moreover, throughout the 5.5℃ and 9.5℃ degrees of subcooling plots (i.e. Figs. 30 and 31 respectively), the heat transferred to the cooling fluid with the SN15 coating outperformed the baseline sample. It is speculated that with the higher degrees of subcooling, more condensation is formed on the tube surface due to the greater energy difference between the cooling fluid and the surrounding environment. The heat transfer performance of the SN15 and SN20 samples is likely explained by these coatings being more capable of shedding water from the surface due to their hydrophobic nature. Similar to before, the SN5 and SN30 samples again showed the worst performance when looking at the heat transferred to the cooling fluid.

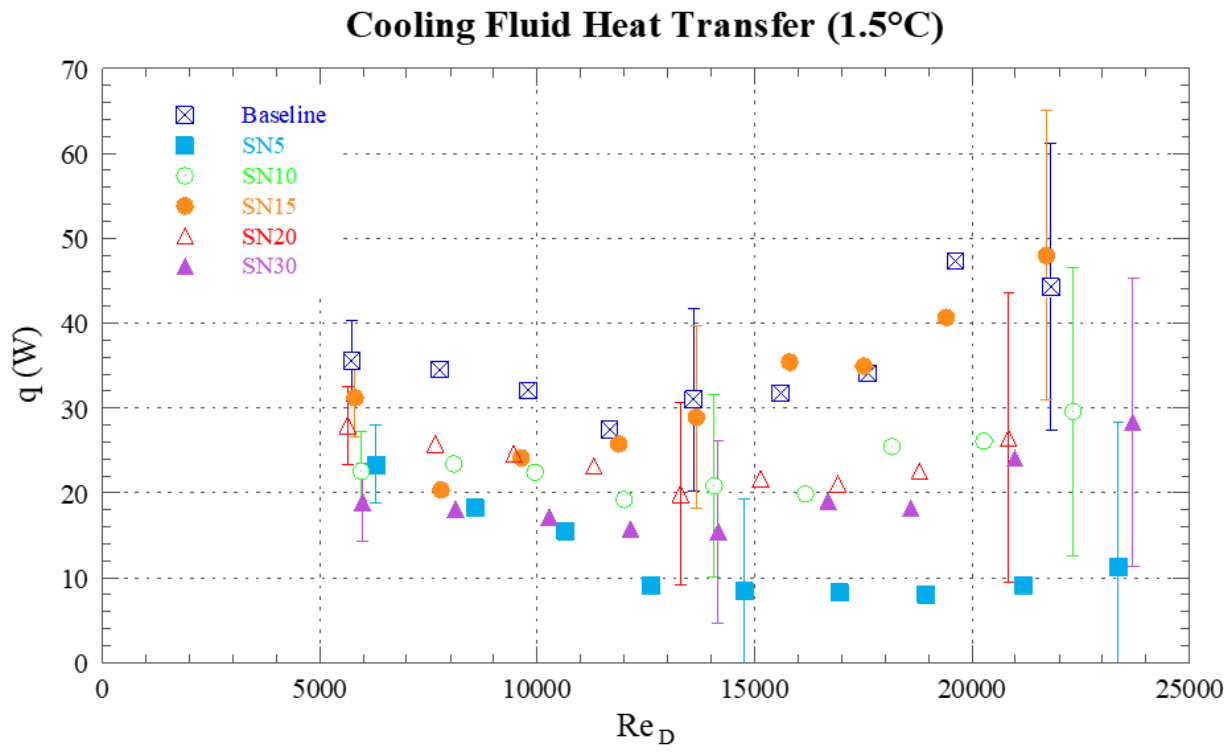

Figure 30. *Comparison of the heat transferred to the cooling fluid (q) between uniformly coated silica nanospring samples at 1.5°C of subcooling.*

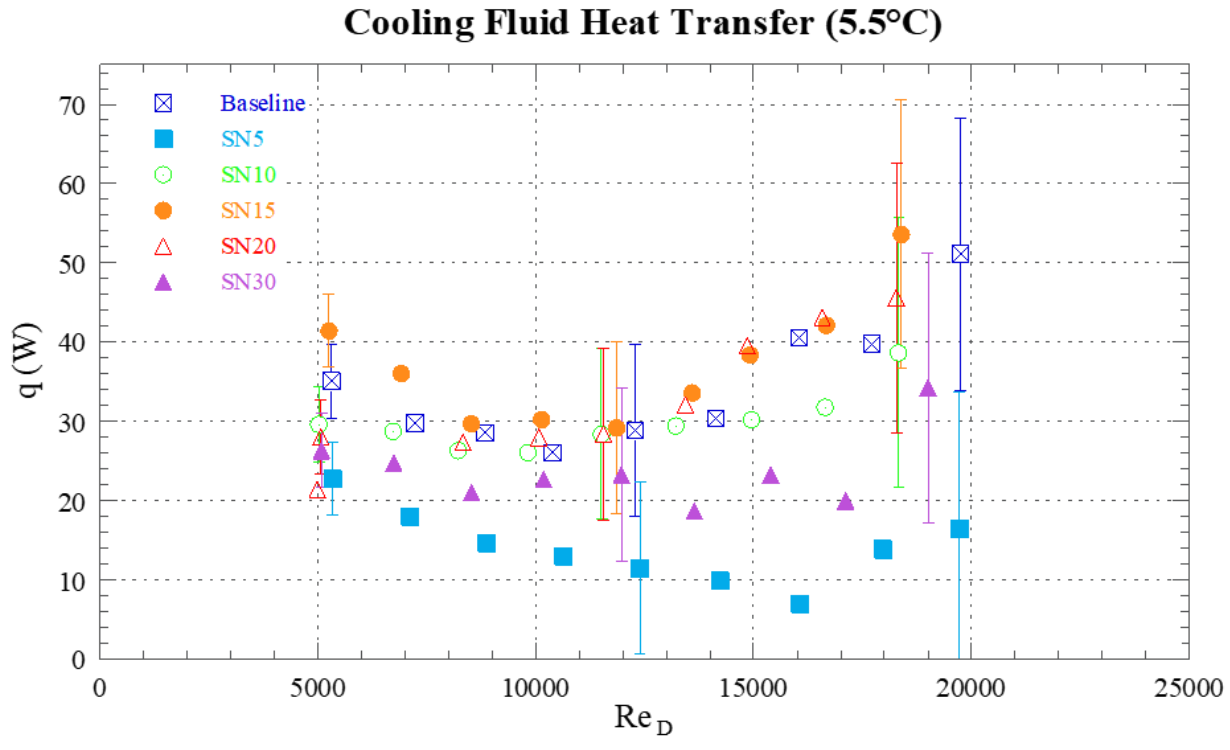

Figure 31. *Comparison of the heat transferred to the cooling fluid (q) between uniformly coated silica nanospring samples at 5.5°C of subcooling.*

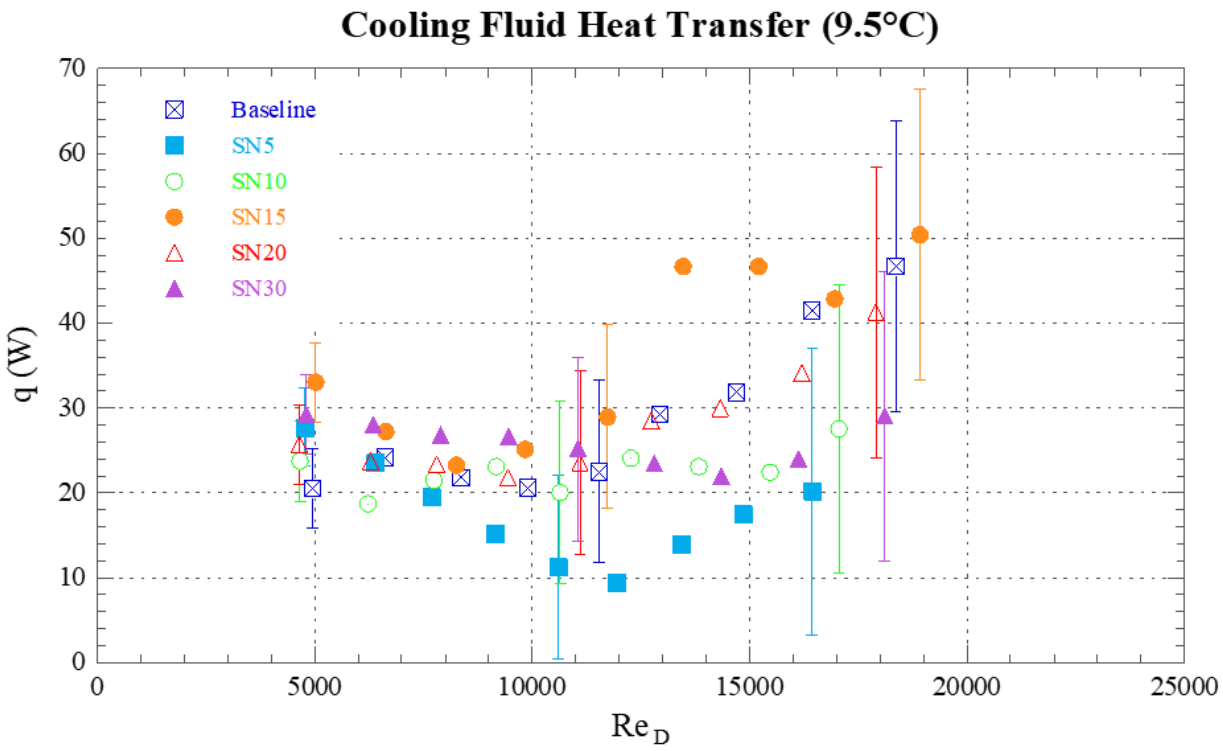

Figure 32. *Comparison of the heat transferred to the cooling fluid (q) between uniformly coated silica nanospring samples at 9.5°C of subcooling.*

5.5 Patterned Sample Condensation Heat Transfer Testing Results

Based on the results of the uniformly coated samples, a patterned sample was created using the nanospring growth conditions with the best heat transfer performance. A growth time of 15 minutes, sample SN15, was selected. The SN15 sample had comparable performance to the baseline sample in all cases and even outperformed the baseline at higher degrees of subcooling. The contact angle measurements of sample SN15 showed a similar wettability to the SN20 and SN30 samples but had a thinner mat which would pose less thermal resistance. Identical growth conditions to SN15 were thus used to create the patterned tube sample. The patterned nanospring sample design consisted of hydrophilic regions adjacent to hydrophobic regions in the form of rings down the length of the tube. Similar to the articles about hybrid wettability patterning in the literature review, the goal of this arrangement was to promote droplet movement from the hydrophobic regions to the hydrophilic regions. With this movement, it would also be more likely for neighboring droplets to interact and coalesce in the hydrophilic region, combining into a single droplet with sufficient mass for droplet drainage and departure. In other words, with an increased

mass, the larger droplets would be more likely to shed from the surface. Thus, less water would remain on the tube surface resulting in decreased thermal resistance and better heat transfer performance. This droplet movement and shedding process is represented in the Fig. 33 graphic.

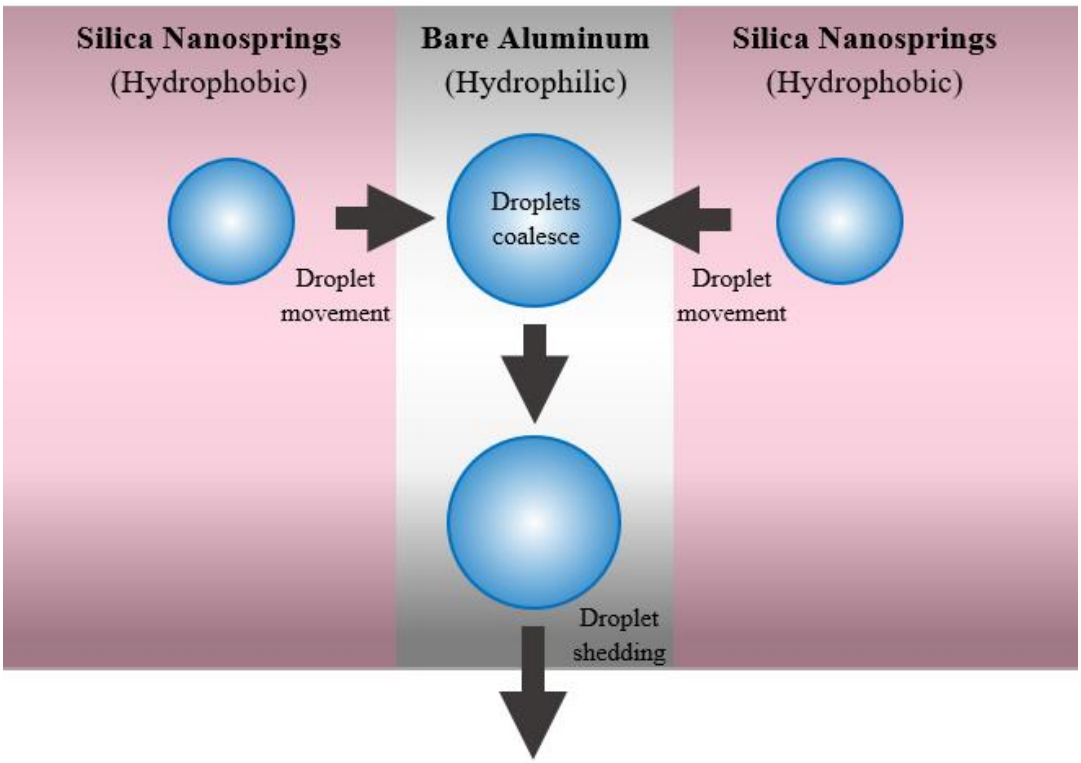

Figure 33. *Graphic of the droplet behavior on the patterned sample.*

The patterned tube sample was fabricated in the same manner as described earlier in the sample preparation portion of the methodology (see Section 4.5). Prior to the sample being sputtered with gold, a 1.25 mm wire was wrapped around the tube sample with an approximately even spacing between each ring. The sample was then sputtered with gold while rotating at 45 rpm. The presence of the wire on the tube masked parts of the tube so the gold could not be deposited. After the sputtering process, the wire was removed, and the sample was placed in the CVD reactor where the growth duration was set for 15 minutes. During this time, the silica nanospring coating grew in the regions that had been sputtered with gold, but the coating was not capable of growing in the regions that had been masked. As a result, the patterned tube had localized regions of hydrophobicity where the nanosprings were launched that were adjacent to localized regions of hydrophilicity that were naturally associated with bare aluminum. An image

of the resulting patterned tube can be found in Fig. 34. Using pixel counting in KAPPA ImageBase software, the ratio of the width of the hydrophobic region to the width of the hydrophilic region was found to be approximately 6:1. SEM images were captured within the coated and uncoated regions of the sample in order to prove the mat grew properly and only in the regions in which it was intended to grow (see Fig. 35).

Figure 34. *Picture of the patterned sample with hydrophobic silica nanospring regions (pink) adjacent to hydrophilic bare aluminum regions (gray).*

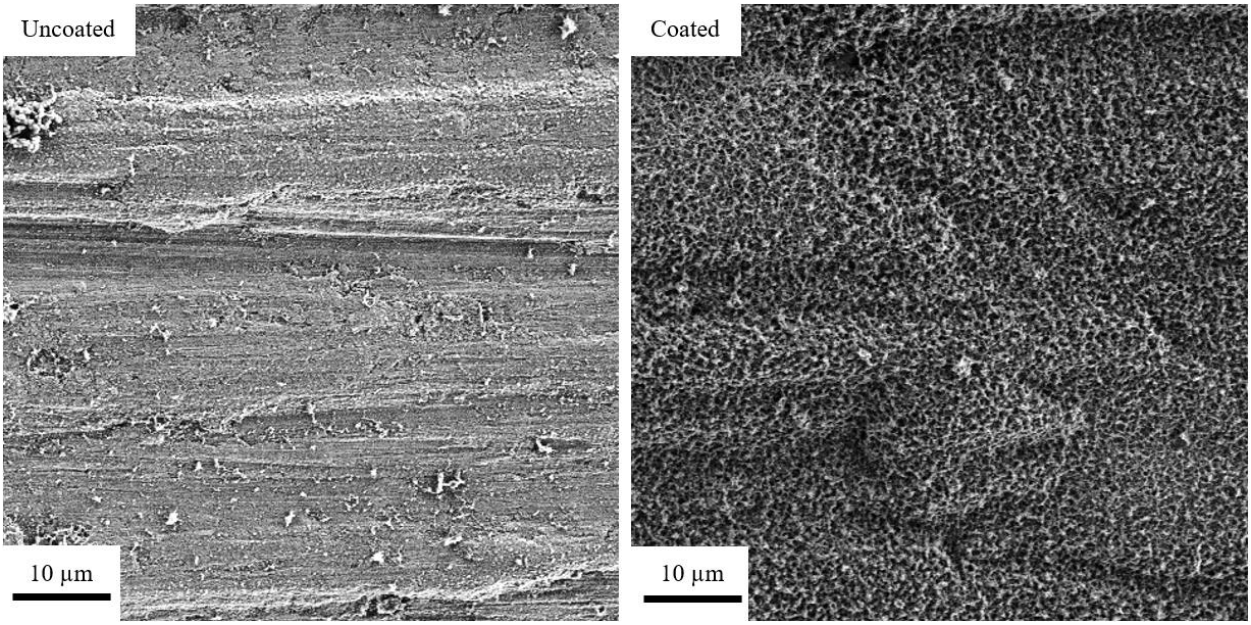

Figure 35. *SEM images of the patterned sample showing the nanosprings grew properly in the sputtered regions and did not grow in the masked regions.*

The patterned sample was placed through the same testing as the other samples in order to assess the heat transfer performance. Throughout this testing, it was noticed that the droplet behavior followed a noticeable pattern. As seen in Fig. 36, the droplets located at the bottom of the tube were aligned with the uncoated hydrophilic aluminum regions of the tube. This helps prove that the patterned tube was functioning as expected, and the droplets on the surface were being redirected from the hydrophobic regions to the hydrophilic regions. It is also worth noting

that the droplets within the uncoated regions appeared to be larger in diameter than the droplets in the coated regions, again promoting the idea that droplets were coalescing and collecting in the hydrophilic regions, thereby resulting in droplets with more mass.

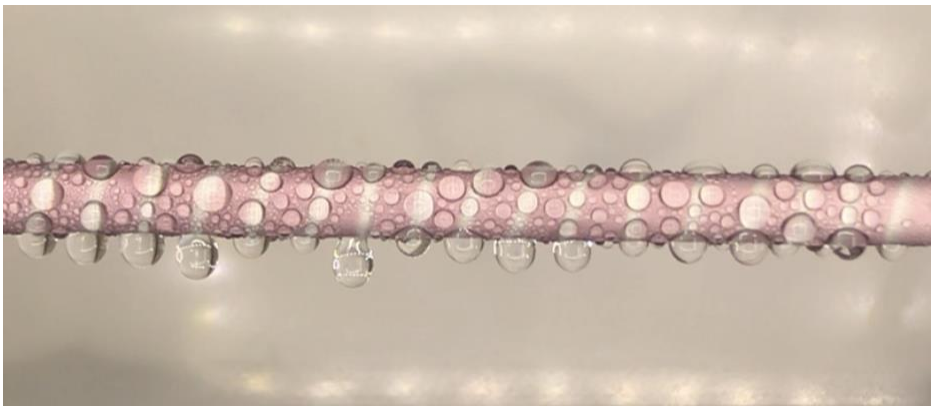

Figure 36. *Condensation behavior on the patterned sample with droplets aligning with the hydrophilic uncoated regions of the tube.*

A plot comparing the condensation heat transfer coefficient of the patterned tube to the baseline sample and the SN15 sample can be found in Fig. 37. As with before, a high degree of uncertainty results from the low degree of temperature change within the test setup. However, it can be seen that the patterned sample has comparable performance to the SN15 and baseline samples, especially at the higher degrees of subcooling. The heat transfer to the cooling fluid was also calculated for the tests conducted with the patterned sample using Eq. (17). Comparison plots for this heat transfer quantity are presented in Figs. 38, 39, and 40. The patterned surface again exhibited comparable performance to the baseline and SN15 samples and performed best at higher degrees of subcooling. This is again likely due to the fact that more condensation is formed at higher degrees of subcooling, and the patterned design may allow for more condensate to be removed from the surface.

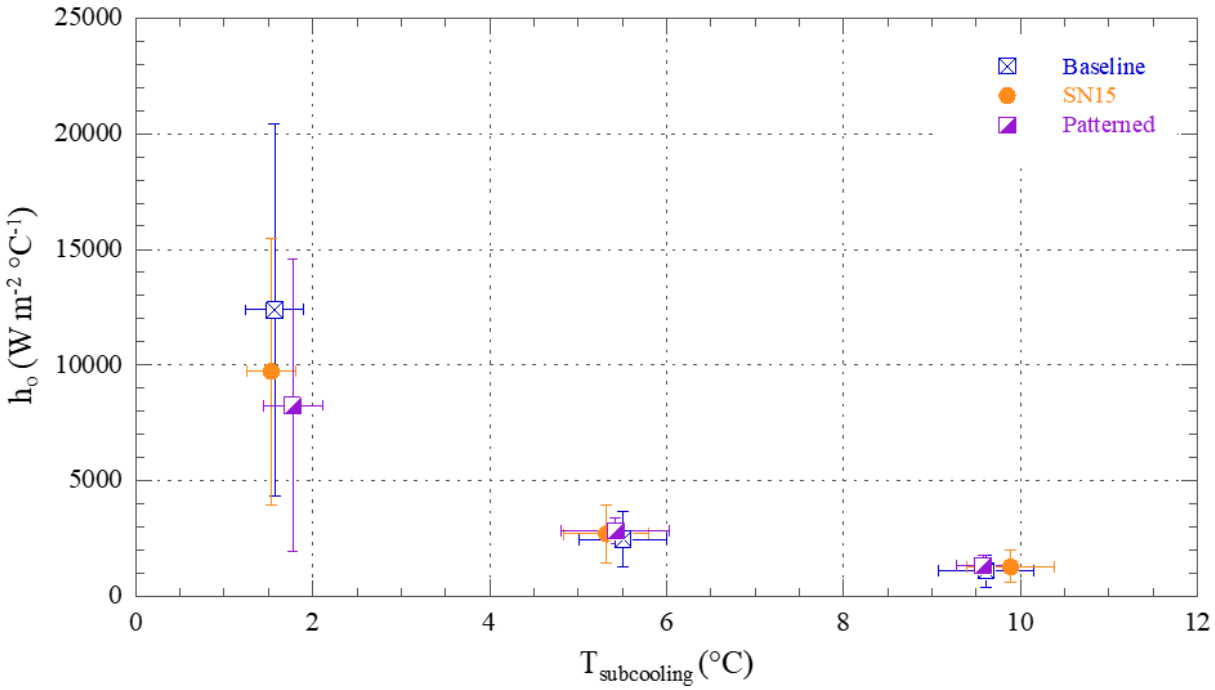

Figure 37. *Comparison plot of the condensation heat transfer coefficient for the patterned sample with the SN15 and baseline aluminum samples.*

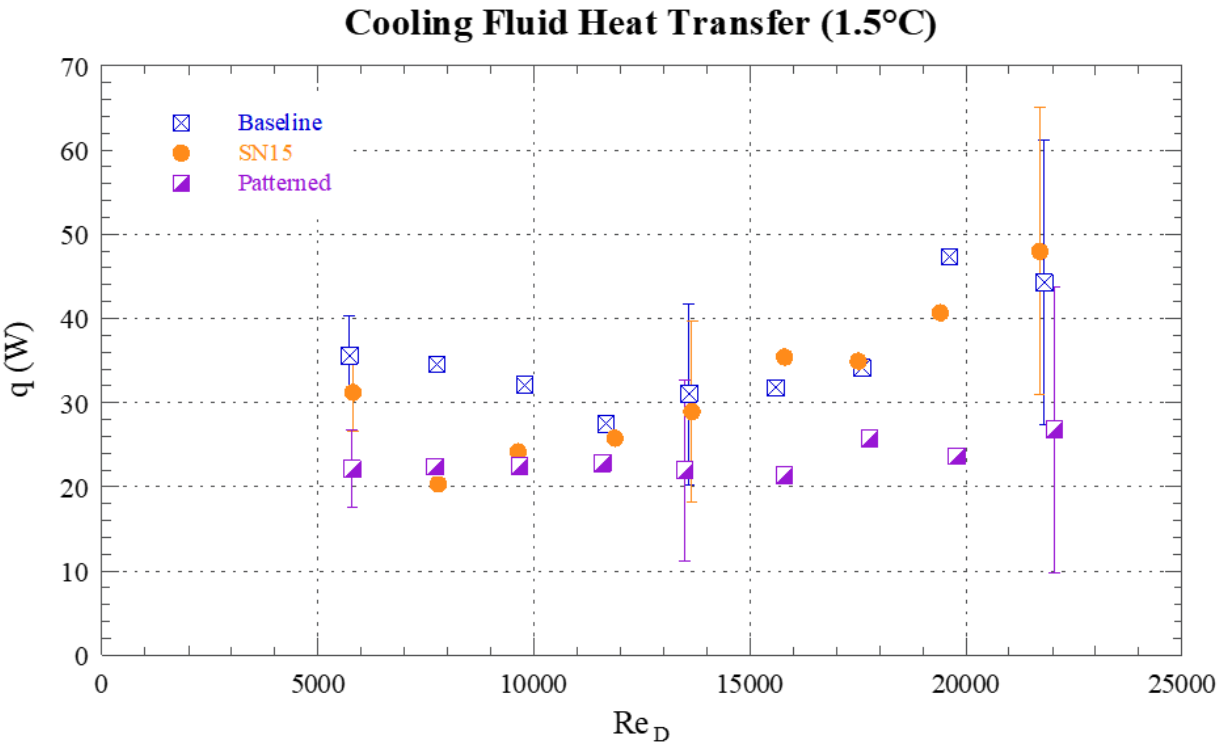

Figure 38. *Comparison of the heat transferred to the cooling fluid (q) for the patterned surface, the baseline surface, and the SN15 sample at 1.5°C of subcooling.*

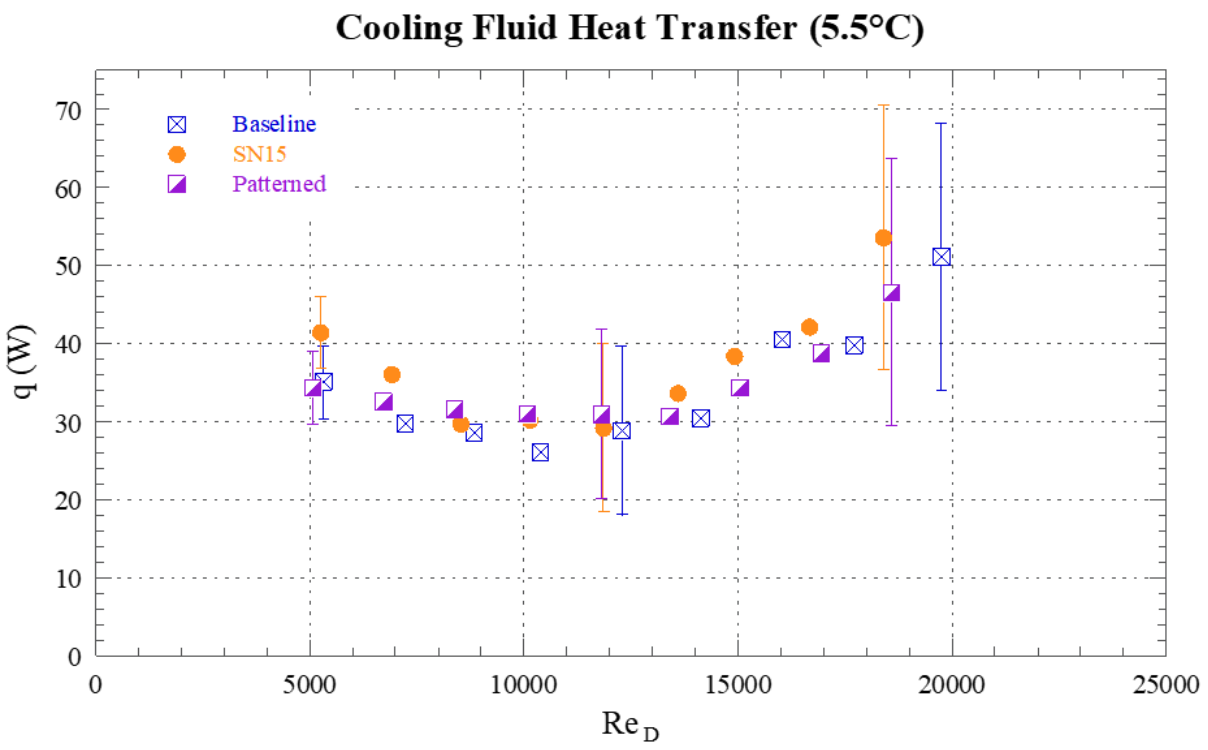

Figure 39. *Comparison of the heat transferred to the cooling fluid (q) for the patterned surface, the baseline surface, and the SN15 sample at 5.5°C of subcooling.*

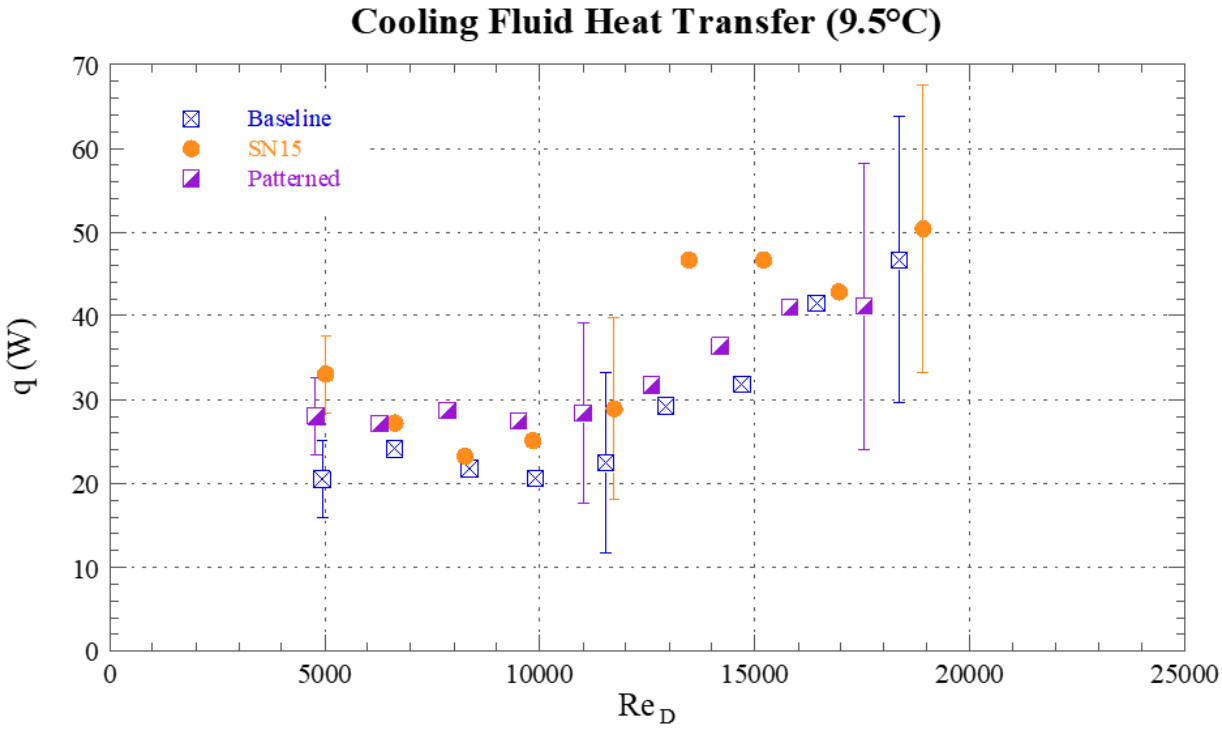

Figure 40. *Comparison of the heat transferred to the cooling fluid (q) for the patterned surface, the baseline surface, and the SN15 sample at 9.5°C of subcooling.*

5.6 Condensate Removal Quantification

Based on the results of the condensation heat transfer testing, the importance of quantifying the amount of water being removed from each sample during condensation testing became clear. In order to complete this quantification, an analysis of the videos taken during testing was performed. All the videos analyzed were taken at a flowrate of 5.5 LPM for each sample and at each of the nominal degrees of subcooling. Each video lasted a minimum of 450 seconds (7.5 minutes) to capture a significant number of droplets shedding from the surfaces. First, a count of the number of droplets that left each sample was collected for the duration of the video. The droplet removal rate, in droplets per minute, was calculated for each sample. Because a slightly different tube length was captured in each video, pixel counting in KAPPA ImageBase software was used to determine these lengths. The droplet removal rate was then normalized based on this length. A column chart of this normalized droplet removal rate is shown in Fig. 41. From this diagram, it can be seen that the samples containing a silica nanospring coating caused more droplets to shed from the surface, with the SN15 and SN20 coating having the highest droplet removal rate. Movement of smaller droplets is more common on the coated samples than the baseline sample due to their hydrophobic nature. The repellency of the surface allows these smaller droplets to then completely detach from the surface.

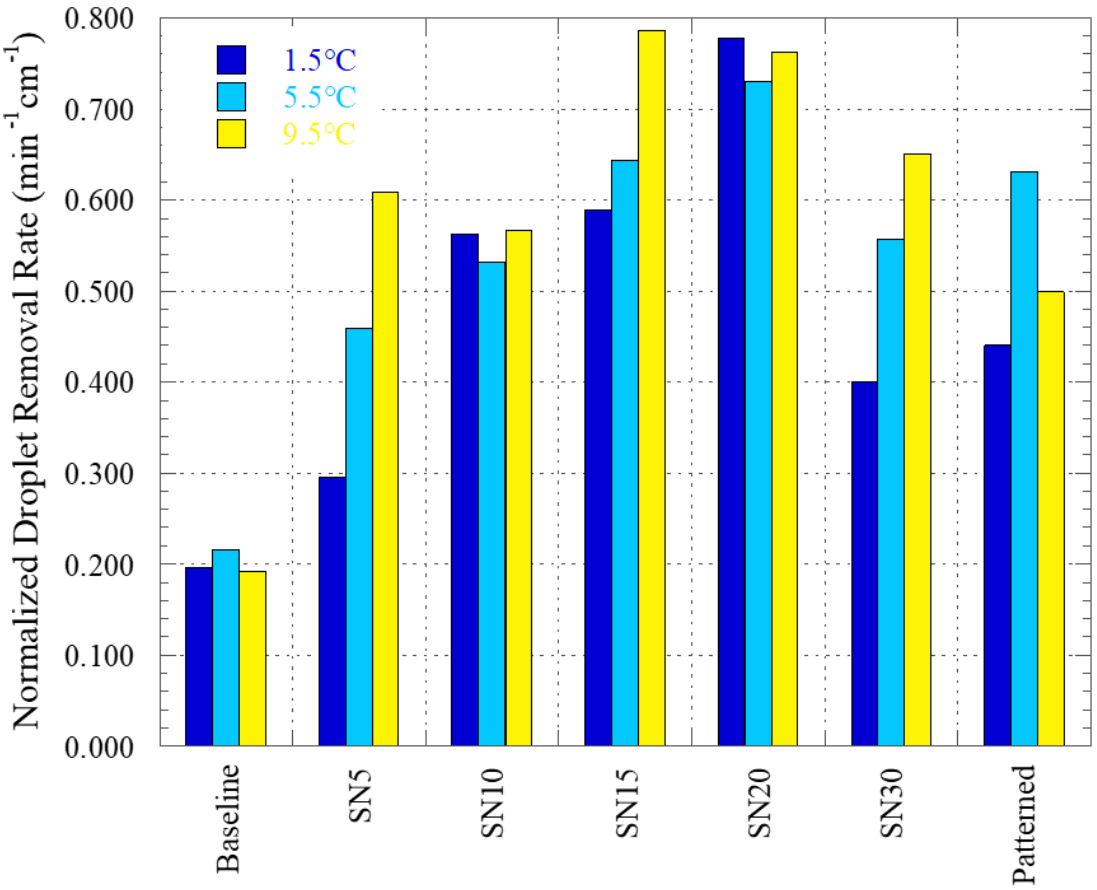

Figure 41. *Comparison chart of the normalized droplet removal rate for each sample at each nominal subcooling. The results are normalized per length of the tested tube captured in the images.*

Although the coated samples were capable of shedding more droplets from the surface than the baseline sample, it was clear within the videos that the droplets from the baseline sample were larger than the droplets from the nanospring-coated surfaces (See Fig. 28). The fact that smaller droplets were capable of draining from the coated surfaces was beneficial, but the amount of water volume removed from the surface is also important from a heat transfer perspective. Because of this, it was important to try to measure the average droplet diameter leaving each sample. Still-images of droplets leaving the surface were captured from the videos and pixel counting was used to measure the average droplet diameter for each sample (see Fig. 42). A minimum of 10 droplets were measured and averaged for each sample. A comparison chart of the average diameter measurement can be found in Fig. 43. As previously noted, the droplets departing from the baseline sample were larger than the droplets from any of the silica nanospring-coated surfaces. However, the silica nanospring samples still had droplets that were relatively close in diameter to the baseline

surface. It is also important to note that the patterned surface removed droplets larger in diameter than any of the uniformly coated samples (see Fig. 43). This suggests that the sample was capable of causing droplets to coalesce into larger droplets with more mass in the hydrophilic regions. Thus, this helps to show the benefit of using a patterned surface. By using the average droplet diameter and the condensation removal rate previously discussed, it was possible to approximate the amount of condensate that was removed from each sample in order to get a more complete quantification of the condensate removal rate for each sample.

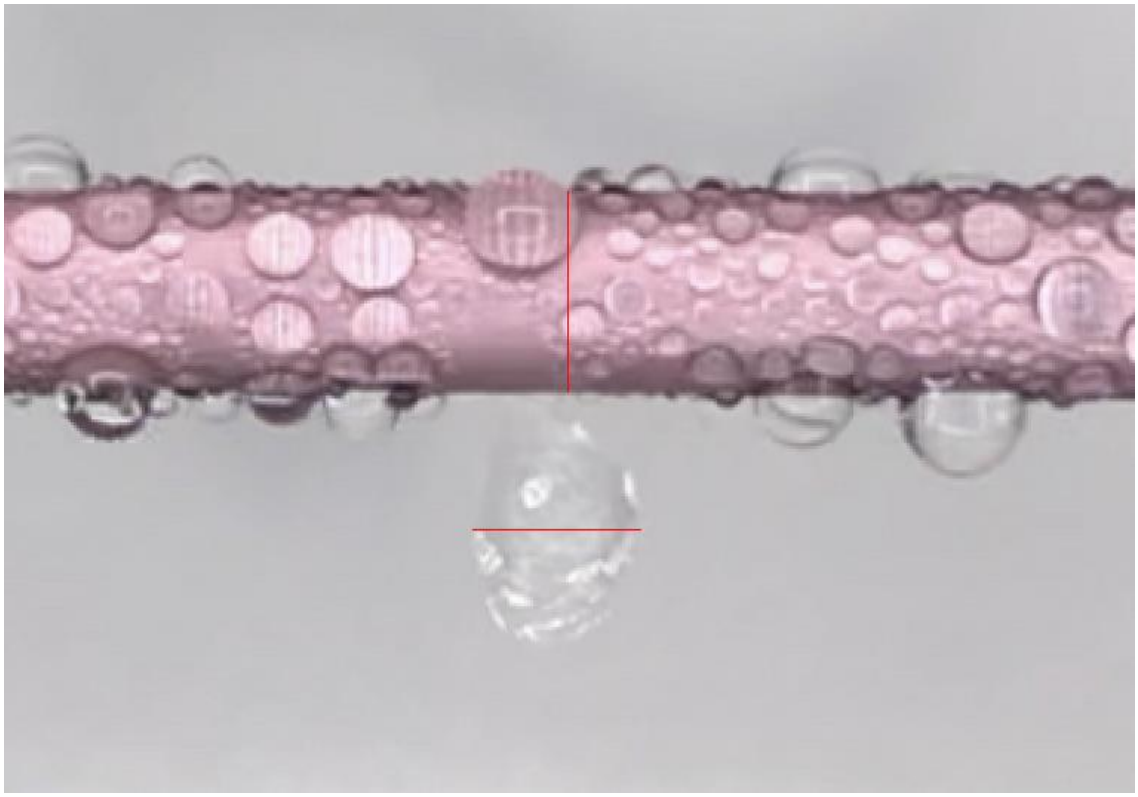

Figure 42. *Droplet diameter measurement as a droplet falls from a nanospring-coated sample.*

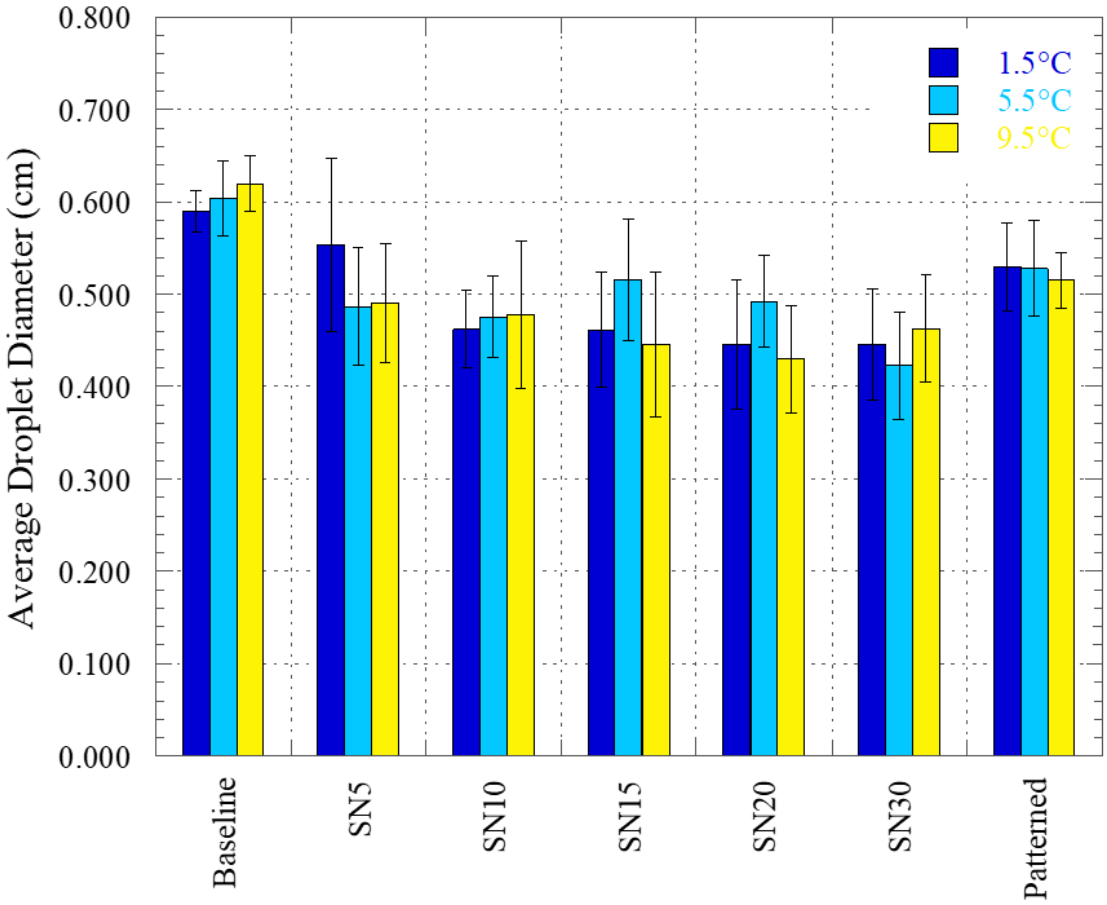

Figure 43. *Comparison diagram of the average droplet departure diameter for each sample at each nominal subcooling.*

To quantify the amount of condensate being removed from each surface, the average droplet volume would have to be approximated. In a study by Hugli and Gonzalez, three different methods for determining a droplet's volume with the use of image processing were evaluated [45]. Of the three methods evaluated, only one could be conducted with the information gathered in this study: approximating the droplet volume based on a spherical model. Using this method, the droplet volume could be calculated as:

$$V = \frac{\pi}{6} D_{max}^3, \tag{18}$$

where V is the volume and D_{max} is the maximum diameter of the droplet on the axis perpendicular to the droplet motion. With this study, a number of droplets with a variety of shapes were evaluated

using the visual methods. The maximum error that was incurred by the use of the spherical model was 20%.

The average droplet volume was calculated based on the average droplet diameter for each sample using the spherical model approximation. The normalized volumetric removal rate was determined for each sample as a function of the normalized droplet removal rate and the average droplet volume. Again, this quantity was normalized based on the length of tube captured in each video. A comparison of the normalized volume removal rate is shown in Fig. 44. From this chart, it can be seen that significantly more condensate was removed from some of the coated samples than the baseline sample. These calculations also show the patterned sample had the highest volumetric removal rate, further showing the pattern was functioning as desired. By forcing droplets to move to unified locations, more mass was capable of being gathered as the droplets were shed from the surface. Although significant differences were not capable of being seen within the heat transfer quantification, this result shows that the coated samples were removing significantly more condensate from the surface than the baseline sample. As a result, significant differences in the heat transfer performance could be realized by altering the testing setup and test conditions. With the use of the SN15 and SN20 uniform coating, the volumetric removal rate increased by 84% over the baseline removal rate, while the patterned sample experienced a 96% increase over the baseline sample.

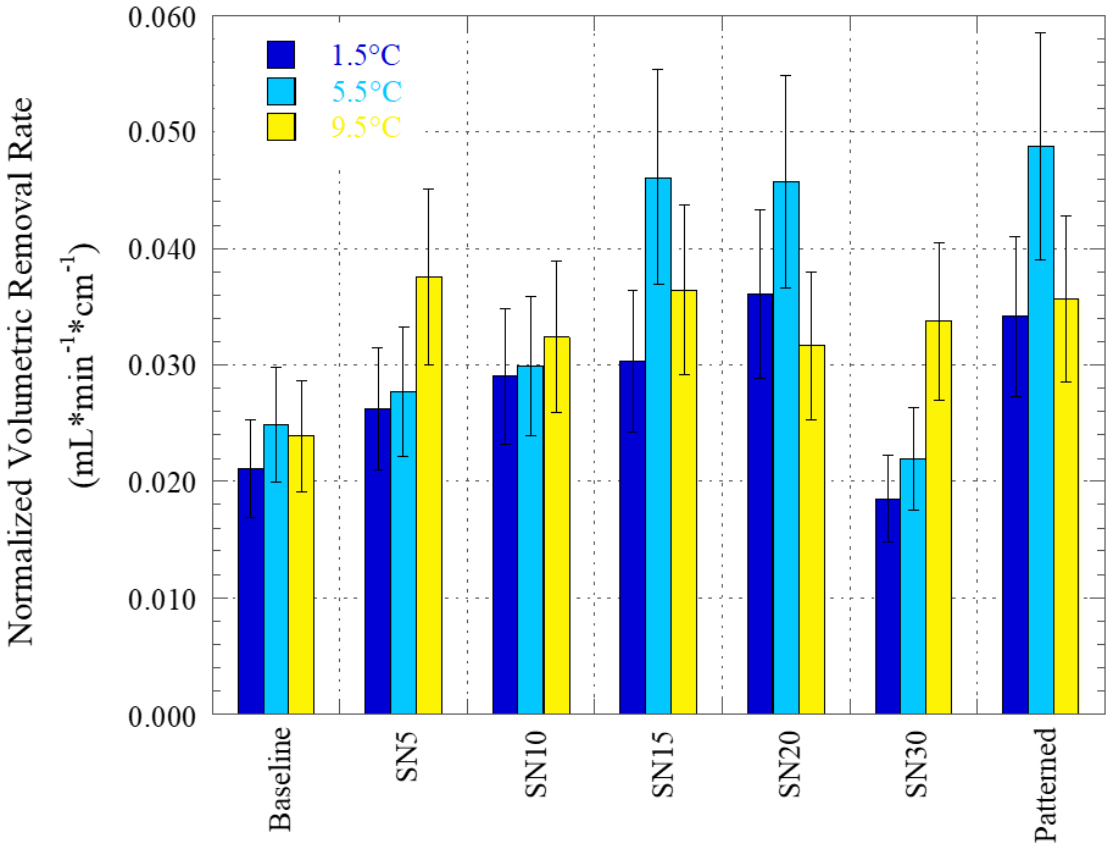

Figure 44. *Comparison chart of the normalized volumetric removal rate for each sample at each nominal subcooling.*

5.7 Durability Assessment

Finally, the durability of each sample was assessed through the use of visual imaging and SEM imaging. Comparison images containing an untested sample and a tested sample can be found in Figs. 45 and 46. In these images, the untested sample is on the left, while the tested sample is on the right. From these images, the first thing to note is that both the baseline sample and the SN5 sample have significantly changed visually as a result of testing. An examination of these two samples revealed that some substance has been deposited on each surface. The deposits appear in a pattern that corresponds to the condensation behavior exhibited by each sample. With the tested baseline sample, the deposition uniformly coats the surface, while the SN5 sample has localized regions where the deposition has occurred (see Fig. 45). Interestingly, these depositions were not present on the other samples used during testing. In order to determine the composition of these deposits, XEDS was used to generate a spectrum for the tested baseline sample (see Fig. 47). When

comparing this spectrum to the untested baseline spectrum in Fig. 20, the newly identified elements contain sodium (Na), chlorine (Cl), and potassium (K). The presence of these elements suggests some form of salt had contaminated the condensing fluid within the chamber. As the condensate formed on the tube, these elements were likely deposited on these surfaces. It is important to note that these deposits were not present on the coated samples with growth times longer than 5 minutes despite the same test water being used for each sample. This can be explained based on the wettability of the samples. One benefit of hydrophobic surfaces is the ability for self-cleaning due to the increased capability of shedding water from the surface. Because of this, the droplets are not capable of depositing any ions on the surface because the droplets are being expelled from the sample. Based on these visual durability results, further analysis was needed to assess the post-testing integrity of the nanospring mat. This analysis was completed with the use of SEM imaging.

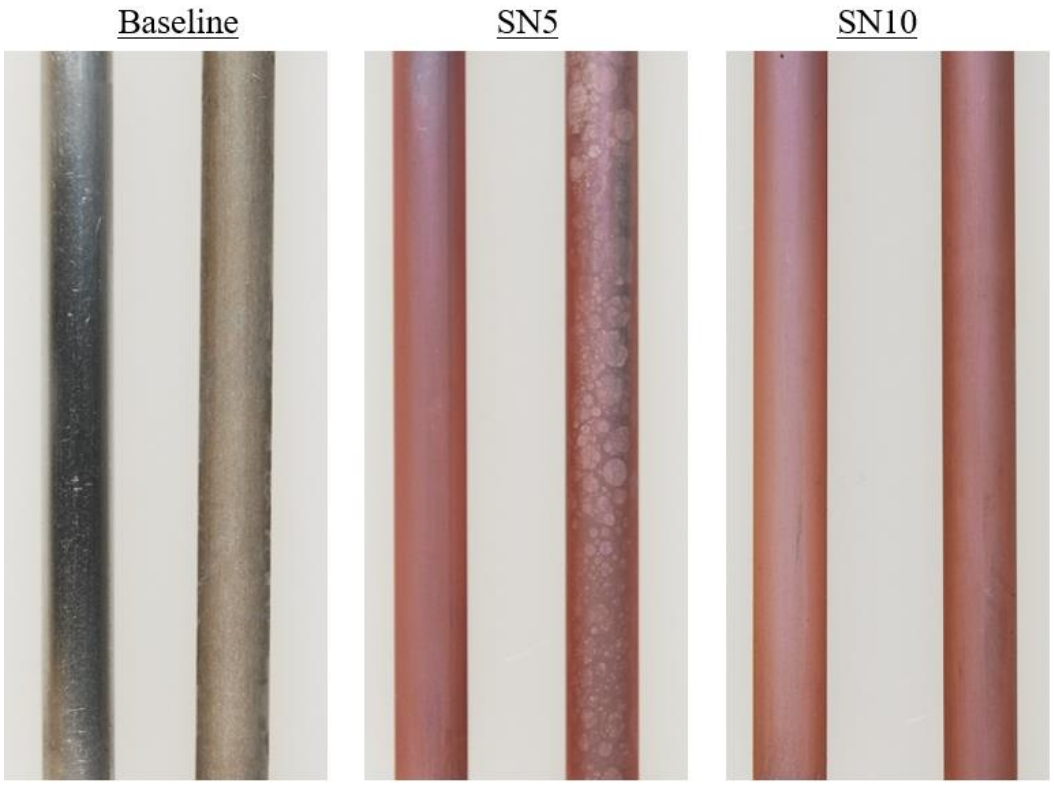

Figure 45. *Pictures of untested (left) and tested (right) baseline, SN5, and SN10 samples for durability assessment.*

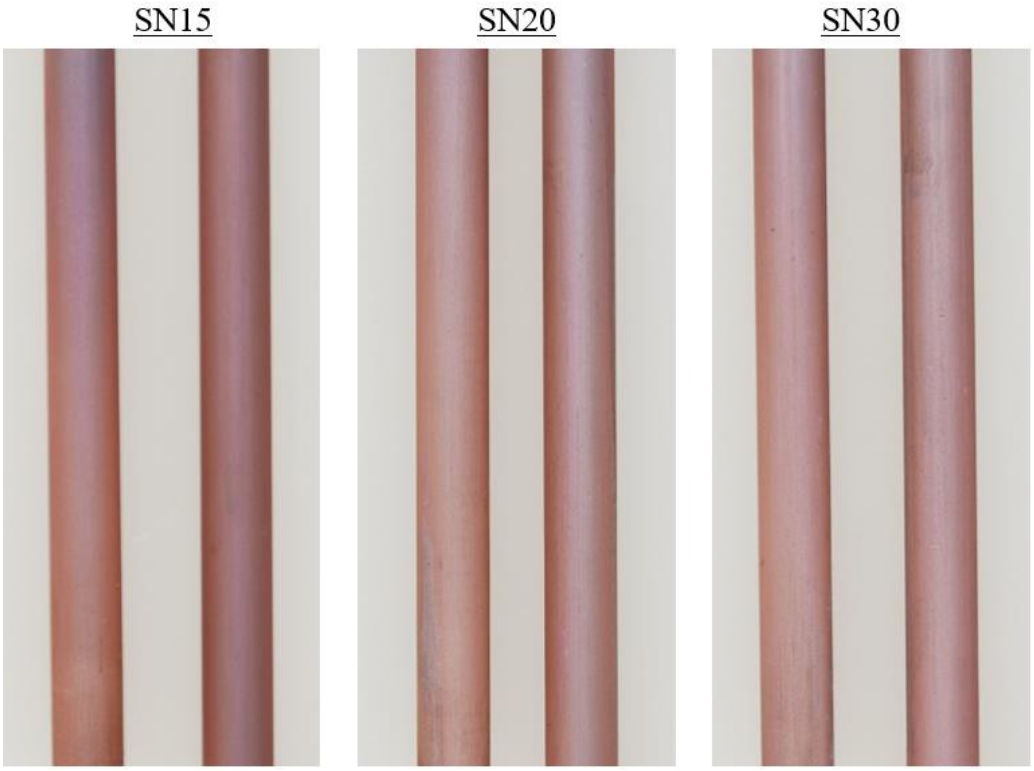

Figure 46. *Pictures of untested (left) and tested (right) SN15, SN20, and SN30 samples for durability assessment.*

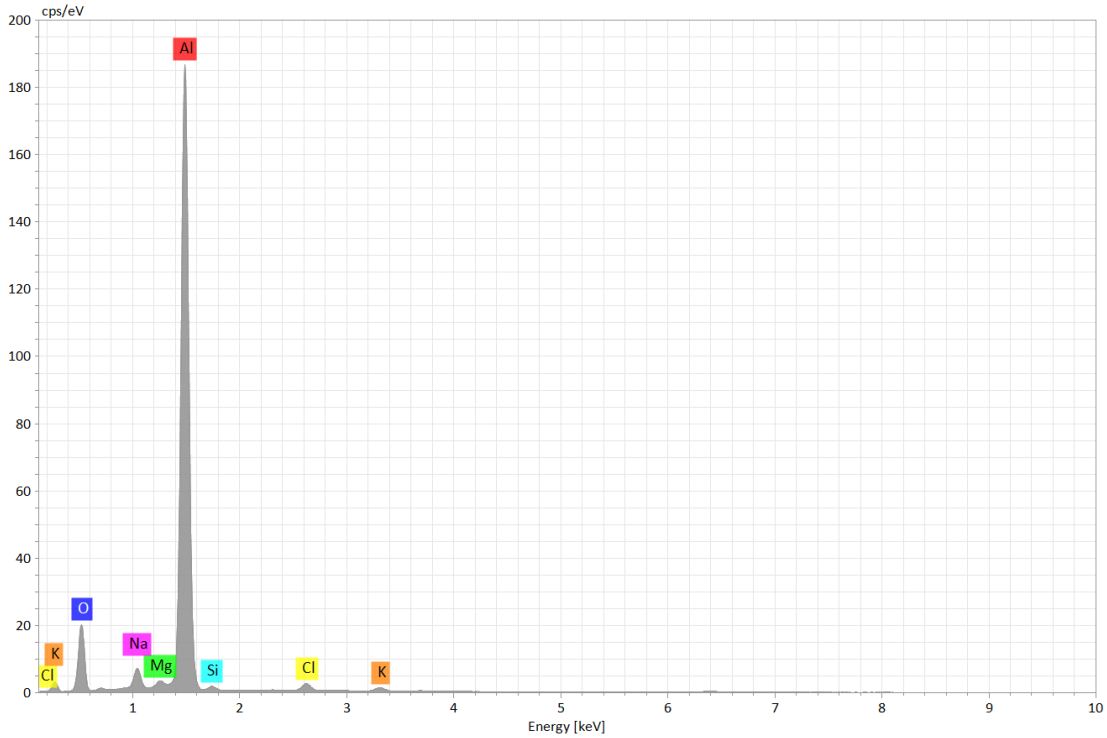

Figure 47. *XEDS spectrum of the tested baseline aluminum surface.*

Comparison SEM images of both untested and tested samples are presented in Figs. 48 and 49. In the image of the tested baseline sample, the previously discussed deposition can be seen covering the sample in the upper half of the image. Only small regions of the underlying aluminum substrate were visible, as seen in the lower half of the image. As was seen in the picture of the untested baseline sample in Fig. 45, these deposits were uniformly present along the tested portion of the sample. Higher magnification images of the tested SN5 sample show the crystalline nature of the deposits on the nanospring mat. This is consistent with the crystalline nature of salts. Contrary to the baseline sample, the deposits on the SN5 sample were more dispersed on top of the mat, rather than uniformly coating the sample. High concentrations of these deposits were present in some areas, as indicated by the tested SN5 sample in Fig. 45, but the silica nanospring mat was still visible between these deposits. This suggests that the SN5 sample still exhibited some of the self-cleaning behavior. These salt crystals were not present on the other silica nanospring-coated samples, further confirming the results gathered from the previously discussed pictures. In looking at the SEM images of the other samples after testing, the nanospring mat still had a similar structure as prior to testing. Thus, the nanospring structures within the mat do not appear to have been damaged throughout the testing process.

The comparisons between the tested and untested samples help to further explain the results noted from the condensation testing. The SN5 sample offered relatively poor heat transfer performance when compared to the other samples. The greater wettability (hydrophilicity) exhibited by the SN5 sample resulted in less water being removed from the surface and allowed for deposits to be placed by the condensate on the surface. The SN15 and SN20 showed good durability with the nanospring structures not being affected by the testing procedure. As a result, these samples were capable of maintaining their hydrophobicity allowing for more condensate to drain off the surface. As a result, these samples offered relatively good heat transfer performance. Based on the results in the pictures in SEM images, it can be concluded that as long as the coating is sufficiently hydrophobic to facilitate frequent droplet removal, the silica nanosprings offer a satisfactory durability within a condensation environment.

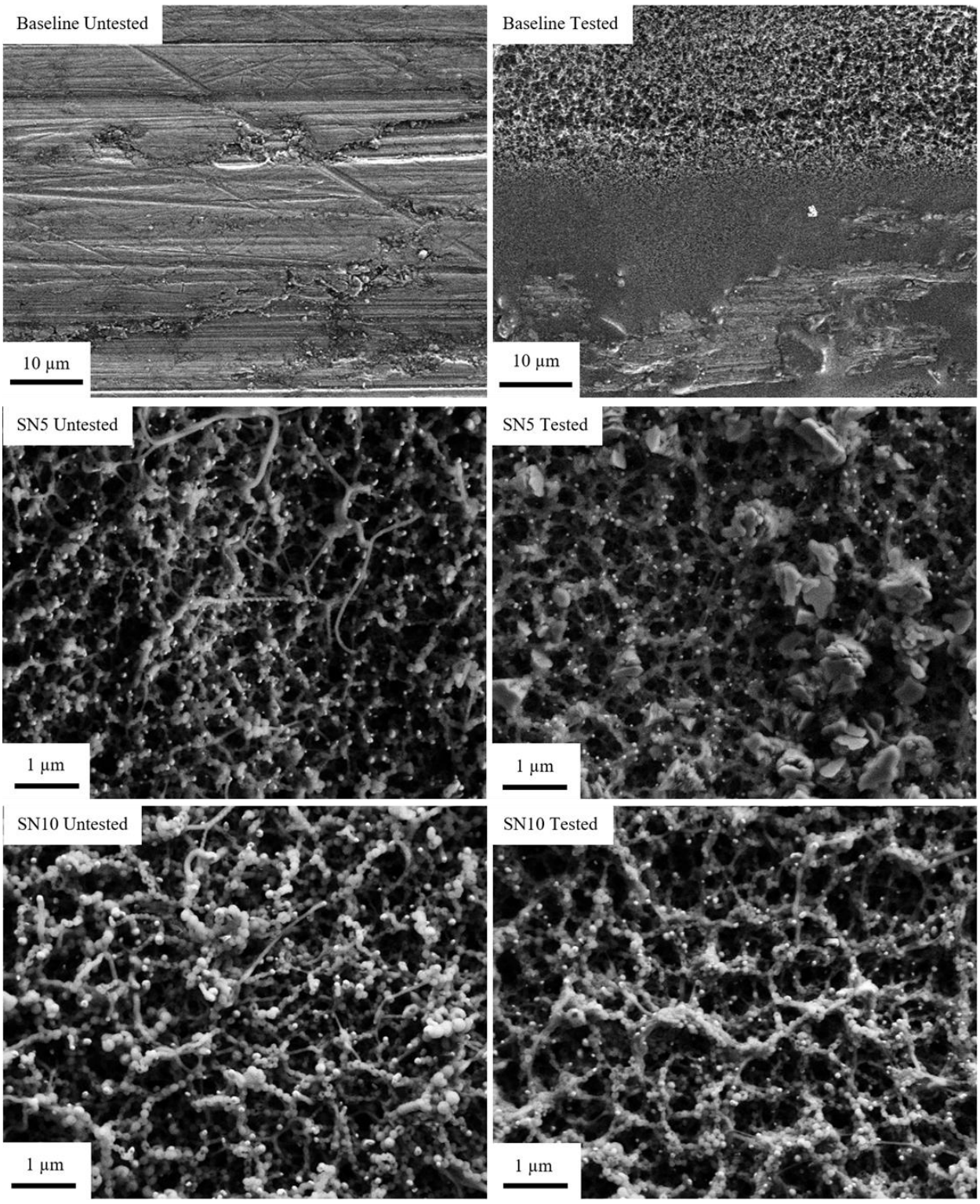

Figure 48. *SEM images comparing the untested and tested baseline, SN5, and SN10 samples.*

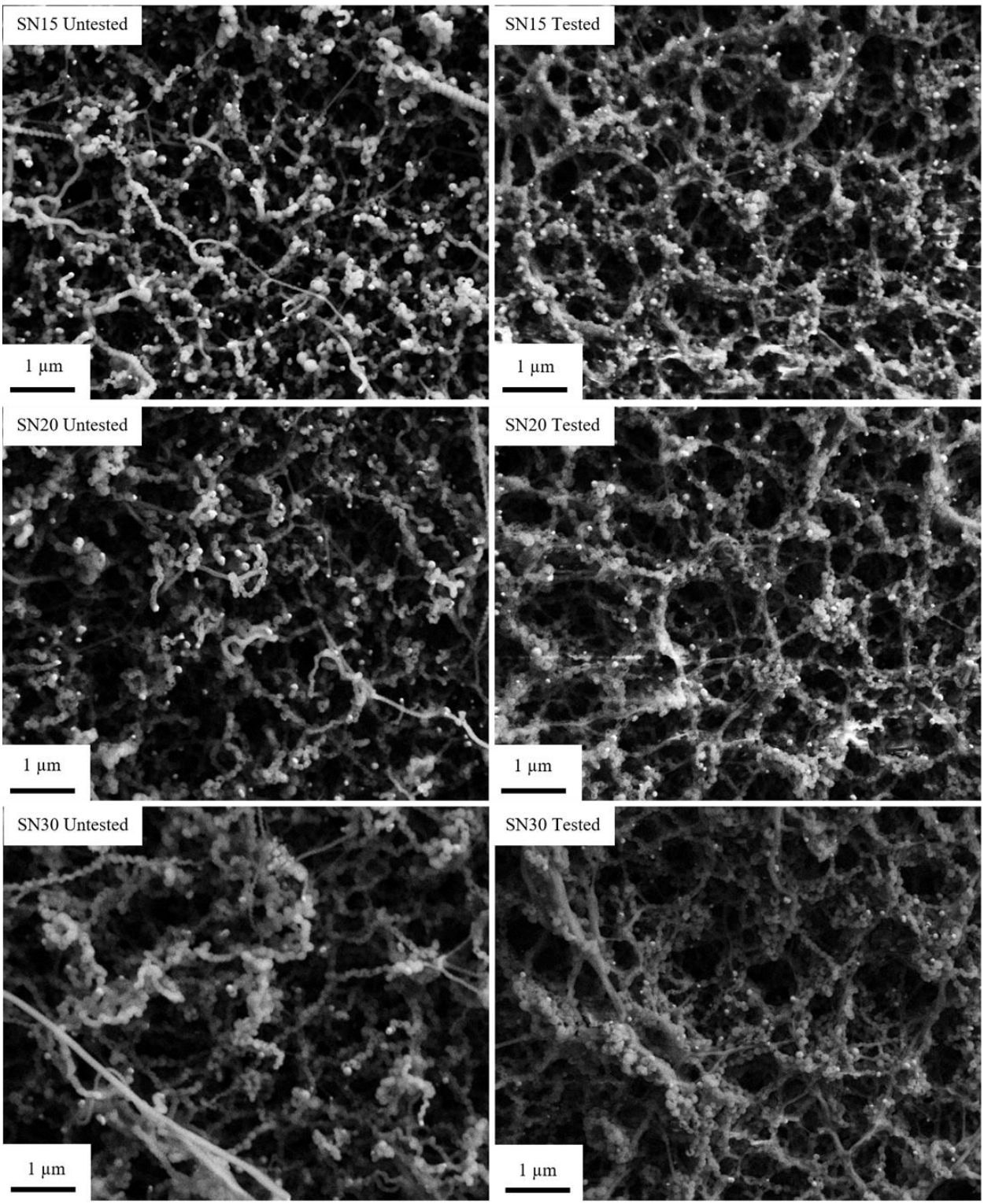

Figure 49. *SEM images comparing the untested and tested SN15, SN20, and SN30 samples.*

6.0 CONCLUSIONS

In this work, an amorphous silica nanospring coating was characterized and assessed for its ability to improve condensation heat transfer performance. Aluminum tubes coated with silica nanosprings were tested against an uncoated baseline aluminum sample. Nanospring mats with thicknesses ranging from 784 nm to 2902 nm were assessed. Contact angle measurements showed that the coating was significantly more hydrophobic than the naturally hydrophilic bare aluminum. Condensation heat transfer experiments were performed within an evacuated controlled environment chamber. In this testing, the bare aluminum tube promoted filmwise condensation, while the nanospring samples promoted dropwise condensation. Previous studies have shown that the promotion of dropwise condensation is beneficial for condensation heat transfer applications due to the decreased thermal resistance and better condensate shedding. During this testing, only small temperature differences were experienced as a result of a short test section. Because of this, statistically significant differences in the heat transfer coefficient calculated for each sample could not be made. However, this testing did appear to show a trend in the performance of the coated samples, with the heat transfer coefficient increasing from the SN5 sample to the SN20 sample and then decreasing with the SN30 sample. In order to further assess the heat transfer performance, the amount of heat transferred to the cooling fluid was calculated for each test. These calculations revealed that the SN15 and the SN20 sample had a comparable heat transfer performance to the baseline sample, and even outperformed the baseline sample at higher degrees of subcooling. The sample SN15 had a heat transfer value approximately 60% higher than the baseline sample at low Reynolds numbers ($Re \approx 5000$) and 9.5℃ of subcooling. Based on these results, the SN15 and SN20 samples offered the best heat transfer performance among the coated samples.

A patterned sample with adjacent hydrophobic and hydrophilic regions was created with the same growth conditions as the SN15 sample. Similar results to the SN15 sample were obtained for the patterned surface during the condensation heat transfer testing with better performance at the high degrees of subcooling. Image and video processing suggested that the rate at which condensate was removed from each sample increased as a result of the application of the silica nanospring coating. It was found that the normalized volumetric removal rate from the SN15 and SN20 samples was 84% higher than the removal rate of the baseline sample, while the removal rate of the patterned sample was 96% higher than the baseline removal rate. Finally, the silica nanospring coating was found to be durable enough to withstand the condensation environment,

provided the coating was thick enough to be considered super-hydrophobic. Additional condensation testing should be performed with a longer test section length in order to better assess the heat transfer performance of the coating, but based on the findings of this study, the silica nanospring coating still appears to be a strong and viable candidate for improving condensation heat transfer performance.

7.0 FUTURE WORK

Within this work, significant differences between the condensation heat transfer coefficients for each sample could not be realized due to small temperature changes that were measured during testing that approached the limitations of the thermocouple accuracies. Because of this, additional condensation testing should be conducted in a manner to increase the temperature difference between the water inlet and outlet in order to make these differences more noticeable. This could be accomplished using multiple methods. First, a simulated serpentine tube could be created by joining multiple straight sections of tube with Swagelok corner fittings. This will nearly triple the length of the test section, increasing the amount of heat transfer that will take place between the surrounding environment and the cooling fluid flowing through the sample tubes. The temperature difference could also be increased by focusing on slower volumetric flowrates of the cooling fluid. By slowing the flowrate, the cooling fluid will spend more time within the test section again allowing more heat to be transferred between the surroundings and the cooling fluid. With these two changes to the test setup and testing procedure, less uncertainty should be present in the calculations and a better characterization of the heat transfer performance of the coating can be made.

Depending on the results of this testing, alterations to the coating itself can also be made. Currently, the surface of the silica nanosprings is terminated with a methyl group (CH_3). This is based on the silane precursor used in the growth process. However, other silane coatings are available that will allow the springs to be functionalized with a group containing a chain of multiple carbons. These groups have been shown to be more hydrophobic than the methyl group. Another alternative functional group that could be considered may be a fluorine group, which have also been shown to have increased hydrophobicity when compared to carbon chains.

Finally, not many coatings have been shown to be both hydrophobic and oleophobic. Because of this, it is desirable to assess how the silica nanospring coating behaves in a hydrocarbon condensation environment. Simple modifications are already capable of being made within the test setup to allow for hydrocarbons to be used as the condensing fluid during testing. Because of this, future testing could be performed to assess the performance of the silica nanosprings in an environment where the condensing fluid is not water. As previously mentioned, different silane functionalization groups may also be considered in order to further modify the hydrophobicity and oleophobicity of the nanospring mat. Further characterization and testing of the silica nanospring

coating should be conducted in order to provide a more complete understanding of the coating and its potential applications.

8.0 SUMMARY

In this work, an amorphous silica nanospring coating was characterized and evaluated on its capabilities for improving condensation heat transfer performance. A number of previous works have investigated other surface modifications for this same purpose. In these works, the surface wettability, that is the degree of hydrophobicity or hydrophilicity, was modified. A common approach is to decrease the surface wettability in order to promote dropwise condensation formation on the surface. The benefits of dropwise condensation include decreasing the amount of thermal resistance posed by the condensate formation on the surface, allowing more water to easily shed from the surface, and creating gaps between droplets on the surface where the underlying surface is capable of having direct contact with the surrounding environment to transfer heat. Previous studies involving the silica nanosprings have suggested that the nanosprings may be a promising candidate for improving the condensation heat transfer performance. This high-surface area coating is made of amorphous silica nanostructures. The nano-scale roughness created by the springs resulted in a superhydrophobic surface coating. A unique feature of the coating is that regions of the underlying substrate are still exposed to the surrounding environment due to the nanosprings launching from gold islands on the surface. The amorphous nature of the silica suggests that the coating may offer beneficial durability. Finally, lithography can be used to control where the coating is applied, and the nanosprings can be functionalized to further modify how they interact with the condensate. Further characterization of the coating was then completed to determine the heat transfer performance of the coating.

Characterization of the coating was conducted in a number of ways. SEM imaging was used to prove the coating was being properly grown on the surface. Various nanospring-coated samples were fabricated in order to determine which mat thickness offered the best performance. Mat thicknesses ranging from 784 nm to 2902 nm were grown. The wettability of each sample was assessed using contact angle measurements. It was determined that increasing the mat thickness resulted in increased hydrophobicity. However, for the growth conditions used, the hydrophobicity reached a plateau for growth times greater than 15 minutes. The performance of the coated samples was compared to an uncoated baseline aluminum sample. Condensation heat transfer tests were conducted in an evacuated chamber. With the data from these tests, the condensation heat transfer coefficient was calculated for each sample. Due to a small degree of temperature change within these tests, no significant differences between the samples could be made. However, as the mat

thickness increased from the SN5 sample to the SN20 sample the heat transfer performance appeared to improve with the SN15 and SN20 samples having comparable performance to the baseline sample. To further assess the heat transfer performance, the amount of heat transferred to the cooling fluid was calculated for each test. Using this metric, it was seen that the SN15 and SN20 samples again offered comparable performance to the baseline sample and even had higher amounts of heat transferred, particularly at higher degrees of subcooling. The sample SN15 had a heat transfer value approximately 60% higher than the baseline sample at low Reynolds numbers ($Re \approx 5000$) and 9.5°C of subcooling. Based on the results of the testing with the uniformly coated samples, a patterned sample was fabricated with adjacent hydrophobic and hydrophilic regions. Because the SN15 sample had some of the best heat transfer performance, the nanospring-coated regions of the patterned surface were grown for 15 minutes in the same manner. Similar to the previous tests, the results for the condensation heat transfer coefficient were comparable to the baseline sample. With the amount of heat transferred to the cooling fluid, the patterned sample had some of the best performance among the samples at the higher degrees of subcooling.

With videos taken during the condensation heat transfer process, the condensate removal of each sample was quantified. A normalized droplet removal rate found that all of the coated samples removed significantly more droplets from the surface than the baseline sample. Still images of falling droplets allowed for the average droplet diameter for each sample to be calculated. The average droplet diameter was largest for the baseline sample (~0.61 cm) with the patterned sample having only slightly smaller droplets (~0.53 cm). The hydrophobic nature of the silica nanospring coating allowed for smaller droplets to move on the surface and shed from the tube. The volumetric removal rate was approximated based on these droplet diameter measurements and the droplet removal rate. It was determined that the normalized volumetric removal rate for the SN15 and SN20 samples was 84% higher than the baseline removal rate, while the removal rate of the patterned sample was 96% higher than the rate of the baseline sample.

Finally, the durability of the nanospring coating was assessed using visual inspection of the samples and further SEM imaging. Based on this analysis, deposits could be seen on both the baseline surface and the SN5 sample. Using XEDS, these deposits were found to be some form of salt left by the water on the sample. These deposits however were not present on the nanospring samples that had been grown for more than 5 minutes, suggesting that the higher degree of hydrophobicity of the thicker mats allowed for the samples to also be self-cleaning. This may also

be of benefit in the heat transfer context. The SN10, SN15, SN20, and SN30 samples showed no obvious signs of damage as a result of the condensation testing procedure, further showing that the coating is durable enough to withstand these conditions.

Based on the results made within this study, a clear conclusion on the ability of the nanospring coating to improve heat transfer cannot be made. The minimal temperature changes during testing limited the ability to show significant differences between the performance of each sample. However, these results do suggest that the nanospring coating may still offer heat transfer benefits. The coated samples were capable of removing more condensate than the baseline tube sample and showed signs of possible heat transfer improvements, especially at higher degrees of subcooling. Further testing should be conducted with longer test sections in order to better assess the heat transfer performance. Overall, the silica nanospring coating still offers promise as a candidate for improving condensation heat transfer performance.

9.0 REFERENCES

[1] Besant, R., and Simonson, C. J., 2003, "Air-to-Air Exchangers," ASHRAE J., **45**(4), pp. 42–54.

[2] Nyman, M., and Simonson, C. J., 2005, "Life Cycle Assessment of Residential Ventilation Units in a Cold Climate," Build. Environ., **40**(1), pp. 15–27.

[3] Bédard, E., Lévesque, S., Martin, P., Pinsonneault, L., Paranjape, K., Lalancette, C., Dolcé, C.-É., Villion, M., Valiquette, L., Faucher, S. P., and Prévost, M., 2016, "Energy Conservation and the Promotion of Legionella Pneumophila Growth: The Probable Role of Heat Exchangers in a Nosocomial Outbreak," Infect. Control Hosp. Epidemiol., **37**(12), pp. 1475–1480.

[4] Martinelli, F., Caruso, A., Moschini, L., Turano, A., Scarcella, C., and Speziani, F., 2000, "A Comparison of Legionella Pneumophila Occurrence in Hot Water Tanks and Instantaneous Devices in Domestic, Nosocomial, and Community Environments," Curr. Microbiol., **41**(5), pp. 374–376.

[5] Guo, Z., Zhou, F., Hao, J., and Liu, W., 2006, "Effects of System Parameters on Making Aluminum Alloy Lotus," J. Colloid Interface Sci., **303**(1), pp. 298–305.

[6] Wu, Y., Saito, N., Nae, F. A., Inoue, Y., and Takai, O., 2006, "Water Droplets Interaction with Super-Hydrophobic Surfaces," Surf. Sci., **600**(18), pp. 3710–3714.

[7] Sun, C., Zhao, X.-W., Han, Y.-H., and Gu, Z.-Z., 2008, "Control of Water Droplet Motion by Alteration of Roughness Gradient on Silicon Wafer by Laser Surface Treatment," Thin Solid Films, **516**(12), pp. 4059–4063.

[8] Barati Darband, Gh., Aliofkhazraei, M., Khorsand, S., Sokhanvar, S., and Kaboli, A., 2018, "Science and Engineering of Superhydrophobic Surfaces: Review of Corrosion Resistance, Chemical and Mechanical Stability," Arab. J. Chem.

[9] McIlroy, D. N., Alkhateeb, A., Zhang, D., Aston, D. E., Marcy, A. C., and Norton, M. G., 2004, "Nanospring Formation—Unexpected Catalyst Mediated Growth," J. Phys. Condens. Matter, **16**(12), p. R415.

[10] Bakharev, P., V. Dobrokhotov, V., and Mcilroy, D., 2014, "A Method for Integrating ZnO Coated Nanosprings into a Low Cost Redox-Based Chemical Sensor and Catalytic Tool for Determining Gas Phase Reaction Kinetics," Chemosensors, **2**, pp. 56–68.

[11] Cantrell, T., Corti, G., Beaux, M., Prakash, T., Mcilroy, D., F Turba, T., and Grant Norton, M., 2010, "Next Generation Nanospring-Enhanced Catalytic Converters," Clean Technol.

[12] Corti, G., Wang, L., Major, D., Branen, J., Jabal, J., Branen, L., Nagler, J., Aston, E., Norton, G., and Mcilroy, D., 2007, "Nanospring-Based Biosensors for Electrical DNA Microarrays," Mater Res Soc Symp Proc, **1010E**, p. No pp given, Paper #: 1010-V05.

[13] Sai, V. V. R., Gangadean, D., Niraula, I., Jabal, J. M. F., Corti, G., McIlroy, D. N., Eric Aston, D., Branen, J. R., and Hrdlicka, P. J., 2011, "Silica Nanosprings Coated with Noble Metal Nanoparticles: Highly Active SERS Substrates," J. Phys. Chem. C, **115**(2), pp. 453–459.

[14] Timalsina, Y. P., Oriero, D., Cantrell, T., Prakash, T., Branen, J., Aston, D. E., Kenneth Noren, Nagler, J. J., Rastogi, S., McIlroy, D. N., and Corti, G., 2010, "Characterization of a Vertically Aligned Silica Nanospring-Based Sensor by Alternating Current Impedance Spectroscopy," J. Micromechanics Microengineering, **20**(9), p. 095005.

[15] Rose, J. W., 2002, "Dropwise Condensation Theory and Experiment: A Review," Proc. Inst. Mech. Eng. Part J. Power Energy, **216**(2), pp. 115–128.

[16] Eslami, F., and Elliott, J. A. W., 2011, "Thermodynamic Investigation of the Barrier for Heterogeneous Nucleation on a Fluid Surface in Comparison with a Rigid Surface," J. Phys. Chem. B, **115**(36), pp. 10646–10653.

[17] Preston, D. J., Mafra, D. L., Miljkovic, N., Kong, J., and Wang, E. N., 2015, "Scalable Graphene Coatings for Enhanced Condensation Heat Transfer," Nano Lett., **15**(5), pp. 2902–2909.

[18] Das, A. K., Kilty, H. P., Marto, P. J., Andeen, G. B., and Kumar, A., 1999, "The Use of an Organic Self-Assembled Monolayer Coating to Promote Dropwise Condensation of Steam on Horizontal Tubes," J. Heat Transf., **122**(2), pp. 278–286.

[19] Tanner, D. W., Pope, D., Potter, C. J., and West, D., 1968, "Heat Transfer in Dropwise Condensation at Low Steam Pressures in the Absence and Presence of Non-Condensable Gas," Int. J. Heat Mass Transf., **11**(2), pp. 181–190.

[20] Tsuchiya, H., Tenjimbayashi, M., Moriya, T., Yoshikawa, R., Sasaki, K., Togasawa, R., Yamazaki, T., Manabe, K., and Shiratori, S., 2017, "Liquid-Infused Smooth Surface for Improved Condensation Heat Transfer," Langmuir, **33**(36), pp. 8950–8960.

[21] Tenjimbayashi, M., Higashi, M., Yamazaki, T., Takenaka, I., Matsubayashi, T., Moriya, T., Komine, M., Yoshikawa, R., Manabe, K., and Shiratori, S., 2017, "Droplet Motion Control on Dynamically Hydrophobic Patterned Surfaces as Multifunctional Liquid Manipulators," ACS Appl. Mater. Interfaces, **9**(12), pp. 10371–10377.

[22] Wen, R., Li, Q., Wu, J., Wu, G., Wang, W., Chen, Y., Ma, X., Zhao, D., and Yang, R., 2017, "Hydrophobic Copper Nanowires for Enhancing Condensation Heat Transfer," Nano Energy, **33**, pp. 177–183.

[23] Porter, M. D., Bright, T. B., Allara, D. L., and Chidsey, C. E. D., 1987, "Spontaneously Organized Molecular Assemblies. 4. Structural Characterization of n-Alkyl Thiol Monolayers on Gold by Optical Ellipsometry, Infrared Spectroscopy, and Electrochemistry," J. Am. Chem. Soc., **109**(12), pp. 3559–3568.

[24] Zhao, C.-Y., Ji, W.-T., Jin, P.-H., Zhong, Y.-J., and Tao, W.-Q., 2017, "The Influence of Surface Structure and Thermal Conductivity of the Tube on the Condensation Heat Transfer of R134a and R404A over Single Horizontal Enhanced Tubes," Appl. Therm. Eng., **125**, pp. 1114–1122.

[25] Gnielinski, V., 1976, "New Equations for Heat and Mass Transfer in Turbulent Pipe and Channel Flow," Int Chem Eng, **16**(2), pp. 359–368.

[26] Miljkovic, N., Enright, R., and Wang, E. N., 2012, "Effect of Droplet Morphology on Growth Dynamics and Heat Transfer during Condensation on Superhydrophobic Nanostructured Surfaces," ACS Nano, **6**(2), pp. 1776–1785.

[27] Rajkumar, M. R., Praveen, A., Arun Krishnan, R., Asirvatham, L. G., and Wongwises, S., 2018, "Experimental Study of Condensation Heat Transfer on Hydrophobic Vertical Tube," Int. J. Heat Mass Transf., **120**, pp. 305–315.

[28] Yang, K.-S., Lin, K.-H., Tu, C.-W., He, Y.-Z., and Wang, C.-C., 2017, "Experimental Investigation of Moist Air Condensation on Hydrophilic, Hydrophobic, Superhydrophilic, and Hybrid Hydrophobic-Hydrophilic Surfaces," Int. J. Heat Mass Transf., **115**, pp. 1032–1041.

[29] Ghosh, A., Beaini, S., Zhang, B. J., Ganguly, R., and Megaridis, C. M., 2014, "Enhancing Dropwise Condensation through Bioinspired Wettability Patterning," Langmuir, **30**(43), pp. 13103–13115.

[30] Alwazzan, M., Egab, K., Peng, B., Khan, J., and Li, C., 2017, "Condensation on Hybrid-Patterned Copper Tubes (I): Characterization of Condensation Heat Transfer," Int. J. Heat Mass Transf., **112**, pp. 991–1004.

[31] Alwazzan, M., Egab, K., Peng, B., Khan, J., and li, C., 2017, "Condensation on Hybrid-Patterned Copper Tubes (II): Visualization Study of Droplet Dynamics," Int. J. Heat Mass Transf., **112**, pp. 950–958.

[32] Wang, L., Major, D., Paga, P., Zhang, D., Norton, M. G., and McIlroy, D. N., 2006, "High Yield Synthesis and Lithography of Silica-Based Nanospring Mats," Nanotechnology, **17**(11), p. S298.

[33] Wojcik, P. M., Bakharev, P. V., Corti, G., and McIlroy, D. N., 2017, "Nucleation, Evolution, and Growth Dynamics of Amorphous Silica Nanosprings," Mater. Res. Express, **4**(1), p. 015004.

[34] Schilke, K. F., Wilson, K. L., Cantrell, T., Corti, G., McIlroy, D. N., and Kelly, C., 2010, "A Novel Enzymatic Microreactor with Aspergillus Oryzae β-Galactosidase Immobilized on Silicon Dioxide Nanosprings," Biotechnol. Prog., **26**(6), pp. 1597–1605.

[35] Hass, J. L., Garrison, E. M., Wicher, S. A., Knapp, B., Bridges, N., McLlroy, D., and Arrizabalaga, G., 2012, "Synthetic Osteogenic Extracellular Matrix Formed by Coated Silicon Dioxide Nanosprings," J. Nanobiotechnology, **10**, p. 6.

[36] Fouetio Kengne, B.-A., Karmakar, S., Kaura, M., Sai, V. V. R., Corti, G., Niraula, I. B., Larin, A., Hall, J., Sowell, D., Hrdlicka, P. J., Dobrokhotov, V., and McIlroy, D. N., 2014, "Self-Assembled Monolayers of Thiols Adsorbed on Au/ZnO-Functionalized Silica Nanosprings: Photoelectron Spectroscopy-Analysis and Detection of Vaporized Explosives," ACS Appl. Mater. Interfaces, **6**(16), pp. 13355–13366.

[37] Corti, G., Brown, J., Rajabi, N., and McIlroy, D. N., 2018, "Threefold Growth Efficiency Improvement of Silica Nanosprings by Using Silica Nanosprings as a Substrate," Nanotechnology, **29**(11), p. 115604.

[38] Norton, M. G., Mcilroy, D., Corti, G., and Miller, M. A., 2009, "Silica Nanosprings- A Novel Nanostructured Material for Hydrogen Storage," Tech. Proc. 2009 NSTI Nanotechnol. Conf. Expo NSTI-Nanotech 2009, **3**, pp. 118–121.

[39] Corti, G., Schmiesing, N. C., Barrington, G. T., Humphreys, M. G., and Sommers, A. D., 2019, "Characterization of Methyl-Functionalized Silica Nanosprings for Superhydrophobic and Defrosting Coatings," ACS Appl. Mater. Interfaces, **11**(4), pp. 4607–4615.

[40] Schmiesing, N. C., Barrington, G. T., Corti, G., and Sommers, A. D., 2018, "Defrosting Performance of Patterned Heat Transfer Surfaces with a Superhydrophobic Silica Nanosprings Coating," *Proceedings of the 17th International Refrigeration and Air Conditioning Conference*, Purdue e-Pubs.

[41] Bhatti, M. S., and Shah, R. K., 1987, "Chapter 4: Turbulent and Transition Flow Convective Heat Transfer in Ducts," *Handbook of Single-Phase Convective Heat Transfer*, John Wiley & Sons, Inc., New York.

[42] Petukhov, B. S., 1970, "Heat Transfer and Friction in Turbulent Pipe Flow with Variable Physical Properties," *Advances in Heat Transfer*, J.P. Hartnett, and T.F. Irvine, eds., Elsevier, pp. 503–564.

[43] Blasius, H., 1913, "Das Aehnlichkeitsgesetz bei Reibungsvorgängen in Flüssigkeiten," *Mitteilungen über Forschungsarbeiten auf dem Gebiete des Ingenieurwesens: insbesondere aus den Laboratorien der technischen Hochschulen*, Springer Berlin Heidelberg, Berlin, Heidelberg, pp. 1–41.

[44] Wada, H., and Kamijoh, T., 1996, "Thermal Conductivity of Amorphous Silicon," Jpn. J. Appl. Phys., **35**(5B), p. L648.

[45] Hugli, H., and Gonzalez, J. J., 2000, "Drop Volume Measurements by Vision," *Machine Vision Applications in Industrial Inspection VIII*, International Society for Optics and Photonics, pp. 60–67.

[46] Davis, A., Engelhardt, J., and Kidd, J., 2017, *MME 449: Hydrocarbon Condensation Final Report*, Miami University.

10.0 APPENDIX

10.1 Thermocouple Calibration

To improve the accuracy of measurements taken during testing, the critical thermocouples used in the test setup were calibrated using a high-precision resistance temperature detector (RTD). For the calibration process, a bath was set at temperatures ranging from 5℃ to 30℃, which contained the range of temperatures expected to be experienced during testing. At each of the calibration temperatures, the isothermal bath temperature was recorded using the RTD and the voltages of each of the thermocouples was recorded using the data acquisition unit (DAQ). A minimum of 60 data points were recorded for each temperature. After data collection, the temperature was plotted with respect to the voltage for each thermocouple, as shown in Fig. A-1. A linear regression was determined for each of the thermocouples and programmed into the DAQ. In order to determine the thermocouple uncertainty, thermocouple temperature measurements based on the calibration equations (see Table A-1) were compared to RTD measurements. The uncertainty associated with each of the thermocouples is also shown in Table A-1.

Table A-1. *Calibration equations and uncertainties associated with the critical thermocouples used during testing.*

Thermocouple	**Calibration Equation**	**Uncertainty**
Cooling Fluid Inlet Thermocouple	$T = 29.276 + 25436V$	±0.035℃
Cooling Fluid Outlet Thermocouple	$T = 29.438 + 25368V$	±0.027℃
Surface Inlet Thermocouple	$T = 30.038 + 25212V$	±0.025℃
Surface Outlet Thermocouple	$T = 30.190 + 25355V$	±0.044℃

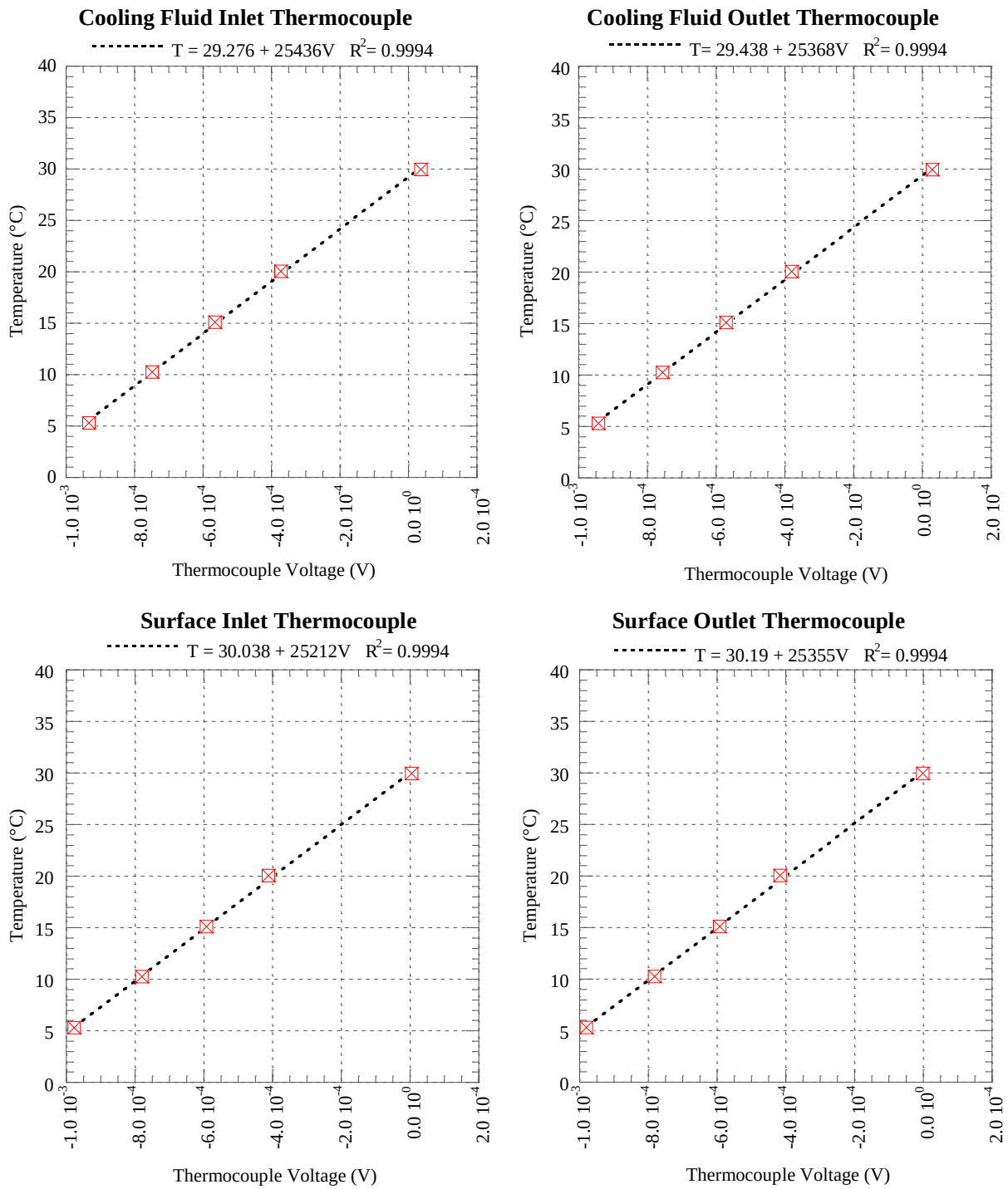

Figure A-1. *Calibration of thermocouple voltage against RTD temperature measurements.*

10.2 Additional Test Setup Images

The condensation testing chamber was developed as part of a senior design project at Miami University during the 2016-2017 school year. An exploded view of the vacuum chamber is shown in Fig. A-2. Additional modifications to the chamber were made to improve the test setup and allow for improved data and media collection. An LED light strip was added to a plastic lining for the interior of the chamber (see Figs. A-3 and A-4). This allowed for better lighting in the chamber and provided a white background for videos and pictures. Wiring for the lighting was fed to the chamber interior through a vacuum suitable fitting. Thermocouples were placed on the exterior walls of the chamber for use with the heat wrap PID controller and to ensure the walls were sufficiently warm enough to prevent condensation formation as in Fig. A-5. A heat wrap was placed around the chamber (see Fig. A-6) and aluminum foil was used to reflect heat back toward the chamber (see Fig. A-7). Finally, the chamber was wrapped in multiple layers of insulation as shown in Fig. A-8.

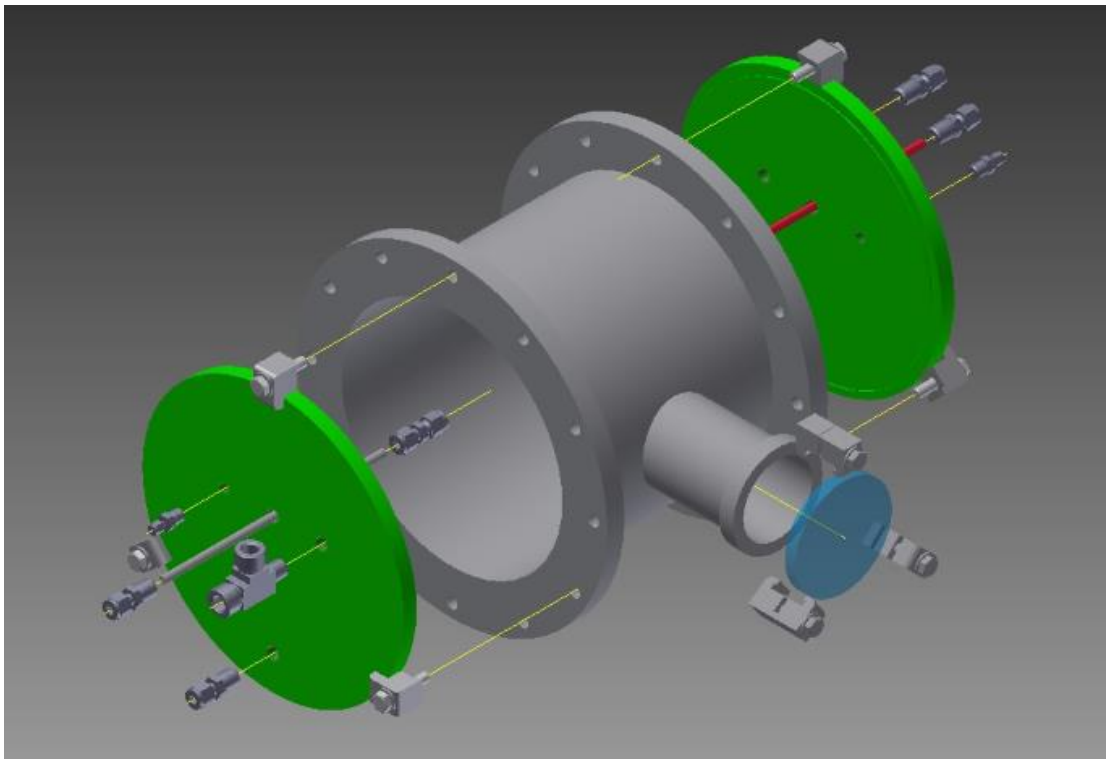

Figure A-2. *Exploded view of the components making up the vacuum chamber for condensation testing, created by a senior design team at Miami University. Taken from [46].*

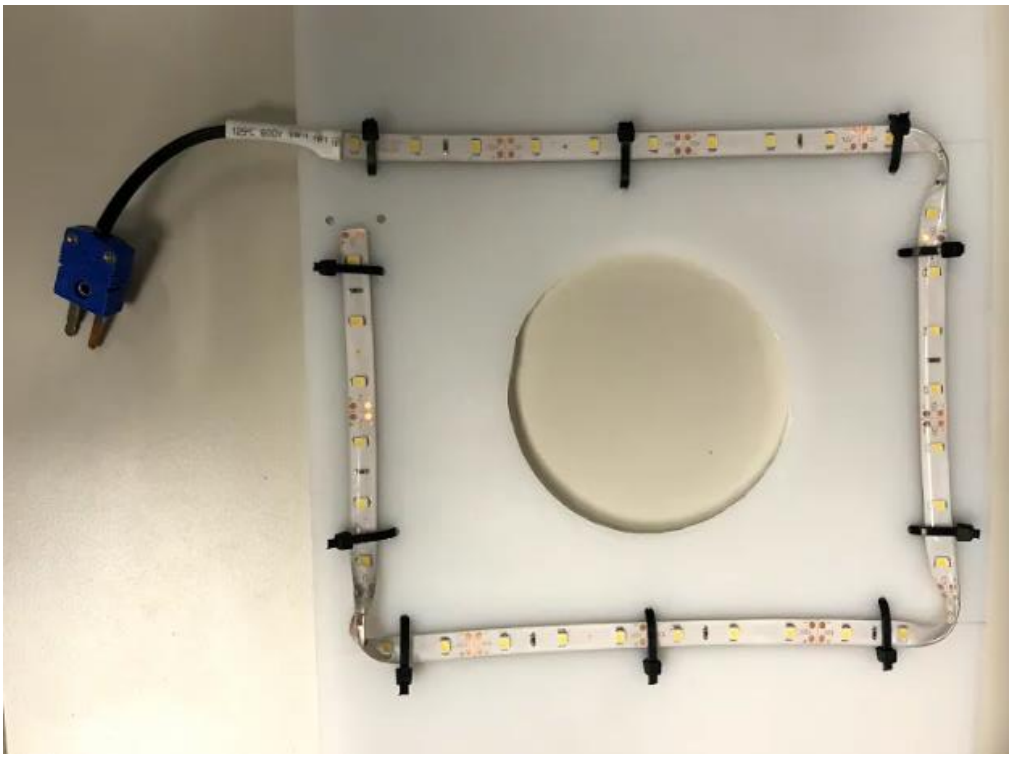

Figure A-3. *LED strip attached to a HDPE lining for the interior of the test chamber.*

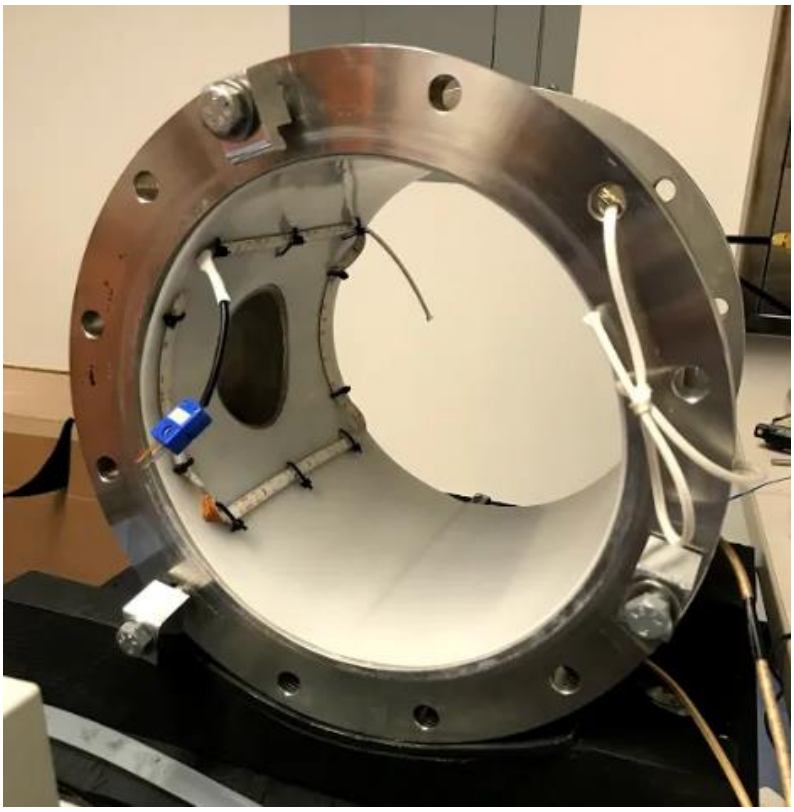

Figure A-4. *Placement of the HDPE lining within the test chamber.*

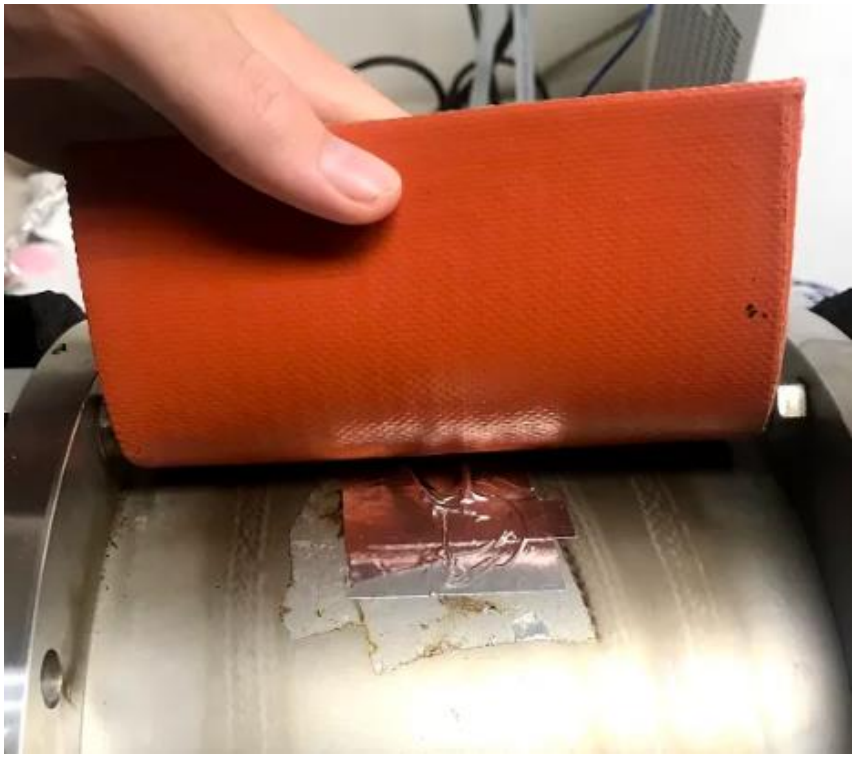

Figure A-5. *Thermocouples placed in contact with the exterior walls of the chamber below the heat wrap.*

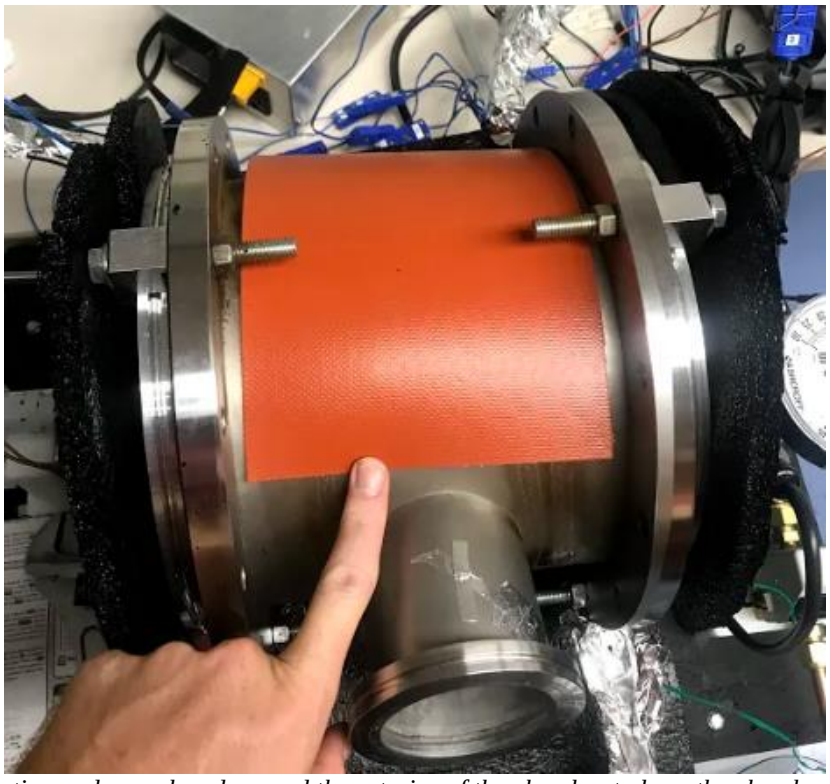

Figure A-6. *A heating pad was placed around the exterior of the chamber to keep the chamber walls sufficiently warm enough to prevent unwanted condensation formation.*

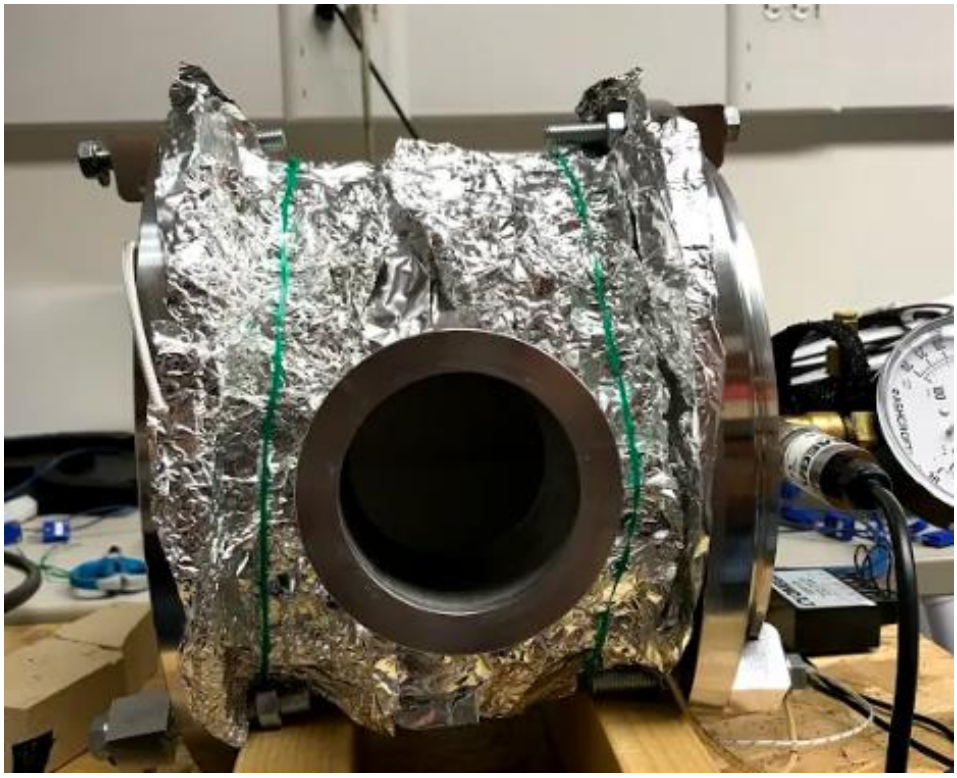

Figure A-7. *Aluminum foil on top of the heating pad reflected heat back toward the chamber.*

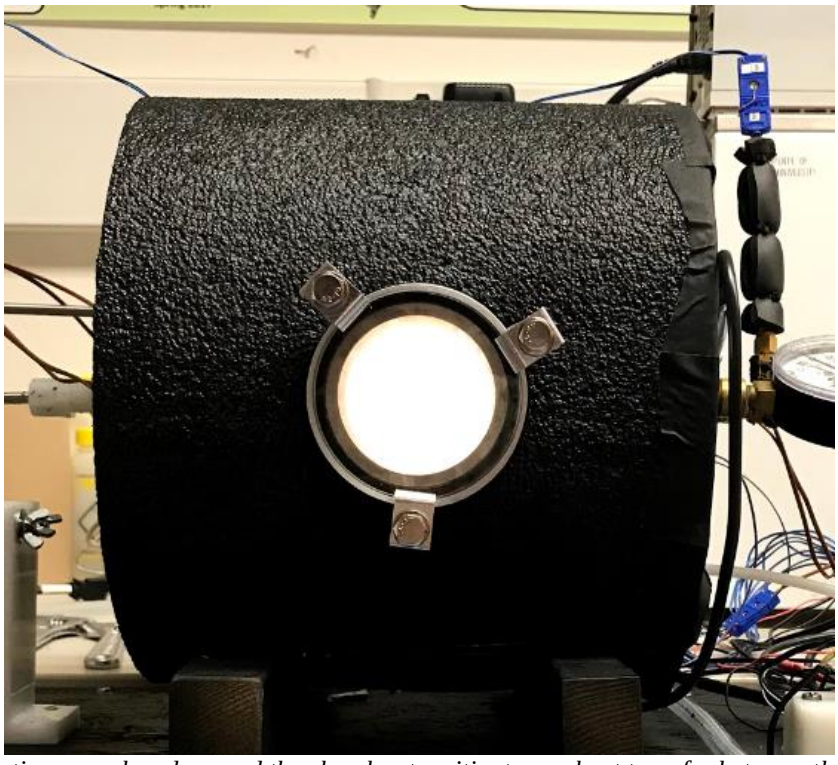

Figure A-8. *Insulation was placed around the chamber to mitigate any heat transfer between the chamber and the surrounding air.*

10.3 EES Program

A program was developed in the Engineering Equation Solver (EES) program to conduct calculations for each of the condensation heat transfer tests that were performed. Built-in functions were used to determine material properties with reference to the data measurements taken throughout testing. A commented form of the EES program used is shown below.

```
"Condition Calculations"
T_infinity = T_sat(Water,P=P) "Surrounding temperature based on
                              pressure"
T_infinity_change = ABS(T_infinity-T_infinity_rec) "Difference
                              between recorded surrounding
                              temperature and surrounding
                              temperature based on pressure"
T_savg = (T_si+T_so)/2        "Average tube surface temperature"
Ts_change=T_so-T_si           "Change in surface temperature
                              between the outlet and inlet"
T_m=(T_mi+T_mo)/2             "Mean cooling fluid temperature"
T_film=(T_infinity+T_savg)/2  "Film temperature"
LMTD = (T_mo-T_mi)/ln((T_infinity-T_mo)/(T_infinity-T_mi)) "Log
                              mean temperature difference"
V_dot = V_rec/(1000*60)       "Volumetric flowrate"
P = P_rec*6894.75729          "Conversion factor from psi to Pa"
T_subcooling = T_infinity - T_m "Degree of subcooling"

"Tube Dimensions and Properties"
D_o = 0.00635 [m]             "Outer tube diameter"
D_i = 0.005334 [m]            "Inner tube diameter"
L = 0.1524 [m]                "Length of the test section"
A_o = pi*D_o*L                "Exterior surface area"
A_i  = pi*D_i*L               "Interior surface area"
A_cs = pi*(D_i/2)^2           "Cross sectional interior tube area"
k_Al = Conductivity(Aluminum_6061, T=T_savg) "Thermal conductivity
                              of tube walls"

"Flowing Water Properties"
P_w = 101325 [Pa]              "Pressure of the cooling fluid"
rho_w=Density(Water,T=T_m,x=0) "Density of the cooling fluid"
rho_w2 = Density(Water,T=T_mi,P=P_w) "Density of the cooling
                                      fluid"
cp= Cp(Water,T=T_m,x=0)        "Specific heat of the cooling
                               fluid"
cp2 = Cp(Water,T=T_mi,P=P_w)   "Specific heat of the cooling
                               fluid"
mu_w= Viscosity(Water,T=T_m,x=0)     "Viscosity of the cooling
                                     fluid"
mu_mean=Viscosity(Water,T=T_m,P=P_w) "Viscosity of the cooling
                                     fluid"
```

```
mu_w2 = Viscosity(Water,T=T_mi,P=P_w) "Viscosity of the cooling
                                       fluid"
mu_s=Viscosity(Water,T=T_savg,P=P_w)  "Viscosity of the cooling
                                       fluid"
k_w= Conductivity(Water,T=T_m,x=0)    "Thermal conductivity of the
                                       cooling fluid"
k_w2 = Conductivity(Water,T=T_mi,P=P_w) "Thermal conductivity of
                                         the cooling fluid"
Pr = Prandtl(Water,T=T_m,x=0)         "Prandtl number of the
                                       cooling fluid"
Pr2 = Prandtl(Water,T=T_mi,P=P_w)     "Prandtl number of the
                                       cooling fluid"
m_dot = V_dot*rho_w                   "Mass flowrate of the
                                       cooling fluid"
u = V_dot/A_cs                        "Average flow velocity of
                                       the cooling fluid"
Re_D = (rho_w*u*D_i)/mu_w             "Reynolds number of the
                                       cooling fluid"


"Method 1 Calculations: Constant Surface Temp"
temp_difference=((T_mo-T_mi)/(T_infinity-T_savg))
h_o_constT=(temp_difference*(m_dot*cp))/A_o

"Method 2 Calculations: Constant External Fluid Temp"
U_bar = ((-m_dot*cp)/A_o)*LN((T_infinity-T_mo)/(T_infinity-T_mi))

"Friction Factor Determination"
f=IF(Re_D,2300,f_1,f_1,f_3)

"Laminar Flow Region"
f_1= 64/Re_D
{*** For Re <= 2300 only ***}

"Turbulent Flow Correlations"
f_2=(1/((1.5635*LN(Re_D/7))^2))*(4)

{Colebrook correlation; within 1% of PKN}
{For Re  > 4000}
f_3=(0.790*LN(Re_D)-1.64)^(-2)
{Petukhov correlation, p. 424 DeWitt textbook}
{3000 <  Re  <  5 x10^6 }
f_4=0.316*(Re_D^(-0.25))
{Turbulent; fully-developed flow}
{For Re < 20,000}

"Nusselt Number Determination"
Nusselt_D=IF(Re_D,2300,Nus_D,Nus_D,Nus_D4)
```

```
"Laminar Flow Correlations"
Nus_D=1.86*term
term=(((Re_D*Pr)/(L/D_i))^(1/3))*(mu_ratio^0.14)
mu_ratio=(mu_mean/mu_s)
{Whitaker correlation; see p. 444 DeWitt textbook (Ch. 8)}
{Laminar Flow: Constant Surface Temp / Accounts for Entrance
Region}
{Combined Entry Length (not fully-developed)}
{0.48 < Pr <16,700}
{0.0044 < mu_ratio < 9.75}
{NOTE: *** Recommended when values of the variable 'term' shown
above > ~2 }
{ Below this limit, fully-developed conditions encompass much of
the tube *** }

Nus_D2=((3.66/(tanh(2.264*(Gz^(-1/3))+1.7*(Gz^(-
2/3)))))+(0.0499*Gz*tanh(1/Gz)))/(tanh(2.432*(Pr^(1/6))*Gz^(-
1/6)))
{Baehr and Stephan correlation, see p. 543 DeWitt textbook (7th
ed.)}
{Laminar Flow: Constant Surface Temp / Accounts for Entrance
Region}
{Combined Entry Length (not fully-developed)}
{Pr >= 0.1}

Nus_D3=3.66+((0.0668*Gz)/(1+0.04*(Gz^(2/3))))
Gz=(D_i/L)*Re_D*Pr
Gz_inverse=1/Gz
{Hausen correlation, see p. 543 DeWitt textbook (7th ed.)}
{Laminar Flow: Constant Surface Temp / Accounts for Entrance
Region}
{Thermal Entry Length (not fully-developed) OR }
{Combined Entry Region (not fully-developed) with Pr >= 5}

"Turbulent Flow Correlations"
Nus_D4 = ((f/8)*(Re_D-1000)*(Pr))/(1+12.7*((f/8)^(1/2))*(Pr^(2/3)-
1))
{Gnielinski correlation, p. 445 DeWitt (Uses Darcy factor)}

{Turbulent; fully developed flow}
{For  Re > 2300  AND  0.5 < Pr < 2000 }
{NOTE:  Does NOT account for entry region since entry lengths for
turbulent flows are}
{typically short. Thus, NuD is often assumed to be equal to the
fully-developed value NuD_fd, }
{except for short tubes. Here, a small correction is sometimes
needed-- see p. 446 in Dewitt}

Nus_D5=(lambda2/2)+(1/(2*x_plus))*LN(lambda2/(8*G_0))
{From: Convective Heat and Mass Transfer, 4th ed., by Kays,
Crawford, and Weigand, pp. 313-315}
```

```
{Thermal Entry Length for Turbulent Flow in Circular Tubes;
Accounts for Entry Region}
{Lambda and G_0 values shown are for Reynolds = 50,000 and Pr = 8}
lambda2=685.6/8.5
G_0=85.4/8.5

x_plus=(L/D_i)/(Re_D*Pr)
{NOTE:  Even with these extrapolated values, Nus_D4 and Nus_D5 are
quite similar.}

"Additional Calculations"
h_i = (Nusselt_D*k_w)/D_i
R_tot = 1/(U_bar*A_o)
R_i = 1/(h_i*A_i)
R_wall = ln(D_o/D_i)/(2*pi*L*k_Al)
h_o = 1/(A_o*(R_tot - R_i - R_wall))
q = m_dot*cp2*(T_mo-T_mi)

"Approximation to Check Value of h_o- see h_o2"
(1/U_bar)=(1/h_i)+(1/h_o2)

{END PROGRAM}
```

10.4 Additional SEM Images of the Samples

Due to the scale of the coating, scanning electron microscopy (SEM) was a critical tool in assessing the growth and performance of the nanospring mats. Additional SEM images are shown below. Figure A-9 exemplifies how the coating uniformly (and conformally) coats the substrate including regions with relatively large topographical changes. A variety of different spring structures that form during the nanospring growth process can be seen in Fig. A-10. Additional images of the mat thickness measurements for each sample are shown in Figs. A-11 through A-15. The annotations in these images show how significantly the mat thickness increases with each increase in the growth duration.

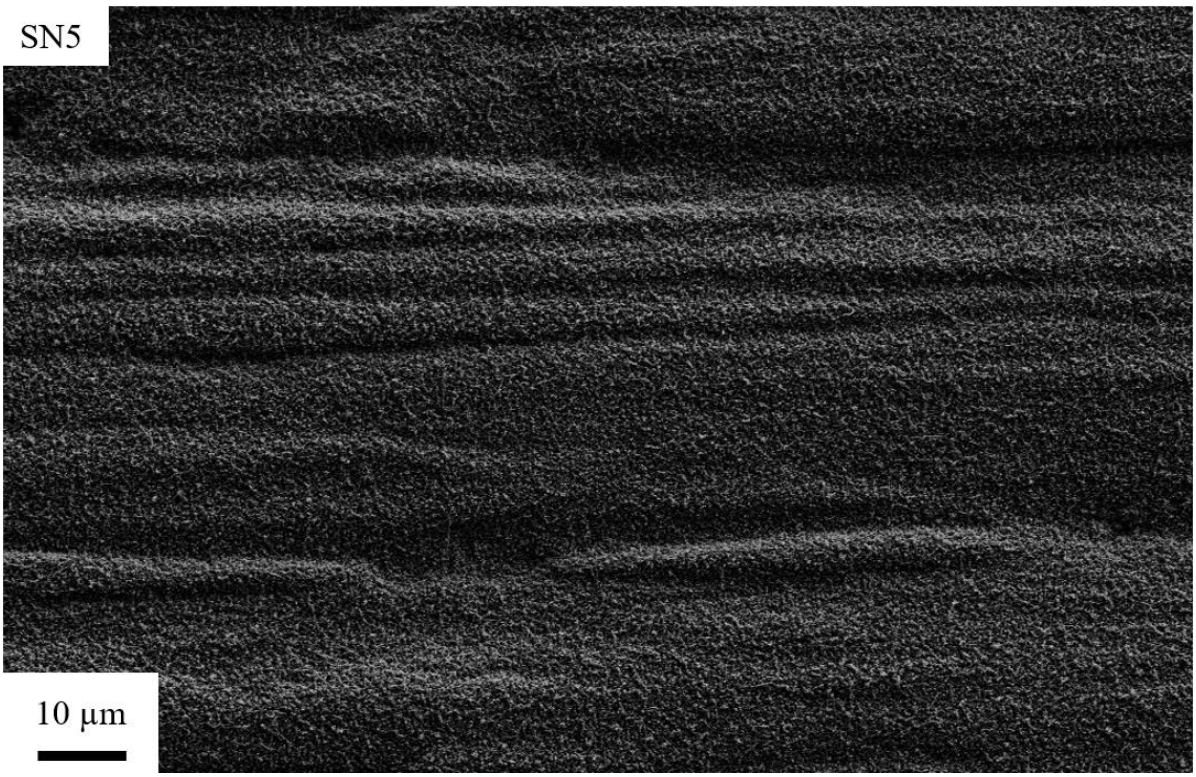

Figure A-9. *The silica nanospring mat uniformly coats each sample, including relatively rough regions.*

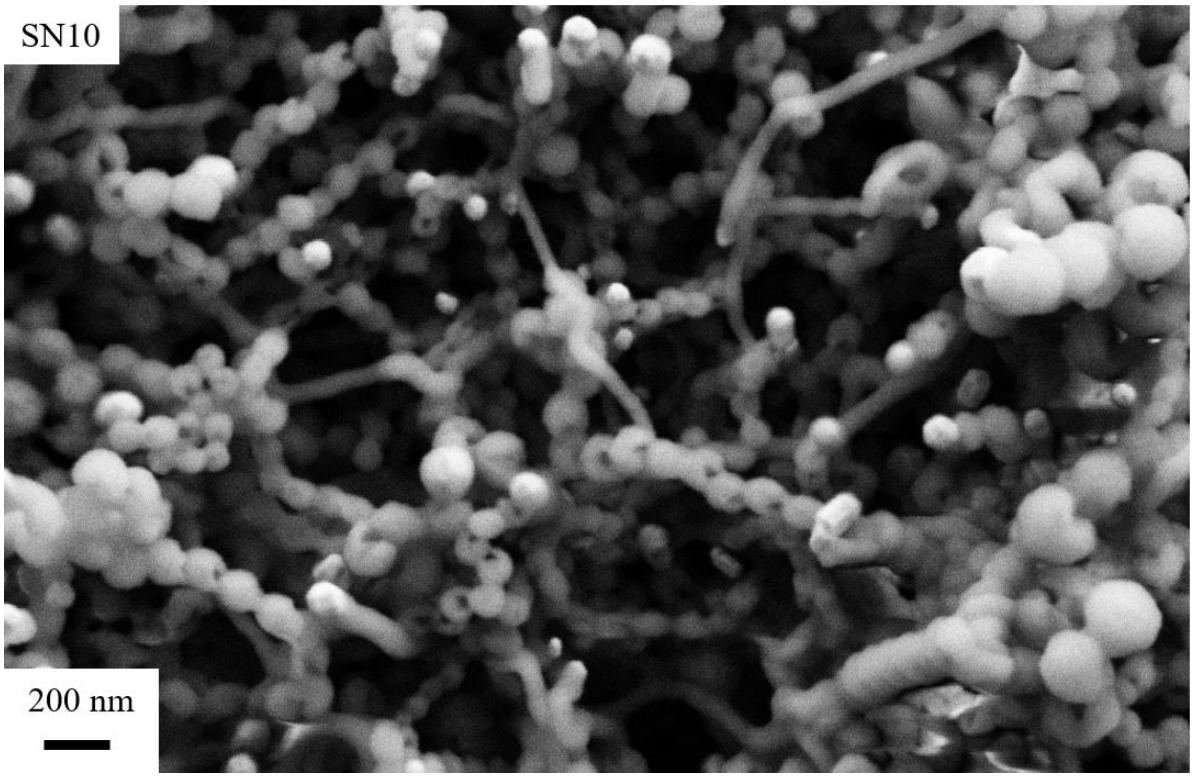

Figure A-10. *A variety of different spring structures grow within each nanospring mat.*

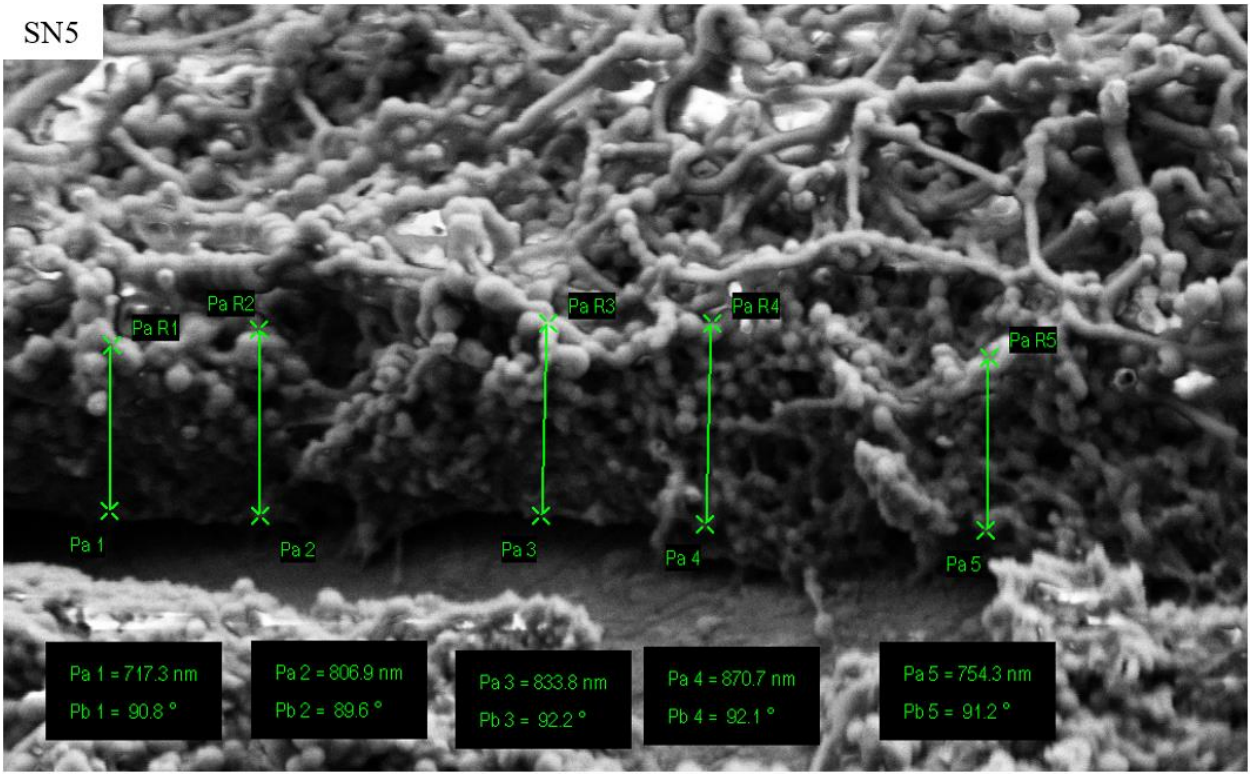

Figure A-11. *An annotated SEM micrograph of the SN5 sample used to measure the thickness of the nanospring mat.*

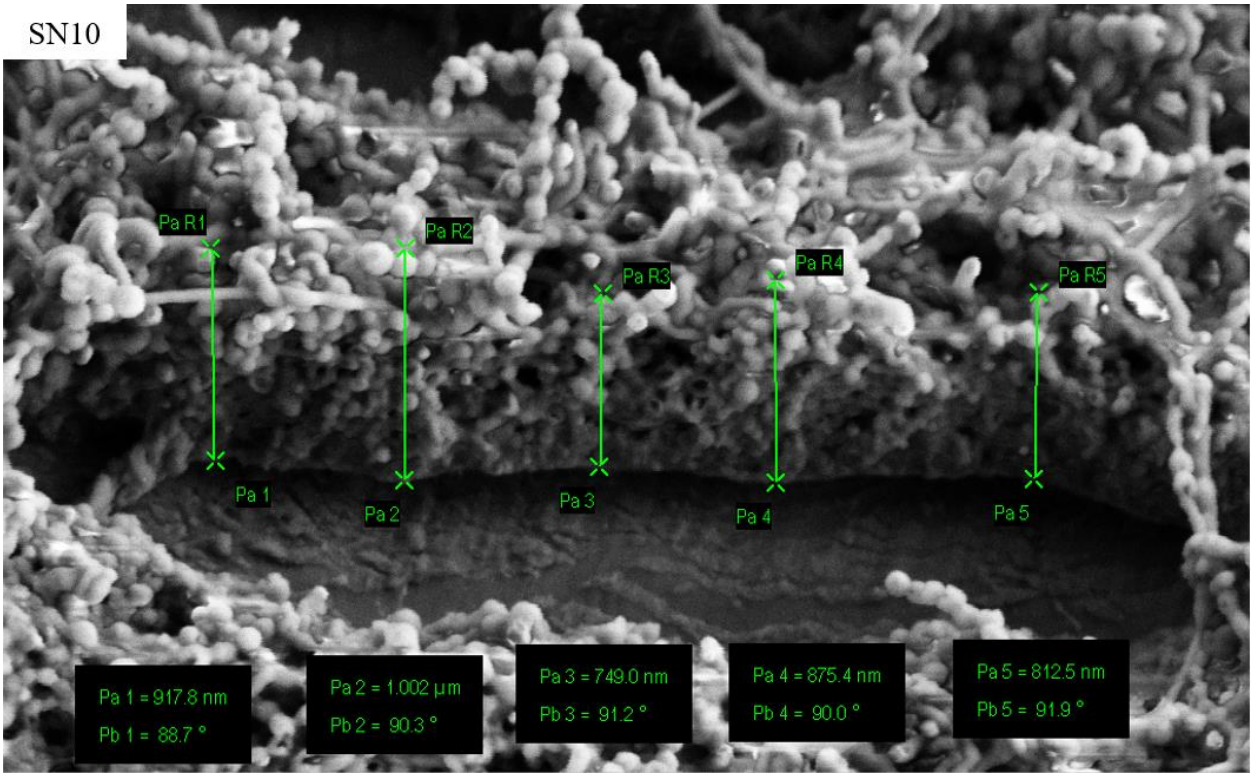

Figure A-12. *An annotated SEM micrograph of the SN10 sample used to measure the thickness of the nanospring mat.*

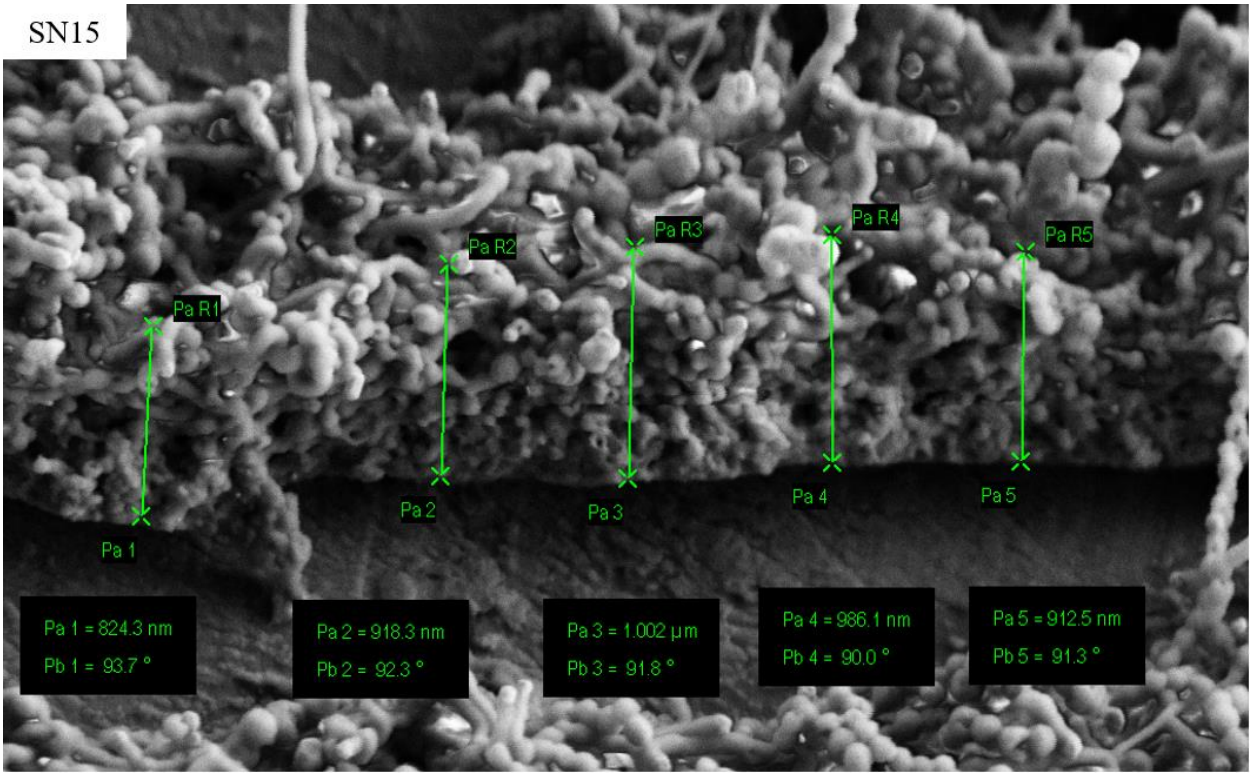

Figure A-13. *An annotated SEM micrograph of the SN15 sample used to measure the thickness of the nanospring mat.*

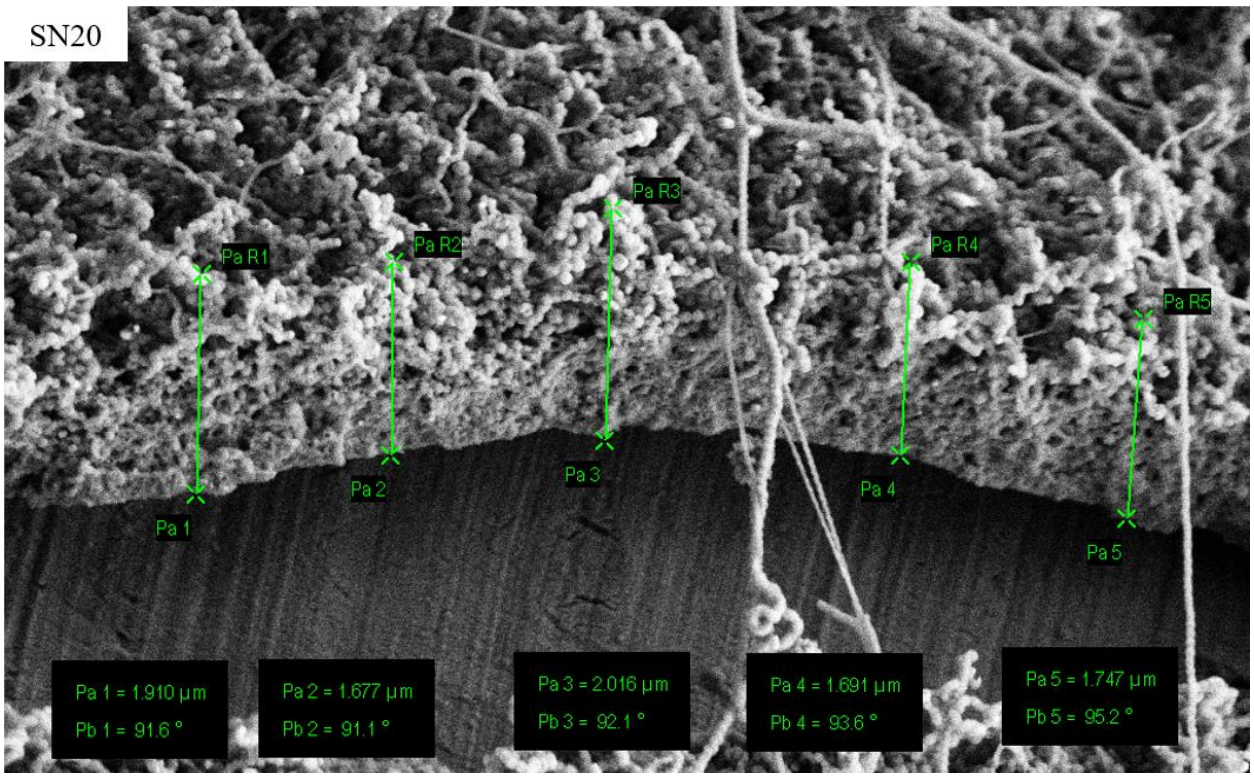

Figure A-14. *An annotated SEM micrograph of the SN20 sample used to measure the thickness of the nanospring mat.*

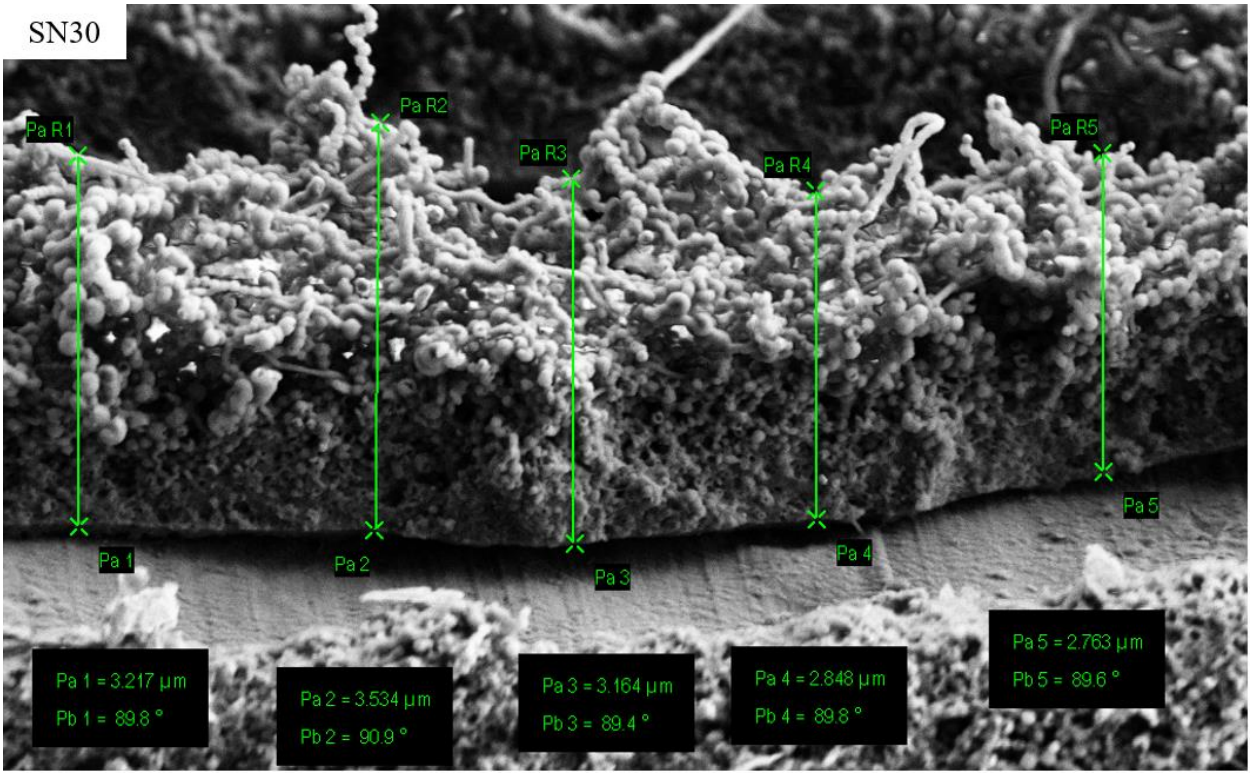

Figure A-15. *An annotated SEM micrograph of the SN30 sample used to measure the thickness of the nanospring mat.*

10.5 Heat Transfer Plots with Error Bars

Plots with error bars shown for only some of the data points were provided in the text in order to better show the trends. For completeness, plots of the heat transferred to the cooling fluid are presented with error bars on all of the data points. As a reminder, a high amount of uncertainty is present at flows with higher Reynolds numbers. This uncertainty is largely due to the small temperature differences occurring between the inlet and outlet of the tube and the associated uncertainty of the thermocouples (0.025°C to 0.044°C with 95% confidence).

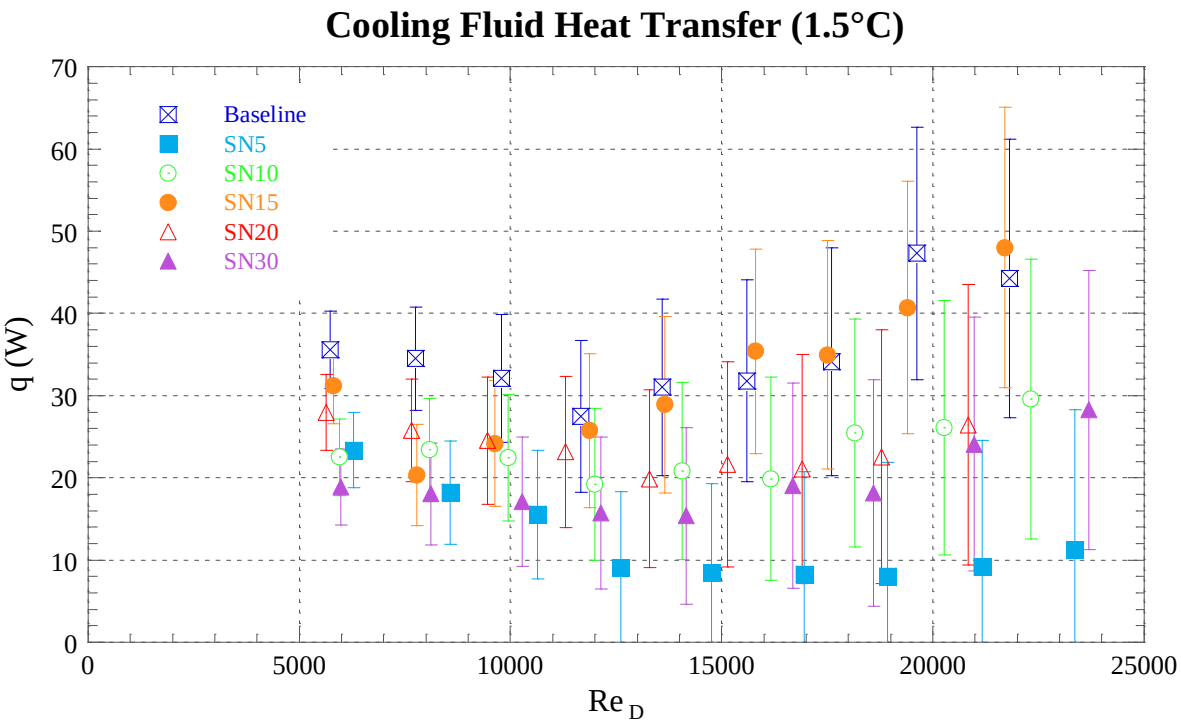

Figure A-16. *Comparison of the heat transferred to the cooling fluid (q) between uniformly coated silica nanospring samples at 1.5°C of subcooling.*

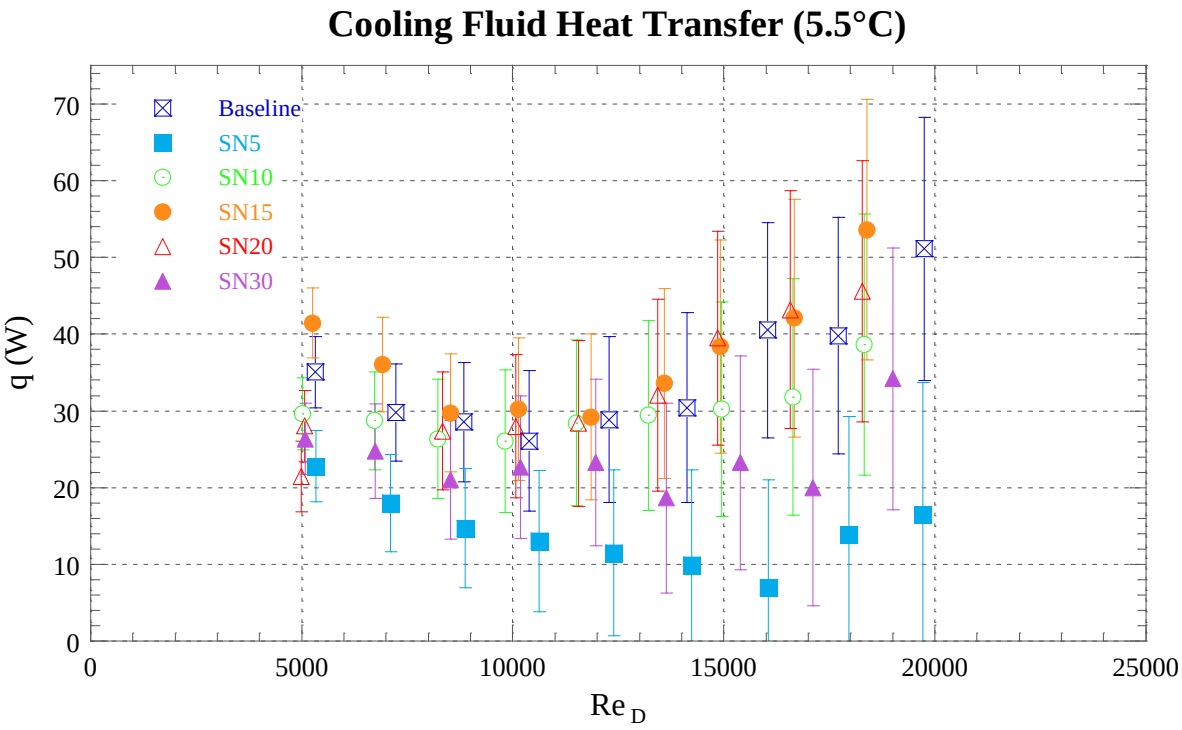

Figure A-17. *Comparison of the heat transferred to the cooling fluid (q) between uniformly coated silica nanospring samples at 5.5℃ of subcooling.*

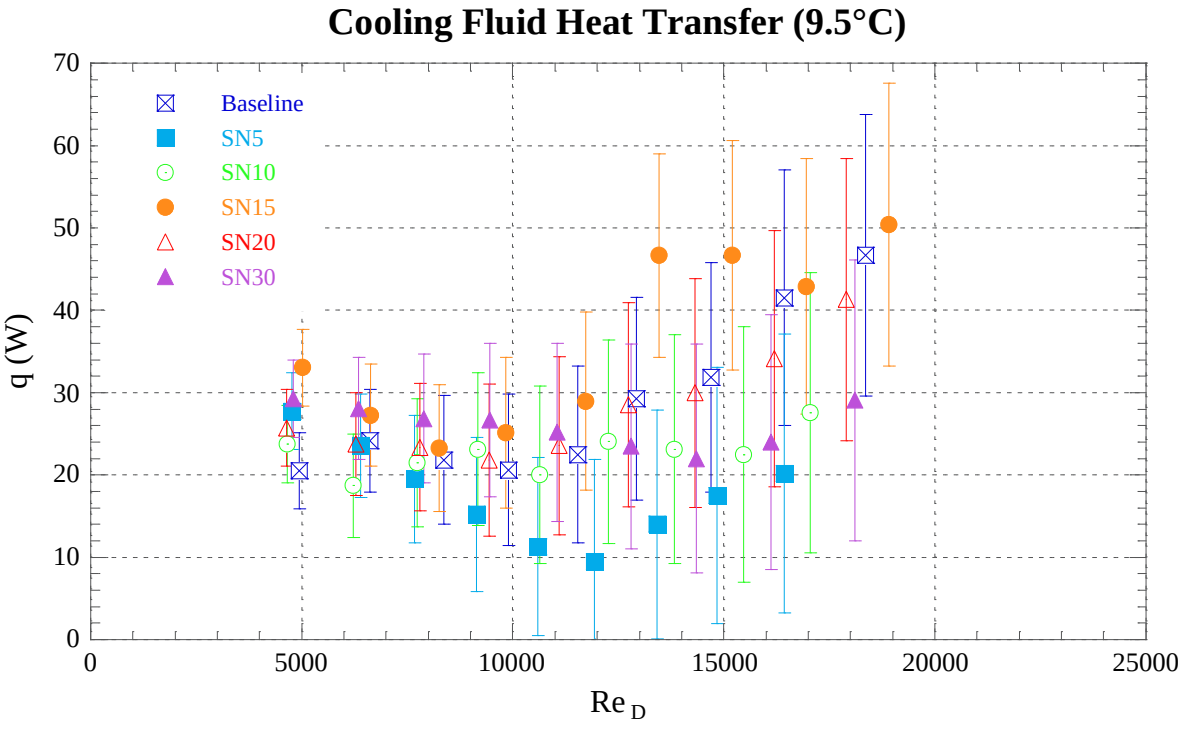

Figure A-18. *Comparison of the heat transferred to the cooling fluid (q) between uniformly coated silica nanospring samples at 9.5℃ of subcooling.*

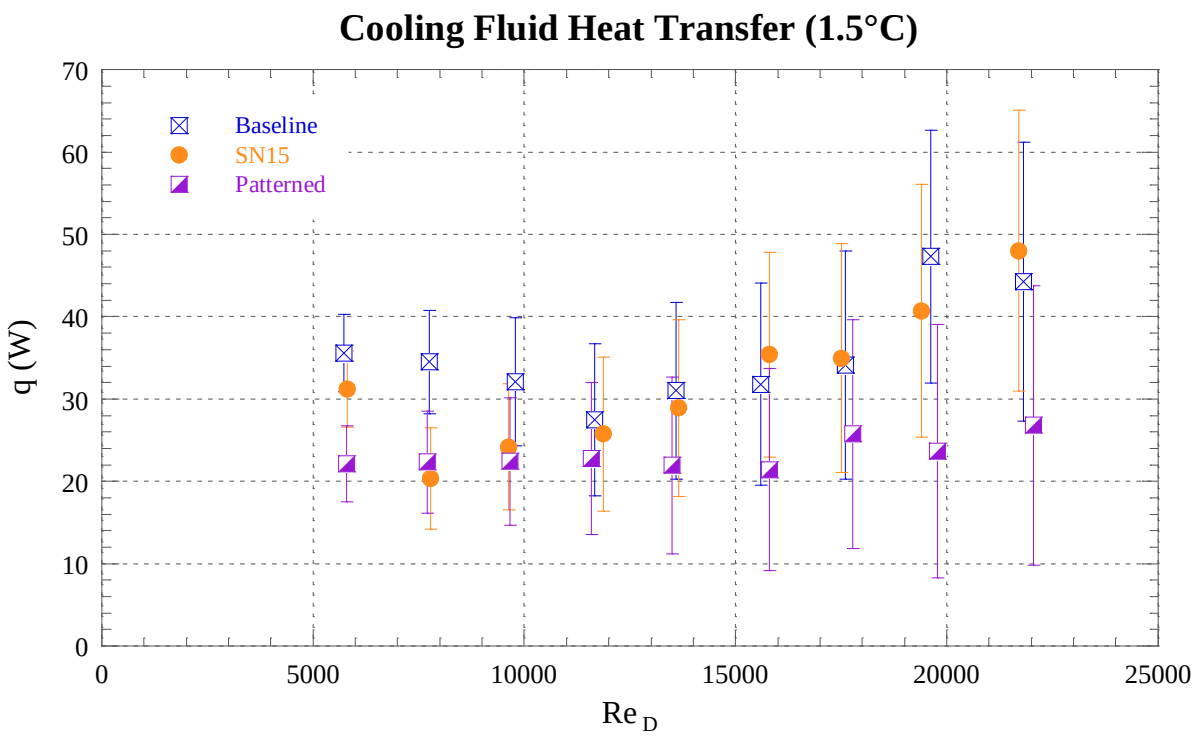

Figure A-19. *Comparison of the heat transferred to the cooling fluid (q) for the patterned surface, the baseline surface, and the SN15 sample at 1.5°C of subcooling.*

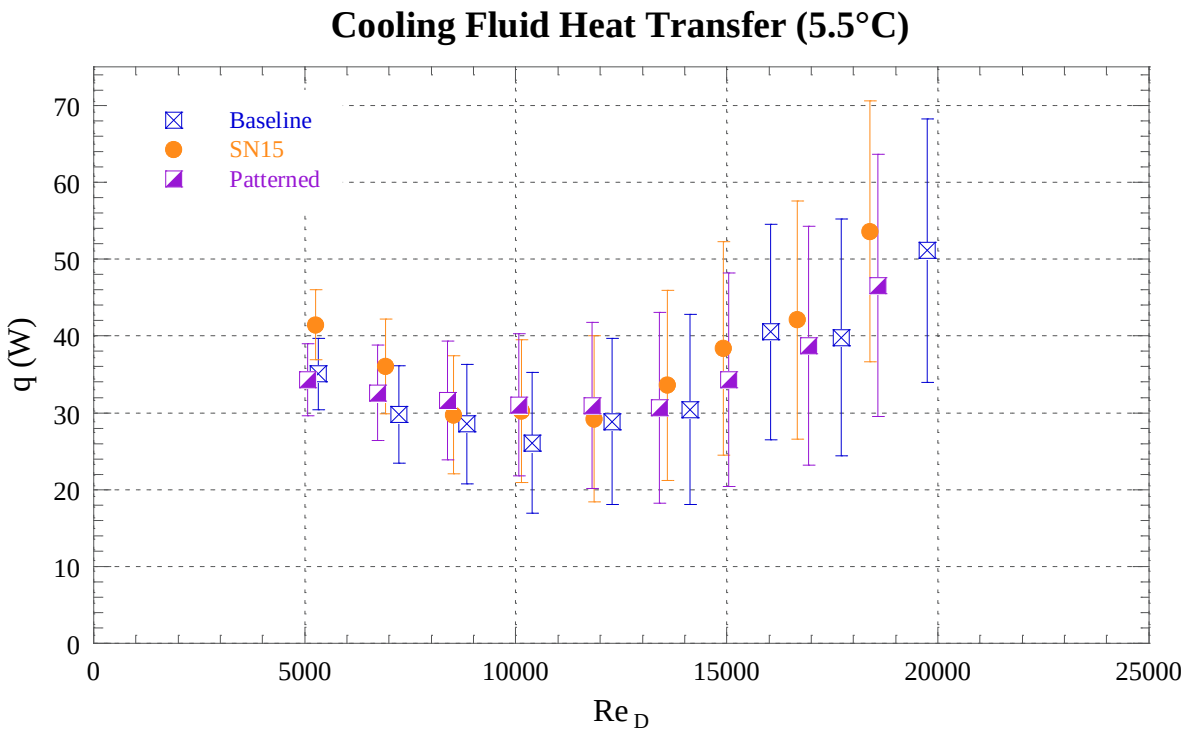

Figure A-20. *Comparison of the heat transferred to the cooling fluid (q) for the patterned surface, the baseline surface, and the SN15 sample at 5.5°C of subcooling.*

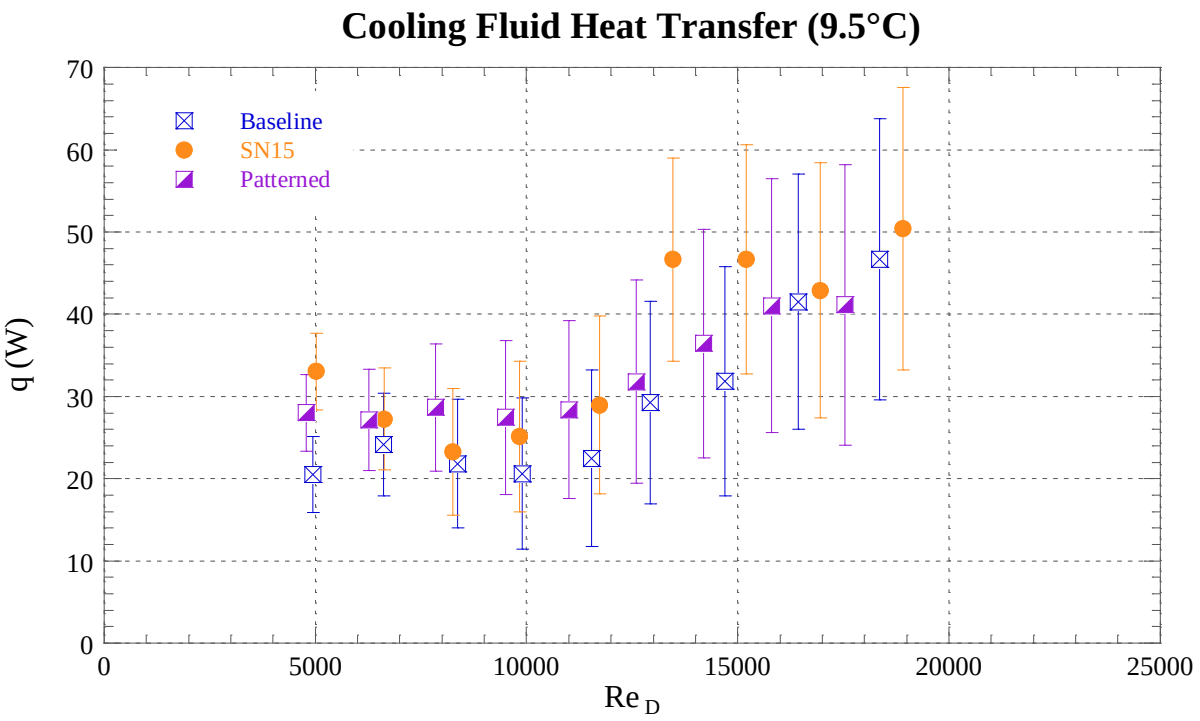

Figure A-21. *Comparison of the heat transferred to the cooling fluid (q) for the patterned surface, the baseline surface, and the SN15 sample at 9.5°C of subcooling.*

10.6 Summary Table of Sample Masses, Thicknesses, and Contact Angle Measurements

Table A-2. *Summary table of sample masses, thicknesses, and contact angle measurements.*

	Baseline	**SN5**	**SN10**	**SN15**	**SN20**	**SN30**	**Patterned**
Growth Time (min)	0	5	10	15	20	30	15
Sputter Time (s)	20	20	20	20	20	20	20
Recipe #	---	5	5	5	5	5	5
d_inner (cm)	0.51	0.51	0.51	0.51	0.51	0.51	0.51
d_outer (cm)	0.64	0.64	0.64	0.64	0.64	0.64	0.64
L (cm)	15.2	15.2	15.2	15.2	15.2	15.2	15.2
Surface Area (cm^2)	30.4	30.4	30.4	30.4	30.4	30.4	30.4
m_i (g)	---	6.75224	6.75313	6.74648	6.69026	6.71058	6.74625
m_Au (g)	---	6.75236	6.75337	6.74663	6.69079	6.71078	6.74625
m_SN (g)	---	6.75337	6.75602	6.74944	6.69429	6.71546	6.74743
Gold Mass (mg)	---	0.12	0.24	0.15	0.53	0.2	0
Nanospring Mass (mg)	---	1.01	2.65	2.81	3.5	4.68	1.18
Nanospring Mass per Area (mg cm^{-2})	---	0.0332	0.0872	0.0924	0.1151	0.1539	0.0388
Thickness (nm)	---	784	948	1081	1825	2902	---
Resistance (K W^{-1})	---	7.09E-05	8.57E-05	9.77E-05	1.65E-04	2.62E-04	---
Resistance of Tube Wall (K W^{-1})	1.19E-03	1.19E-03	1.19E-03	1.19E-03	1.19E-03	1.19E-03	1.19E-03
SN Resistance Percentage of Wall	---	6.0%	7.2%	8.2%	13.9%	22.1%	---
Static CA	83.73	132.98	148.365	151.1	152.66	155.335	---
Advancing CA	98.3	139.96	166.73	160.8	160.44	160.64	---
Receding CA	58.33	117.18	123.52	131.66	140.98	144.43	---
CA Hysteresis	39.97	22.78	43.21	29.14	19.46	16.21	---

10.7 Summary of the Condensate Removal for Each Sample at Each Subcooling

Table A-3. *Summary of the condensate removal for each sample at a nominal subcooling of 1.5°C.*

	Condensate Removal at 1.5°C						
Samples	**Baseline**	**SN5**	**SN10**	**SN15**	**SN20**	**SN30**	**Patterned**
Droplet Count	16	24	44	45	57	33	35
Time (min)	7.52	7.55	7.77	7.52	7.55	7.52	7.52
Droplets/Time (min^{-1})	2.13	3.18	5.67	5.99	7.55	4.39	4.66
Tube Length in Video (cm)	10.86	10.75	10.07	10.16	9.71	10.97	10.58
Normalized Droplet Removal Rate (min^{-1} cm^{-1})	0.20	0.30	0.56	0.59	0.78	0.40	0.44
Average Droplet Diameter (cm)	0.59	0.55	0.46	0.46	0.45	0.45	0.53
Average Droplet Volume (mL)	0.11	0.09	0.05	0.05	0.05	0.05	0.08
Volume Removed (mL)	1.72	2.13	2.27	2.32	2.65	1.53	2.72
Volume Removed per Time (mL min^{-1})	0.23	0.28	0.29	0.31	0.35	0.20	0.36
Normalized Volumetric Removal Rate (mL min^{-1} cm^{-1})	0.021	0.026	0.029	0.030	0.036	0.019	0.034
Percent of Baseline Removal	100%	124%	138%	143%	171%	90%	162%

Table A-4. *Summary of the condensate removal for each sample at a nominal subcooling of 5.5°C.*

Condensate Removal at 5.5°C							
Samples	**Baseline**	**SN5**	**SN10**	**SN15**	**SN20**	**SN30**	**Patterned**
Droplet Count	18	37	47	50	82	46	56
Time (min)	7.52	7.52	7.68	7.52	10.18	7.52	8.37
Droplets/Time (min^{-1})	2.39	4.92	6.12	6.65	8.05	6.12	6.69
Tube Length in Video (cm)	11.08	10.72	11.50	10.35	11.03	10.99	10.60
Normalized Droplet Removal Rate (min^{-1} cm^{-1})	0.22	0.46	0.53	0.64	0.73	0.56	0.63
Average Droplet Diameter (cm)	0.60	0.49	0.48	0.52	0.49	0.42	0.53
Average Droplet Volume (mL)	0.12	0.06	0.06	0.07	0.06	0.04	0.08
Volume Removed (mL)	2.07	2.23	2.64	3.59	5.14	1.82	4.32
Volume Removed per Time (mL min^{-1})	0.28	0.30	0.34	0.48	0.50	0.24	0.52
Normalized Volumetric Removal Rate (mL min^{-1} cm^{-1})	0.025	0.028	0.030	0.046	0.046	0.022	0.049
Percent of Baseline Removal	100%	112%	120%	184%	184%	88%	196%

Table A-5. *Summary of the condensate removal for each sample at a nominal subcooling of 9.5°C.*

	Condensate Removal at 9.5°C						
Samples	**Baseline**	**SN5**	**SN10**	**SN15**	**SN20**	**SN30**	**Patterned**
Droplet Count	17	48	52	60	63	52	40
Time (min)	7.52	7.52	8.00	7.58	7.52	7.52	7.53
Droplets/Time (min^{-1})	2.26	6.39	6.50	7.91	8.38	6.92	5.31
Tube Length in Video (cm)	11.81	10.50	11.48	10.07	11.01	10.64	10.63
Normalized Droplet Removal Rate (min^{-1} cm^{-1})	0.19	0.61	0.57	0.79	0.76	0.65	0.50
Average Droplet Diameter (cm)	0.62	0.49	0.48	0.45	0.43	0.46	0.51
Average Droplet Volume (mL)	0.12	0.06	0.06	0.05	0.04	0.05	0.07
Volume Removed (mL)	2.12	2.97	2.98	2.78	2.62	2.70	2.86
Volume Removed per Time (mL min^{-1})	0.28	0.39	0.37	0.37	0.35	0.36	0.38
Normalized Volumetric Removal Rate (mL min^{-1} cm^{-1})	0.024	0.038	0.032	0.036	0.032	0.034	0.036
Percent of Baseline Removal	100%	158%	133%	150%	133%	142%	150%